The Adsorption Geometry of PTCDA on Ag(111) – an NIXSW Study

Dissertation

zur Erlangung des Doktorgrades (Dr. rer. nat.)
der
Mathematisch-Naturwissenschaftlichen Fakultät
der
Rheinischen Friedrich-Wilhelms-Universität Bonn

vorgelegt von
Annegret Hauschild

Bonn, August 2007

Angefertigt mit Genehmigung
der Mathematisch-Naturwissenschaftlichen Fakultät
der Reheinischen Friedrich-Wilhelms-Universität Bonn

Erster Gutachter	Prof. Dr. M. Sokolowski
Zweiter Gutachter	Prof. Dr. K. Wandelt
Fachnaher Gutachter	Prof. Dr. Th. Bredow
Fachfremder Gutachter	Prof. Dr. F. S. Tautz

Abgabedatum: 31.08.2007

Tag der mündlichen Prüfung: 14.12.2007

Erscheinungsjahr: 2008

Angefertigt am Institut für Physikalische und Theoretische Chemie der
Reheinischen Friedrich-Wilhelms-Universität Bonn

Contents

Chapter 1

Introduction

In this work, the adsorption of a prototype organic semiconducting material on a crystalline silver surface was investigated.

Plastics, or polymers, exist everywhere in our environment. Most packing materials (bags and bottles), many toys (e.g., LEGO), medical applications, clothing and many other things are made out of this material. Cheap oil in the sixties provided the spread of plastics in everyday life. In many fields plastics exhibit better properties than other materials. The main advantage is the cheap and easy production, and that plastics can be tailored to any form. Conventional plastics are electrical insulators, but with the discovery of conductive polymers [Chi 77], many new applications became possible. For their work on conductive polymers, the Nobel price was awarded to A. MacDiarmid, H. Shirakawa and A. Heeger in 2000 [Shi 00].

As plastics, semiconductors are found throughout in everyday life. They form the basis of field effect transistors (FET), used millionfold in processors of personal computers and many other microelectronic devices. The fabrication of semiconductor-based devices has to be performed under extremely clean conditions and requires highly pure materials. By photolithography the so-called integrated circuits (IC) are produced in a relatively simple way and they can be easily reproduced. Most devices are based on silicon and germanium.

The organic semiconductors (OSC) are an alternative to the rigid inorganic material. Both, conducting polymers and small organic molecules belong to this class of materials. They combine the advantages of plastics and conventional semiconductors. Due to the great variety of molecules, almost any size and any property can be designed with the organic materials. Many applications already exist for organic semiconductors. The most prominent example is the organic light emitting diode (OLED). Today, OLEDs cover the complete spectrum of colors. They are found in displays of mobile phones, MP3-players and many other devices. OLEDs do not need any background illumination, they are extremely flat and they provide brilliant images with a high contrast. Additional advantages are low fabrication costs and low power consumption.

Organic solar cells and organic field effect transistors (OFETs) are other promising applications of organic semiconductors. However, they do not reach the performance of conventional semiconductors, yet. The charge-carrier mobility, for instance, which is important for the switching frequency, is still much lower for organic semiconductors ($10^{-1} - 20\,\mathrm{cm}^2/\,\mathrm{V\,s}$) than for the conventional ones ($1 - 10^4\,\mathrm{cm}^2/\,\mathrm{V\,s}$). However, the combination of OLEDs and OFETs opens the possibility of flexible displays, e.g., the electronic newspaper or a rollable display for mobile phones. Regarding the prototypes for these devices, a rapid further development can be expected. Moreover, due to the enduring fall in prices for semiconductor devices, new concepts are required in semiconducting industry. Therefore, OFETs represent an interesting field of further research.

In recent years, a broad research activity was focused on interfaces of organic semiconductors and inorganic materials. This is due to the fact that, e.g., in the OFET technology, the insulator-semiconductor interface plays a crucial role for the performance of the device [Kla 06]. Also, the metal-semiconductor interface is of technological importance, e.g. for OFETs and organic solar cells [BarRav 03].

Since the first few layers of the organic material significantly determine the properties of the whole device, it is a major challenge to understand the electronic and geometrical structure of organic semiconductors adsorbed on a particular surface. However, a reliable model for predicting the properties of a given molecular material is still not available. Calculations of the interface based on density functional theory (DFT) often only give imprecise or wrong results, and do not reflect the real situation of the interface at all. By the experimentally determination of as many parameters as possible for different interfaces, it will be possible to test and to improve the theoretical calculations. Hence, the results of the calculations will become much more reliable in the future.

The aim of the present work was to further solve the puzzle of the geometrical properties of organic semiconductors on metal crystal surfaces. Therefore, normal incidence x-ray standing waves (NIXSW) studies were performed on 3,4,9,10-perylenetetracarboxylic dianhydride (PTCDA), which represents an extensively studied model system of the organic semiconductors.

Monolayer films of PTCDA were grown on a silver(111) surface at different temperatures. Depending on the temperature, different lateral structures were obtained. An introduction to this organic material and particularly to the system of PTCDA adsorbed on Ag(111) will be given in chapter 2.

By the NIXSW technique, the vertical distances of an adsorbate to the underlying substrate can be determined which is an important parameter for any kind of calculations. The NIXSW method is based on a Bragg reflection of the underlying substrate. For varying energies of the incident x-ray beam close to the Bragg energy, the photoemission (PE) yield (and also the electron yield from Auger electron spectroscopy (AES) and the fluorescence yield) of the adsorbate exhibits a particular profile, depending on the adsorbate's position on the substrate. A detailed description of this experimental method is given in chapter 3.

At room temperature, PTCDA forms a long range ordered monolayer film on the Ag(111) surface [Glö 98]. If the atoms of one element are chemically different and on distinct vertical positions, it is possible to measure these position, as it will be demonstrated. The results of the room temperature phase, obtained in this work, are presented in chapter 4.

At low temperatures a metastable phase exists [Ere 03] [Tem 06b] [Kil 07] which exhibits no long range order. The results for this so-called precursor phase [Bar 00] are given in chapter 5.

Finally, in chapter 6, the results of the two distinct phases are compared. The results are summarized in chapter 7.

Chapter 2

PTCDA

The substance 3,4,9,10-perylenetetracarboxylic dianhydride ($C_{24}O_6H_8$), or PTCDA, is an organic semiconductor. A ball-and-stick model of this planar molecule is shown in the inset of figure 2.1. Due to its color and its thermal stability, this molecule is used as a red pigment, e.g., in automotive applications. PTCDA often is referred to as the prototype of organic semiconductors, since it has an unique electronic structure and it grows on surfaces in a well defined way [Bul 96] [For 97]. The fact that PTCDA is an extensively studied molecule can be seen by the numbers of publications on PTCDA in recent years (figure 2.1).

PTCDA is a large molecule with an extended conjugated π-electron system. Its molecular weight is 392 u. The molecule consists of a perylene body with two functional groups (dicarboxylic anhydride groups) at both sides. Due to these partially negatively charged anhydride groups, the molecule has a quadrupole moment. The bulk crystal structure is characterized by flat lying molecules in the (102) planes, which form a stacking structure. Two different morphological forms are known, the α- and β-modification [MoeKar 92]. The α-phase is the more compressed and more stable phase [Kil 04]. The space group for both phases is P2_1/c. There are two molecules per unit cell. The lattice parameters for the α-phase are $a = 3.72\,\text{Å}$, $b = 11.96\,\text{Å}$, $c = 17.34\,\text{Å}$, $\beta_c = 98.8°$ with a volume of $766.5\,\text{Å}^3$ [Lov 84] and for the β-phase $a = 3.78\,\text{Å}$, $b = 19.30\,\text{Å}$, $c = 10.77\,\text{Å}$, $\beta_c = 98.8°$ with a volume of $780.8\,\text{Å}^3$ [MoeKar 92].

In the (102) plane of the bulk, the molecules are arranged in the so-called *herringbone structure.* The short axis of one molecule faces the long axis of another molecule. This plane is of particular importance. On the one hand side, it is the cleavage plane of the crystal [AloGar 04]. On the other hand side, on many substrates, PTCDA arranges in this particular way, when grown by molecular beam epitaxy. The occurrence of the herringbone structure indicates that the interactions of the molecules within this plane play a major role. This structure of PTCDA is found for monolayers on various surfaces, as e.g. on HOPG [Hos 94], on MoS_2 [Lud 94], on Au(111) [SH 97], on Au(100) [SH 99], on Ag(111) [Glö 98], and on Cu(111) [Wag 07].

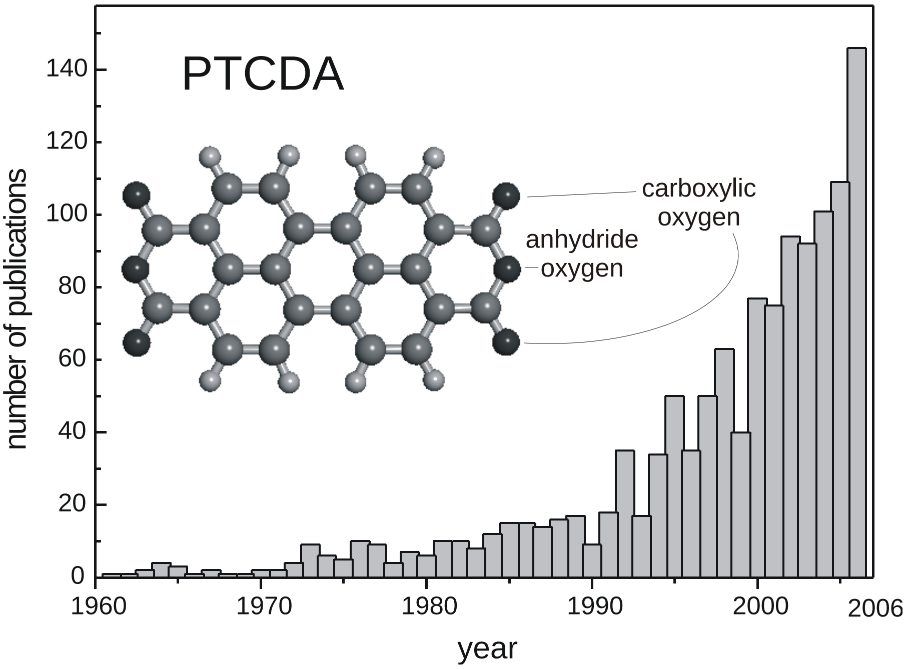

Figure 2.1: *Increasing number of publications related to PTCDA from 1960 to 2006, as obtained from the search engine scifinder scholar. Inset: Ball-and-stick model of the planar molecule PTCDA. The carbon atoms are shown in dark grey, the oxygen atoms in black color and the hydrogen atoms in white color. The latter are located at the end of the short axis. The carboxylic oxygen atoms correspond to the four outer O atoms. The anhydride oxygen atoms correspond to the two inner O atoms.*

The adsorption of PTCDA on various surfaces has been so far investigated in great detail. In the following, details will only be presented for the specific features of the PTCDA (sub-) monolayer on Ag(111) at different temperatures, as this is of importance for this work. For a more general introduction to the epitaxial growth of PTCDA on various metal surfaces see e.g. the review article of Barlow and Raval [BarRav 03] or the review article of Witte and Wöll [WitWöl 04].

2.1 The room temperature phase of PTCDA on Ag(111)

At room temperature, PTCDA forms a commensurate monolayer on Ag(111). Due to the symmetry of Ag(111), the adsorbate grows in six symmetry equivalent domains. These domains exhibit an almost defect-free long-range order [Umb 96].

The unit cell of the adsorbate consists of two molecules arranged in the herringbone structure. The unit cell parameters agree within 2% with those of the β-phase of the (102) net plane [Glö 98] [Umb 98]. It was found by NEXAFS that in this structure, the molecules lie flat on the surface [Tab 95].

Kraft et al. revealed the lateral adsorption geometry by means of STM and DFT calculations [Kra 06]. They found two distinct lateral positions for the two molecules in the unit cell. However, for both molecules the central carbon ring is positioned on a bridge site.

The monolayer exhibits a thermal stability up to approximately 560 K, it cannot be thermally desorbed from the Ag surface. However, it is found to dissociate at temperatures above 560 K [Glö 98] [Sei 93]. The multilayer desorption takes place at about 510 K, the desorption of the second layer occurs at about 510 K to 530 K. Therefore, the monolayer can be easily prepared by desorbing the multilayers at temperatures of 550 K [Kil 04].

The desorption behavior as well as the ultraviolet photoelectron spectroscopy (UPS) and the high resolution electron energy loss spectroscopy (HREELS) data reveal a strong chemisorptive bonding of the first layer of PTCDA on Ag(111) [Kil 02a] [Zou 06] [Shk 00]. Strong changes in the electronic structure of the molecule were found for the monolayer. Compared to the multilayer, the

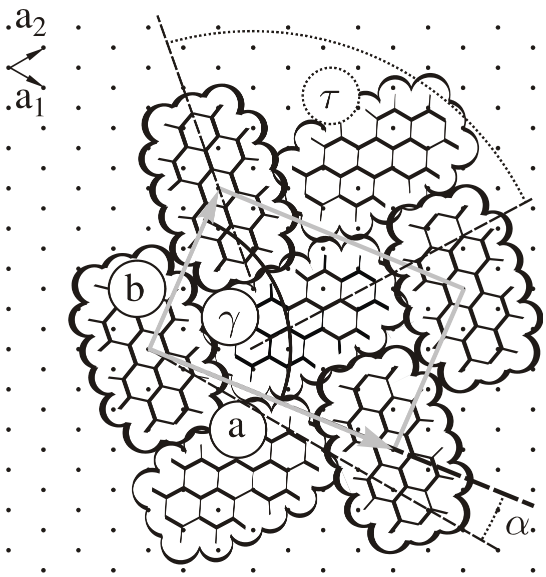

Figure 2.2: *Herringbone pattern of the monolayer PTCDA on Ag(111) found by STM and high resolution LEED. This figure was taken from [Glö 98].*

HOMO-LUMO transition is shifted to lower energies in the monolayer [Jun 93] [Tab 95] [Shk 00]. This can be attributed to a strong molecule-substrate interaction. Eremtchenko et al. found hints that the bonding involves mainly the carbon atoms and that it is restricted to the central carbon ring [Ere 03] [Ere 04].

The lowest unoccupied molecular orbital (LUMO) of the molecule in the multilayer is shifted in the monolayer to lower energies and is cut by the Fermi level. Hence, it is the new highest occupied molecular orbital (HOMO) which is partially filled. This indicates that the monolayer of PTCDA on Ag(111) is metallic [Zou 06]. Evidence for this metallic state was also found by means of scanning tunnelling microscopy (STM) and HREELS. This metallicity leads to strong interfacial dynamic charge transfer [Tau 02b]. The partial occupancy of this orbital (the former LUMO) can be concluded from STM measurements, because this orbital can be imaged under positive and negative bias condition [Tau 02a].

2.1.1 Adsorption of PTCDA at step edges

In the present work, the geometrical structure of the molecule PTCDA on Ag(111) was investigated. By using normal incidence x-ray standing waves (NIXSW), the geometrical properties of a large area on the sample are averaged. If other geometrical arrangements are present besides the described herringbone structure, this has to be taken into account, because it directly influences the results. Specific geometric arrangements of PTCDA were found on the step edges of the Ag(111) substrate which turn out to be relevant for the present work. Thus, these are described in the following.

Glöckler et al. found that the steps of the silver (111) crystal are decorated with PTCDA molecules. On single atomic steps no molecules were found, only on double steps of 4.72 Å height (and higher steps) the molecules were observed [Glö 98]. The molecules stand upright at the steps, hereby the molecule orientation alternates from one molecule with the long axis perpendicular to the step to the next one with its long axis parallel to the step. After annealing the sample, further step bunching is observed. The authors ascribe this preference of step edges to a stronger bonding mechanism which occurs on the Ag(110)-like step sites.

Marchetto et al. investigated the growth behavior of PTCDA on Ag(111) with UV photoelectron emission microscopy (UV-PEEM) [Mar 06]. In the submonolayer range, they found a preferred growth of the molecules at the step edges. They discuss models of either an attractive or a repelling (Ehrlich-Schwoebel barrier [EhrHud 66] [SchShi 66]) potential for the diffusing PTCDA molecules at the step edges. The authors point out the difficulty of the interpretation of integrating measurements which average the signal over large surface areas. The authors claim that the surface morphology plays an important role. Since the employed technique of this work, namely NIXSW, is an integrating measurement, this is an important aspect for the interpretation of the results of this work.

In his Ph.D. thesis, C. Seidel investigated PTCDA on Ag(775) [Sei 93]. This surface is similar to a Ag(111) surface which is highly stepped. He found that PTCDA is adsorbed in chains on biatomic steps. On triatomic steps he observed two lines of PTCDA molecules, very similar to the herringbone structure. In the submonolayer range up to 0.5 monolayers, no coverage of the (111) terraces could be found. S. Schmitt described in his Ph.D. thesis that the annealing of such a structure yields an adsorbate-induced reconstruction of the steps, as shown in figure 2.3.

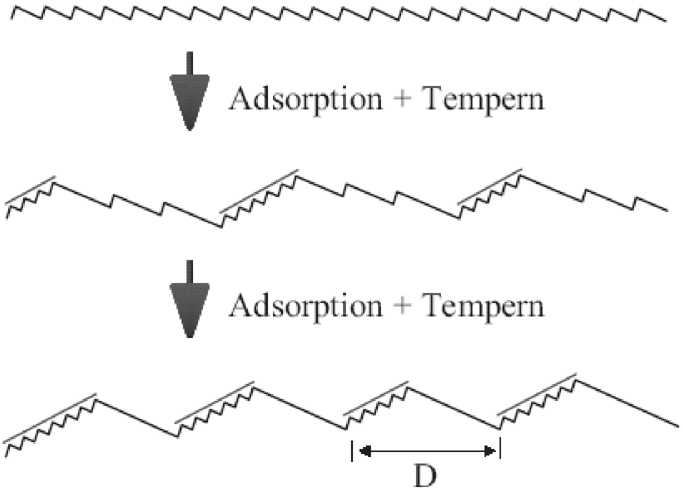

Figure 2.3: *Adsorbate induced reconstruction of a vicinal Ag(111) surface. The reconstruction occurs after deposition of PTCDA and subsequent annealing. This figure was taken from reference [Sch 06]. This is of importance of the present work, since the used Ag(111) crystal can be slightly stepped. For the preparation of a monolayer, the organic material was evaporated on the crystal and then subsequently annealed. Therefore, depending on the crystal quality, such a adsorbate induced reconstruction can occur also for the thin films prepared in this work.*

2.2 The low temperature phase of PTCDA on Ag(111)

In 2001, Kilian discovered the metastable low-temperature phase of PTCDA on Ag(111) [Kil 02a] which he identified as a *precursor* state. He found this phase of the molecules at coverages below the monolayer coverage of the room temperature phase.

For the preparation of this phase, the PTCDA is deposited at temperatures clearly below 160 K onto the Ag(111) substrate. The precursor state only exists below 160 K. No long range order was found neither by high resolution low energy electron diffraction (LEED) nor by STM [Kil 02a] [Tem 06b]. Heating the sample with the precursor phase, the PTCDA molecules turn into the commensurable ordered monolayer phase at temperatures of about 170 K.

From UPS, Kilian deduced that the molecules are chemisorbed. In contrast to the room temperature state, the precursor phase appears semiconducting [Kil 02a]. Striking is also the difference in the HREELS spectra in comparison to the spectra of the room temperature phase, where (in the RT-phase) enhanced inplane Raman modes were observed. These are due to charge transfer of the central carbon rings to the substrate. This charge transfer only is possible, because the partly filled former LUMO strongly interacts with the substrate. For the precursor phase, these modes were not observed [Ere 03] [Ere 04].

In this thesis the room-temperature phase will be named *monolayer* and the metastable low-temperature phase will be named *precursor*.

Chapter 3

Introduction to NIXSW

In this chapter, the NIXSW method will be introduced. The theoretical background of the experiment is given by the dynamical x-ray diffraction (see section 3.1). The Auger process for XSW is shortly described in section 3.2, and the PE process with the multipole contributions, and the systematic resulting uncertainties of the results are described in section 3.3. The experimental setup of the beamline ID32 at the *ESRF* in Grenoble, at which these experiments were performed, is described in section 3.4. In section 3.5, an introduction is given to the computer programs used for the data analysis, as well as to the Argand diagrams commonly used to visualize NIXSW results.

3.1 Dynamical x-ray diffraction theory

The NIXSW technique is based on Bragg scattering. However, for the description of x-ray standing waves, the kinematical diffraction theory is failing. In the kinematical theory, the scattering from each volume element in the sample is treated as being independent. In contrast, the dynamical theory considers all wave interactions within the crystalline particle. While diffraction takes place, the entire wave field inside a crystal is treated as a single entity. Generally, this theory has to be applied, whenever diffraction from large perfect crystals is being studied.

The crucial change between kinematical and dynamical scattering theory can be understood in the concept of the Ewald sphere. In reciprocal space, there no longer is a single Ewald sphere for a single monochromatic incident ray. Instead, one has to determine the loci of permitted Ewald spheres, the so-called dispersion surface. Wave vectors drawn from points on this surface to reciprocal lattice points represent waves that are permitted solutions of Maxwell´s equations in a periodic medium. The geometrical construction of the dispersion surfaces is shown in figure 3.1. For further reading, an excellent description of the dynamical theory is given in the review article from Batterman and Cole [BatCol 64].

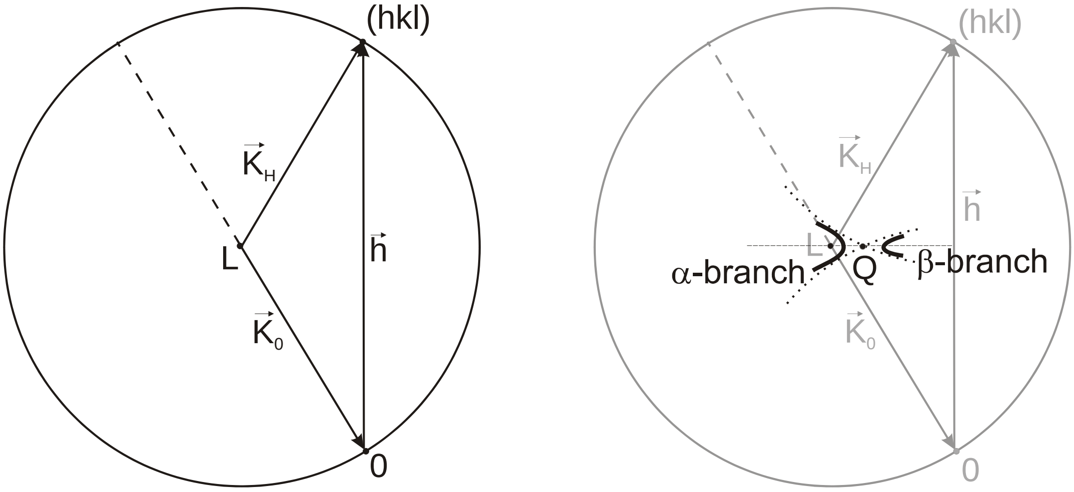

Figure 3.1: *Left: Ewald sphere in reciprocal space; the Bragg reflection is described with the kinematical diffraction theory. L is the so-called Laue point, the center of the Ewald sphere.* $\vec{h}$ *is the reciprocal lattice vector of the (hkl) diffraction. Right: geometrical construction of the dispersion surface, obtained in the dynamical theory. Instead of the Laue point, the center of the Ewald sphere (the kinematical construction is still shown in grey) corresponds to Q. The distance between L and Q is proportional to the average index of refraction. The spheres (shown with the black dotted lines in the right figure) through Q, which are centered on 0 and (hkl), form asymptotes for the hyperbolas of the so-called "dispersion surface". The dispersion surface corresponds to the* α*- and* β*-branch represented by the thick black lines. By changing the angle (or respectively the energy) of the incident x-ray beam with respect to the crystal, the different tie points on the dispersion surfaces are "excited", and the reflection curve is obtained (Darwin Prins curve - e.g., see top left in figure 3.2 for silver(111)). For a better visualization, the distance from L to Q is strongly exaggerated in this figure, with respect to the radii of the spheres.*

3.1.1 The standing wave field

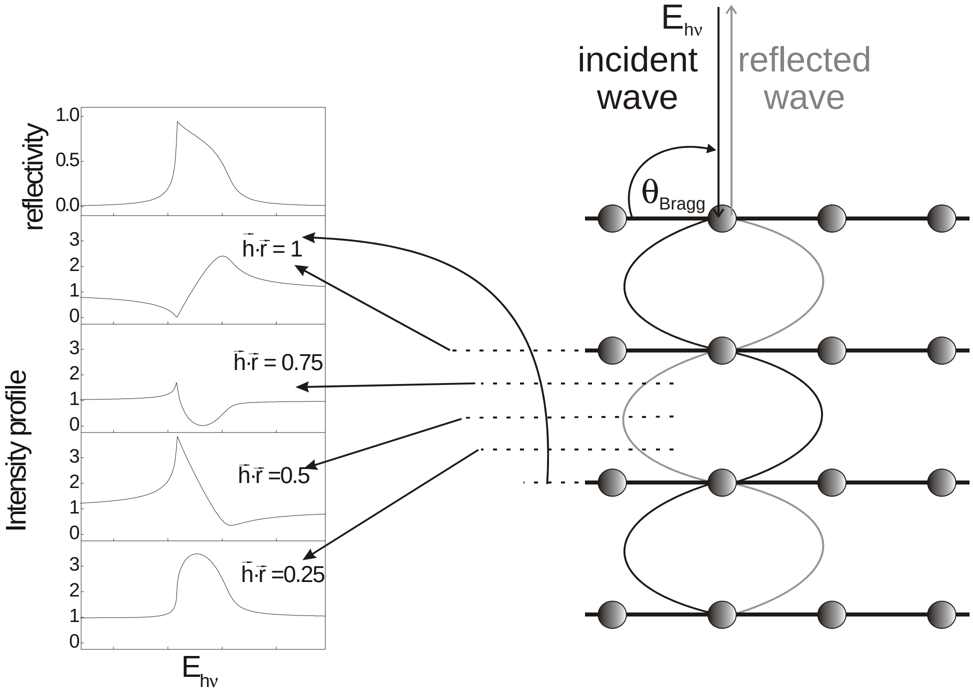

Figure 3.2: *By rocking the crystal angle or changing the photon energy* $E_{h\nu}$*, a reflection curve is obtained. Top Left: Ideal reflection curve for Ag(111). Below: Depending on the vertical position inside the crystal (with respect to the diffraction planes), the photon intensity profile* $I(\nu)$ *(or* $I(\theta)$*) of the coupled wavefield changes with crystal angle or photon energy close to the Bragg condition (the data for this figure were calculated with the program DARE [Zeg 02]). The corresponding vertical positions within the crystal are shown on the right and the normally incident x-rays.*

Close to the crystal x-ray Bragg condition, an x-ray standing wave interference field with sinusoidal electric field intensity is created [BatCol 64]. The total electric field is given by the superposition of the incident E_0 and the reflected E_h monochromatic plane waves which are coherently coupled. The wave-field intensity $I(\vec{r})$ at an arbitrary point $\vec{r}$ in space is given by the square of the electric field. For σ polarization this can be expressed as [Zeg 93]:

$$I(\vec{r}) = |E_0|^2 \left[1 + R(E) + 2\sqrt{R(E)}\cos(\nu(E) - 2\pi\vec{h}\cdot\vec{r})\right]. \qquad (3.1)$$

Herein $\vec{h}$ is the reciprocal-lattice vector of the crystal, ν is the phase of the complex-field amplitude ratio $E_h/E_0 = \sqrt{R}e^{i\nu}$, and $R = |E_h/E_0|^2$ is the reflectivity function (Darwin-Prins curve [BatCol 64]). Both $R(E)$ and $\nu(E)$ are functions of the photon energy or of the angle close to the Bragg condition. ν changes in its value by π across the width of Bragg reflection. The periodicity of the standing-wave field intensity is $d = 2\pi/h$, which is equal to the diffraction-plane spacing of the crystal. Equation (3.1) shows the dependence of the wave-field intensity on the vector $\vec{r}$. The scalar product $\vec{h} \cdot \vec{r}$ can be simplified by

$$\vec{h} \cdot \vec{r} = h \cdot z, \tag{3.2}$$

where z is defined to be the component of $\vec{r}$ parallel to $\vec{h}$.

This transformation highlights a very important point. The wave-field intensity $I(\vec{r})$ directly depends on the vertical position z, with respect to the diffraction planes. By varying the photon energy (or the crystal angle θ, i.e., "rocking" the crystal), each individual vertical position z yields a particular wave-field intensity profile $I(\vec{r},E)$. Hence, each intensity profile can be led back to a particular vertical position within the crystal. In figure 3.2, profiles are shown for different vertical positions with respect to the diffraction planes.

The standing wave field also exists above the surface of the crystal. This is an important fact for the application of the standing wave technique to adsorbates on surfaces. Any adsorbate on the top of the crystal experiences a particular x-ray intensity variation, by rocking the Bragg angle or changing the energy in the vicinity of the Bragg peak. This variation depends on the vertical distance of the adsorbate to the substrate surface.

Considering single site and multiple site adsorption

The essence of the x-ray standing waves (XSW) technique is that the adsorbate on the surface experiences a specific x-ray intensity profile that is related to its vertical distance above the surface. This profile can be measured by determining the photoemission (PE)-yield, the Auger-yield or the fluorescence-yield variation of the adsorbate atoms in a standing x-ray wave experiment.

However, in the so-called *multiple site adsorption,* an adsorbate occupies several different vertical positions on the surface, hence equation (3.1) must be modified.

For a number N of atoms of a particular element the yield is the sum of the yields from the individual atoms i at their positions $\vec{r_i}$.

$$I \propto 1 + R\,(\nu) + \frac{2}{N}\sqrt{R\,(\nu)}\sum_{i=1}^{N}\cos(\nu - 2\pi\vec{h}\cdot\vec{r_i}), \tag{3.3}$$

herein the reflectivity R is written as a function of ν which is equivalent to $R\,(E)$. The scalar product $\vec{h}\cdot\vec{r_i} = C_{Pi}$ corresponds to the so-called coherent positions. It describes the vertical adsorbate position relative to the diffraction plane normalized to the diffraction plane spacings d_s.

In the so-called *single site adsorption* all adsorbate atoms occupy the same vertical position. Therefore the sum in equation (3.3) can be transformed to a cosine function with only one particular coherent position C_P, instead.

In order to obtain a general description of the intensity profile, equation (3.3) has to be further transformed. The distribution of the atoms can be described as

$$G(\vec{r_0}) = \frac{1}{N}\sum_{i=1}^{N}\delta(\vec{r_i} - \vec{r_0}).$$

Therefore the normalized result for the intensity can be written as

$$I \propto 1 + R\,(\nu) + 2\sqrt{R\,(\nu)}\int_V G(\vec{r})\cos(\nu - 2\pi\vec{h}\cdot\overrightarrow{r})d\vec{r}. \tag{3.4}$$

The above equation can be transformed to

$$I \propto 1 + R\,(\nu) + 2\sqrt{R\,(\nu)}C_F\cos(\nu - 2\pi C_P). \tag{3.5}$$

This can be understood since the sum of cosine functions of the common variable ν yield again a cosine function of ν. In this equation, the so-called coherent fraction C_F corresponds to the resulting amplitude of the cosine [Zeg 93]. For single site adsorption, C_F is equal to 1. For multiple site adsorption, C_F takes in values below 1, and, depending on the particular adsorption sites, it can even vanish.

The value C_P often is explained as being the average vertical position of the atoms. However, the resulting C_P represents the phase shift of the integral cosine function in the standing wave equation. Only in some particular cases, C_P corresponds also to the average vertical position. This is the case for two distinct adsorption sites with equal C_F. For more than two adsorption sites, this is approximately true when the adsorption sites do not differ much in their coherent positions. For further discussion on this topic see section 3.5.1.

It has to be pointed out that equation (3.5) is the key formula for the NIXSW experiments, all following results are based on this equation. The coherent parameters C_P and C_F can be fitted to the experimental data, because the PE- and the Auger-yield in a standing wave field follow equation (3.5).

3.2 Auger emission for XSW

The Auger signal can be used for the determination of the structural parameters C_P and C_F in a NIXSW experiment.

By the x-rays a core hole is created which is filled with an electron from an outer shell. The energy gain of this electron is transferred to another electron which emits with a defined kinetic energy. The detection of these electrons corresponds to the so called Auger electron spectroscopy (AES) [HenGöp 94].

The determination of the structural parameters of an adsorbate with the Auger signal is difficult since the core hole can be excited by the incident x-rays and by electrons. Therefore, the adsorbate Auger signal consists of two contributions, one originating from the photon-excitation which carries the structural information from the adsorbate, the other originating from the excitation by escape-electrons from the bulk which are caused by inelastically scattered photoelectrons from the substrate. For the results of a NIXSW experiment obtained from the Auger signal, this means that the resulting structural parameters also correspond to the average of this two contributions (see chapter 4.5.1) [ShaCow 98] [Sta 04].

3.3 Multipole effects in photoelectron emission

Unfortunately, equation (3.5) does not strictly describe the PE yield. This is due to the so-called multipole effects.

The PE yield has an angular distribution, depending on the direction of the photons (see figure 3.3) and the initial state. Therefore, for particular experimental geometries (as used in this work), there is a difference in the photoelectron yield excited by the incident beam and the photoelectron yield excited by the reflected beam. In a standing wave experiment, the total photoelectron yield is recorded for various excitation energies close to the Bragg condition. Due to this described asymmetry in the photoelectron yield for the incoming and outgoing x-ray waves, there is a non negligible difference in the photoelectron-intensity profile and the wave-field intensity profile $I(\vec{r})$ which has to be taken into account for the PE-cross section.

Therefore, the multipole contributions have to be included in the evaluation of the XSW data, in order to obtain correct results. This effect was first taken into account in an XSW evaluation by Fisher et al. in 1998 [Fis 98]. The knowledge of the correct *multipole parameters* is essential for the identification of the true vertical position. In literature, several ways, as well experimental as theoretical ones, are described for the determination of the multipole parameters. The citations for the multipole parameters needed in this work are presented in section 3.3.3. The discussion about the correct multipole contributions is still in progress (see section 3.3.3), also several different notations are in use. The multipole formalism, presented here, follows the paper of Nelson et al. [Nel 02].

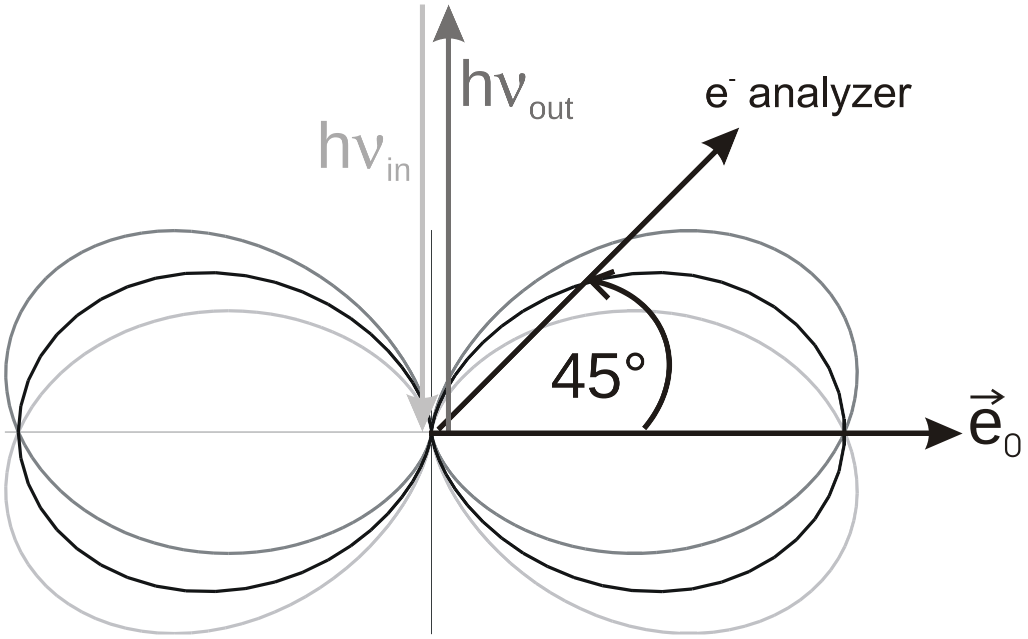

Figure 3.3: *Angular photoemission distribution for the 1s core level transition. Black: dipole approximation; light grey: electrical quadrupole approximation for the electrons excited by the incoming x-rays; dark grey: electrical quadrupole approximation for the electrons excited by the outgoing x-rays. The electron analyzer is positioned at 45 degrees with respect to the beam in the experimental setup of this work. The formalism is found in equation 3.12. The vector* $\vec{e}_0$ *corresponds to the polarization which is the same for the incoming and outgoing x-rays in this work.*

3.3.1 Photoelectric process and XSW

In the photoemission (PE), a photon is absorbed by an atom. Due to the gained energy, an electron of the atom is excited from the ground state $|i\rangle$ to an excited final state $|f\rangle$. For the PE process, one has to calculate the photoelectron emission matrix element under excitation by the x-ray standing wave interference field. Therefore, the individual photoelectron emission matrix elements from the incident *and* reflected waves are needed. The differential photoelectron yield $dY/d\Omega$ in space is proportional to the squared matrix element between the initial and the final states:

$$\frac{dY}{d\Omega} \propto |M_{fi}|^2 , \tag{3.6}$$

where

$$M_{fi} = E_0 e^{i\vec{k}_0\cdot\vec{r}_{core}} \left\langle f \left| e^{i\vec{k}_0\cdot\vec{r}_e} \left(\vec{e}_0 \hat{p}\right) \right| i \right\rangle + E_h e^{i\vec{k}_h\cdot\vec{r}_{core}} \left\langle f \left| e^{i\vec{k}_h\cdot\vec{r}_e} \left(\vec{e}_h \hat{p}\right) \right| i \right\rangle . \quad (3.7)$$

The incident and reflected waves travel with the wave vectors $\vec{k}_0$ and $\vec{k}_h$, and polarization vectors $\vec{e}_0$ and $\vec{e}_h$, respectively. $\hat{p} = (\hbar/i)\bigtriangledown$ is the momentum operator, $\vec{r}_{core}$ is the position vector of the centre of the atom and $\vec{r}_e$ is the position of the absorbing electron relative to the centre of the atom. The first term of equation (3.7) corresponds to the incident wave and the second to the reflected wave.

The reason for the different angular distributions of the ingoing and outgoing waves, is due to the fact that the PE-matrix element cannot be sufficiently described within the so-called *dipole approximation*, for which the PE-yield is identical for the incoming and outgoing x-rays. Higher order terms have to be taken into account. This is done in the so-called *quadrupole approximation.*

Dipole and quadrupole approximation for the photoelectric process

Considering only one direction of the photons, i.e., either the incident or the reflected wave, exciting the photoelectric process, the exponential function in the term of equation (3.7)

$$\left\langle f \left| e^{i\vec{k}\cdot\vec{r}} \left(\vec{e}_0 \cdot \hat{p}\right) \right| i \right\rangle$$

can be expanded in a Taylor series:

$$e^{i\vec{k}\vec{r}} = 1 + i\vec{k}\cdot\vec{r} - \frac{1}{2}\left(\vec{k}\cdot\vec{r}\right)^2 - ... \quad (3.8)$$

Using only the first two terms, the matrix element becomes [Var 05]:

$$\begin{aligned}
& \left\langle f \left| e^{i\vec{k}\cdot\vec{r}} \left(\vec{e}_0 \hat{p}\right) \right| i \right\rangle && (3.9)\\
\Rightarrow \; & \left\langle f \left| \left(1 + i\vec{k}\cdot\vec{r}\right) \left(\vec{e}_0 \hat{p}\right) \right| i \right\rangle && (3.10)\\
= \; & \left\{ im\omega \left\langle f \left| \left(\vec{e}_0 \cdot \vec{r}\right) \right| i \right\rangle \right\}_{\text{el. dipole}} - \left\{ (m\omega/2) \left\langle f \left| \left(\vec{k}\cdot\vec{r}\right) \left(\vec{e}_0 \cdot \vec{r}\right) \right| i \right\rangle \right\}_{\text{el. quadrupole}} \\
& + \left\{ (i/2) \left\langle f \left| \left[\vec{k} \times \vec{e}_0\right] \hat{L} \right| i \right\rangle \right\}_{\text{mag. quadrupole}} && (3.11)
\end{aligned}$$

where $\hat{L}$ is the angular momentum operator [VarZeg 00].

In this equation, the first term corresponds to the electric dipole transition, the second to the electric quadrupole and the third one to the magnetic dipole transition. For the photoelectric effect, the magnetic transitions can be neglected[1] [VarZeg 00].

With the initial and final state wave functions $|i\rangle$ and $|f\rangle$ in polar coordinates, equation (3.9) can be written as [Coo 93]:

$$\begin{aligned}
\frac{dY}{d\Omega} \;\propto\; & \frac{d\sigma}{d\Omega} = \left(\frac{d\sigma}{d\Omega}\right)_{\text{dipole}} + \left(\frac{d\sigma}{d\Omega}\right)_{\text{quadrupole}} \qquad (3.12)\\
= \; & \frac{\sigma}{4\pi} \left[\left\{1 + \beta P_2\left(\cos\theta\right)\right\}_{\text{dipole}} + \left\{ \left(\delta + \gamma \cos^2\theta\right) \sin\theta \cos\phi \right\}_{\text{quadrupole}} \right],
\end{aligned}$$

where $P_2\left(\cos\theta\right) = \left(3\cos^2\theta - 1\right)/2$ is the second order Legendre polynomial and θ is the angle between the x-ray polarization vector $\vec{e}_0$ and the direction $\vec{k}_f$ of propagation of the photoelectron. β varies from -1 to 2 depending on the relative amplitude and the phase shift between the matrix element for the $\Delta l = +1$ and $\Delta l = -1$ allowed dipole transitions. ϕ is the azimuthal angle between the reflected photon wave vector $\vec{k}_h$ and the photoelectron momentum $\vec{k}_f$ in the plane perpendicular to the polarization vector. The δ and γ parameters determine the quadrupole contribution to the PE yield. In equation (3.12) $\frac{d\sigma}{d\Omega}$ is the differential photoelectron cross section and σ is the total cross section

---

[1] For a central-field model and a one-electron approximation, the magnetic transition probability for the photoelectric effect is equal to zero due to the orthogonalitiy of the initial and final state radial wave functions. If core relaxations are taken into account, the probability for magnetic transitions does no longer vanish, but it is still much smaller than the electric quadrupole contributions [Var 05].

of a core level photoelectron excitation.

In the dipole approximation, only the electric dipole transition is considered. In the quadrupole approximation, the electric quadrupole transition is considered in addition to the dipole transition. The difference between these two approximations is demonstrated in figure 3.3. The angular distribution of the dipole approximation, which is the same for the incoming and outgoing x-rays, is shown in black color. The angular distribution of the quadrupole approximation is shown in light grey color for the incoming and in dark grey color for the outgoing x-rays. They differ significantly from each other.

Using the dipole approximation for the evaluation of the PE yield in a NIXSW experiment, the standing wave equation (3.5) can be directly employed with no corrections. However, with using the quadrupole contributions (which is necessary in many cases), the angular distributions of the photoelectrons for the incoming and the outgoing beam differ significantly from each other. In order to take this effect into account in the evaluation of the XSW data, equation (3.5) has to be modified.

Quadrupole parameters in the XSW equation

As discussed above, in order to correctly describe the photoelectron yield in a standing wave experiment, a modification has to be made to equation (3.5). Woodruff et al. describe these changes in the following way [Woo 05]:

$$\frac{dY}{d\Omega} \propto 1 + RS_R + 2C_F\sqrt{R}\,|S_I| \cdot \cos(\nu - 2\pi C_P + \psi). \tag{3.13}$$

With the unit wave vectors of the incident and reflected beam, $\vec{s}_0 = \frac{\vec{k}_0}{|\vec{k}_0|}$ and $\vec{s}_h = \frac{\vec{k}_h}{|\vec{k}_h|}$, respectively, the (direct reflection) term S_R becomes

$$S_R = \frac{|M_{fi}\,(\vec{s}_h)|^2}{|M_{fi}\,(\vec{s}_0)|^2}.$$

The complex interference term S_I becomes

$$S_I = |S_I| \, e^{i\psi} = \frac{M_{fi}(\vec{s}_0) * M_{fi}(\vec{s}_h)}{|M_{fi}(\vec{s}_0)|^2}. \tag{3.14}$$

In the dipole approximation, the matrix elements for the incident and reflected wave are identical, i.e. $M_{fi}(\vec{s}_0) = M_{fi}(\vec{s}_h)$, and consequently the values of S_R and S_I in equation (3.13) are equal to 1. In the quadrupole approximation[2] S_R and S_I differ from 1, and the phase ψ differs from zero (see equation (3.14)).

Different notations for the description of S_R and S_I are found throughout in the literature. Following the paper of Nelson et al. [Nel 02], the complex interference term $S_I = |S_I| \, e^{i\psi}$ has the magnitude $|S_I| = \frac{\sqrt{1+q^2 \sin^2 \Delta}}{1-q \cos \Delta}$ with the quadrupole amplitude parameter q and the phase $\tan \psi = q \sin \Delta$. The term of the direct reflection is quoted $S_R = \frac{1+q \cos \Delta}{1-q \cos \Delta}$. Herein, the quadrupole amplitude parameter q is defined as

$$q = 2 \frac{|M_{\text{quadrupole}}|}{|M_{\text{dipole}}|} = 2 \frac{|\langle f \, | i k_{0,h} (\vec{s}_{0,h} \cdot \vec{r}_e)(\vec{e}_{0,h} \cdot \hat{p}) | \, i \rangle|}{|\langle f \, | \vec{e}_{0,h} \hat{p} | \, i \rangle|}. \tag{3.15}$$

One can define a phase shift between the complex dipole and the complex quadrupole matrix element. With $M_{\text{dipole}} = |M_{\text{dipole}}| \, e^{i\phi_d}$ and $M_{\text{quadrupole}} = |M_{\text{quadrupole}}| \, e^{i\phi_q}$ the phase shift is

$$\Delta = \phi_q - \phi_d. \tag{3.16}$$

Due to the quadrupole contribution, the modified standing wave equation (3.13) has three additional variables S_R, $|S_I|$, and ψ. As shown above, only two of them are independent. The parameters alternatively can be expressed with two parameters, namely the quadrupole amplitude parameter q and the phase shift Δ. Therefore, when evaluating a standing wave experiment, these parameters have to be identified.

---

[2] Higher non-dipolar terms are not considered. Trzhaskovskaya et al. calculated the parameters for higher non-dipolar terms. For outer shells, these contributions become noticeable, even at low energies [Trz 06]. However, in this work only 1s shells are considered.

Phenomenological forward/backward asymmetry parameter

One experimental way to partly identify the multipole parameters lies in the determination of the phenomenological forward / backward asymmetry which can be described by the parameter Q. The photoelectron yield for the incident x-rays correspond to $I(1-Q)$, and the yield for the reflected wave correspond to $I(1+Q)$. For the experimental setup used in the present work, the relation of Q and the angular PE distribution will be given in the following based on equation (3.12).

Referring to equation (3.13), Q can be related to the interference term S_I and to the reflection term S_R in the following way:

$$Q = q \cos \Delta \tag{3.17}$$

with $S_R = \frac{1+Q}{1-Q}$ and $|S_I| = \frac{\sqrt{1+Q^2 \tan^2 \Delta}}{1-Q}$ and the phase $\psi = \arctan(q \sin \Delta) = \arctan(Q \tan \Delta)$.

Considering one x-ray beam which is not reflected, the electron yield can be written as follows (for linear polarization, or σ-polarization)

$$\begin{aligned} \frac{dY}{d\Omega} &\propto |M_{\text{dipole}}|^2 (1-Q) && (3.18) \\ &\propto 1 + \beta P_2(\cos\theta) - \left(\delta + \gamma \cos^2\theta\right) \sin\theta \cos\phi. && (3.19) \end{aligned}$$

With $|M_{\text{dipole}}|^2 \propto 1 + \beta P_2(\cos\theta)$ the asymmetry parameter Q can be written as

$$Q = \frac{(\delta + \gamma \cos^2\theta) \sin\theta \cos\phi}{1 + \beta P_2(\cos\theta)}. \tag{3.20}$$

For the photoelectron emission[3] from an s-state, $\delta = 0$ and $\beta = 2$ [Trz 01], hence equation (3.20) becomes

$$Q = \frac{(0 + \gamma \cos^2\theta) \sin\theta \cos\phi}{1 + \frac{2}{2}(3\cos^2\theta - 1)} = \frac{\gamma \sin\theta \cos\phi}{3}. \tag{3.21}$$

---

[3] Depending on the energy, the value β differs from $\beta = 2$ in a relativistic calculation. For the investigated O1s and C1s transitions at a photon energy of 2.6 keV one calculates $\beta \approx 1.976$ [Trz 01]. In the following this small difference from 2 is neglected. However, for outer s-shells of heavy atoms, the parameter β changes drastically with energy.

In this work, only XSW experiments with normal incidence are considered, therefore the angle ϕ is 0° for the incident and 180° for the reflected beam. The angle θ was 45°. Introducing these values into equation (3.21), the parameter Q can be evaluated for the incident (i) beam to

$$Q = Q_i = \frac{\gamma \sin\theta}{3} = 0.2357 \cdot \gamma, \tag{3.22}$$

and for the reflected beam (r) to

$$-Q = Q_r = -Q_i = -\frac{\gamma \sin\theta}{3} = -0.2357 \cdot \gamma, \tag{3.23}$$

respectively.

3.3.2 Experimental determination of Q

The asymmetry parameter Q can be derived by calculations or can be experimentally determined. Ideal conditions for measuring the anisotropy factor Q are given by incoherent films, which can be produced by growing a multilayer on the surface. For multilayers, it is assumed that the atomic distribution is random with respect to the diffraction planes of the substrate.

Another way to measure on an incoherent atomic distribution is the tilting of the crystal-surface normal with respect to the beam. In this case, a particular Bragg reflection is used for which the reflecting lattice planes are tilted to the surface normal. A monolayer or multilayer film, adsorbed on the crystal-surface, is consequently also tilted with respect to the reflecting lattice planes. Therefore, under such experimental conditions these films become incoherent to x-ray standing waves.

The point for the use of incoherent films is that the coherent fraction C_F in equation (3.13) becomes 0. Therefore, the measured electron yield should follow the following function:

$$\frac{dY}{d\Omega} \propto 1 + RS_R = 1 + R \cdot \frac{1+Q}{1-Q}. \tag{3.24}$$

In a XSW experiment, the reflectivity R is directly measured as will be shown in section 3.4. Therefore, by fitting equation (3.24) to the experimental data, the parameter Q can be determined.

3.3.3 Quadrupole parameters in literature

The correct choice of the quadrupole parameters is of important consequence for the results of an x-ray standing wave experiment. In literature many different values have been published for the asymmetry parameter Q. Depending on the photon energy and on the experimental setup, differences in the values are expected. However, for a particular experimental setup (and a particular photon energy), of course only one value should be appropriate for Q. By transforming the values from literature to the experimental setup and photon energy used in the present work, a large spread can be observed in the resulting values for the parameter Q (see figure 3.4).

In the following, an overview is given on the determination and on the corresponding values for the multipole parameter Q found in literature. In detail, only values for C1s and O1s will be considered due to their relevance for the present work. In addition comments on the methods of determination and the uncertainties of these methods will be shortly discussed.

In 1989 Bechler and Pratt [BecPra 89] presented nonrelativistic calculations for the multipole corrections of the dipolar angular distribution. However, for a long time, it was not realized that this effect is also important for rather small x-ray energies (around 3 keV and lower). For example, the correction for the C1s transition at a photon energy of 2 keV turned out to be $Q = 0.23$ (for $\theta = 45°$ as in this work). That means that the PE yield is 23% higher for the photoelectron excited by the reflected beam and 23% lower for the photoelectrons excited by the incident beam. However, the total cross section is not much affected by these corrections. Since only the influence on the total cross section σ was investigated so far, the strong influence on the angular cross section $\frac{d\sigma}{d\Omega}$ was not considered for a long time.

In 1993, Cooper calculated the quadrupole asymmetry parameters for the inert gas atoms in the energy range up to 5 keV [Coo 93]. In another theoretical study, Vartanyants et al. estimated the multipole contributions to be small [VarZeg 97]. However, in 1998, Fisher et al. published a study, where they showed the strong influence of the asymmetry parameters onto the experimental XSW results for the first time. They investigated the element Iodine in the system Cu(111)$(\sqrt{3} \times \sqrt{3})R30°$-I [Fis 98]. For the determination of the asymmetry parameters, they compared Auger XSW results with results from photoemission. The angular distribution of the Auger electrons is independent of the direction of the x-ray beam, therefore the Auger electron yield was directly taken for the XSW evaluation, without any further corrections. However, in this investigation, the electron stimulated Auger electrons were not considered (see [ShaCow 98]), which have a direct influence on the result for the asymmetry parameters. Thus, the values for Q, determined by this method, have to be dealt with some caution. Nevertheless, the strong influence of Q on the XSW results was demonstrated for the first time.

Stanzel et al. presented an alternative way for the evaluation of the Auger electron yield [Sta 04]. In their work, the electron induced Auger electrons were considered. By comparing the corrected XSW Auger results with the PE results, they determined the non-dipolar parameter Q. However, this method only gives an estimation of the non-dipolar parameters. The reason for this is that four parameters have to be determined from only two XSW profiles (for the Auger and the PE yield). The four parameters correspond to the contribution of the electron-induced Auger yield, to the multipole parameter Q and to the values of the coherent position and coherent fraction of the investigated system (the phase Δ was assumed to be known). In the work from Stanzel an error in the fitting routine for the fit of the XSW profiles was found. Therefore, the estimation of the non-dipole parameters comes out wrong [Sta 07][4].

Jackson et al. determined the asymmetry parameter in a different way [Jac 00]. By growing films which are incoherent with the underlying crystalline substrate, namely disordered films or multilayer films with a negligible coherent fraction, they obtained the parameters for the photoemission from core levels

---

[4] In the work of Stanzel, the sign of ψ in equation (2) is wrong. This leads to an error in the values for the non-dipole parameters fitted with this routine. See equation (3.13) in this chapter.

of s symmetry for C, O and P 1s. In subsequent publications, the same authors revised their results. Due to an error in the fitting routine, the values for Q came out to be too low (see [Woo 05] and [Lee 01]).

In 2000, Vartanyants and Zegenhagen published a theoretical work about the photoelectron emission in a x-ray standing wave field. They especially studied the influence of the multipole terms on the scattering process and compared the different polarizations [VarZeg 00].

Relativistic calculations of the multipole parameters were done by Trzhaskovskaya, Nefedov and Yarzhemsky for the elements of $Z = 1$ to 54 [Trz 01].

For the 1s PE of carbon and oxygen, Schreiber et al. measured the asymmetry parameter with the method of incoherent films [Sch 01]. They used the same system as it was done in the present work, namely multilayers of PTCDA on Ag(111). Therefore, the result of $Q_{\mathrm{O1s,\ C1s}} = 0.31$ is especially interesting for the present work.

Nelson, Woicik, Pianetta, Vartanyants and Cooper investigated the quadrupole effects on crystalline Ge [Nel 02]. They placed a shutter in front of the analyzer. By comparing the azimuthal angle resolved and azimuthal angle-averaged electron yields, the multipole parameters were determined. The authors emphasize the importance of the phase shift Δ for the result. However, one year earlier, Lee et al. proposed that this phase shift can be neglected [Lee 01]. In their paper, they experimentally determined the quadrupole parameters for the 1s PE at photon energies around 3 keV for first and second row elements from C to Cl. Again, by growing incoherent thick films of various systems on Cu(111) and Al(111) substrates, the parameter Q was determined.

In table 3.1, the experimental and theoretical results from literature for the O1s and the C1s electron transition are given. For a better overview, the results are adapted to the experimental geometry of this work[5] with $\theta = 45°$. The original values, given in the papers, are listed in appendix B.

Within the present work, the parameter Q was determined. However, the analyzed data obviously did not represent incoherent films. The evaluation is shown in appendix C. It could not be used for the determination of the asymmetry parameter Q.

---

[5] Using $Q = \frac{\gamma \sin\theta}{3}$.

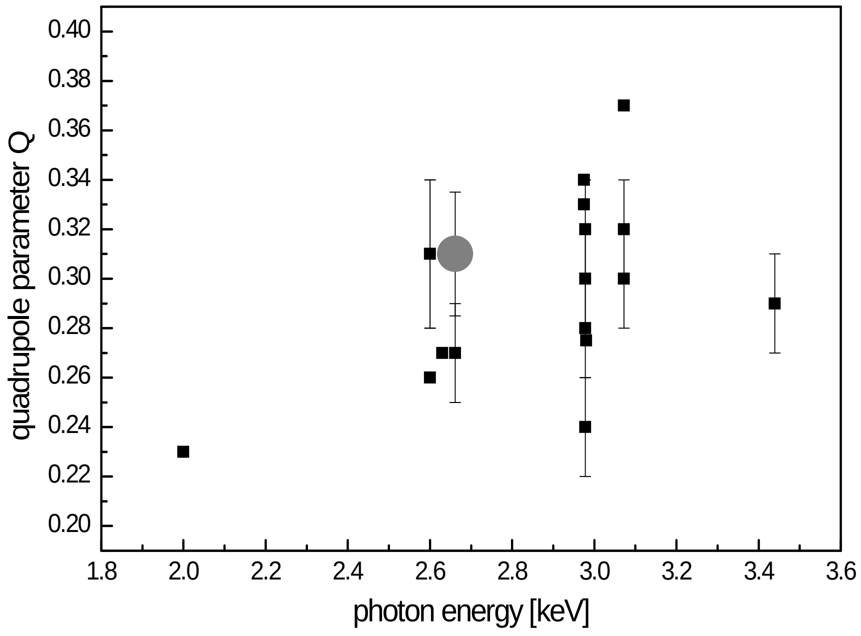

Figure 3.4: *Values of the quadrupol parameter Q for the O1s and C1s transitions taken from literature. They were converted to the detector geometry of the experiment of this work. The value Q=0.31 (grey circle) was used in the present work for both transitions.*

In figure 3.4, the spread of the reported values of Q can be seen. The theoretically calculated values for Q are significantly lower than the experimentally determined values. It seems to be obvious that the Q-values, derived from theory, are underestimated. Regarding the large spread of values for the same photon energy, it appears that Q must also depend on other factors than only the photon energy. These could be due to the substrate itself, or to the structural order of the film, or to the fact whether one measures on a monolayer or on a multilayer film.

The other multipole parameter, which was needed in this work is the phase shift Δ. It has only been determined theoretically, until now [Lee 01] [Jab 03]. In table 3.2 the values for Δ were taken from the NIST electron elastic scattering cross section database [Jab 03].

The values for the parameter Δ used in the present work are based on calculations done by Lee et al. [Lee 01]. The total range of the calculated values of Δ for O1s and C1s extends from -0.20 to -0.35 (in the photon energy range of approximately 2.2 keV to 2.7 keV).

Q in literature

author	**method**	**transition**	**energy** (keV)	$\mathbf{Q}(\boldsymbol{\theta} = \mathbf{45}^\circ)$
Bechler [BecPra 89]	theor.	C1s	2.0	0.23
Jackson [Jac 00]	exp.	O1s	2.975	(0.25)
	exp.	O1s	3.046	(0.22)
Jackson [Jac 00] corrected by Lee [Lee 01]	exp.	C1s	2.978	0.30 ± 0.02
	exp.	C1s	2.978	0.32 ± 0.02
Lee [Lee 01]	exp.	O1s	2.661	0.27 ± 0.02
	exp.	O1s	2.978	0.28 ± 0.02
	exp.	O1s	3.072	0.30 ± 0.02
	exp.	O1s	3.439	0.29 ± 0.02
	exp.	C1s	2.661	0.31 ± 0.025
	exp.	C1s	2.978	$0.24/0.28 \pm 0.02$
	exp.	C1s	3.072	$0.32/0.37 \pm 0.02$
	exp.	C1s	3.439	(0.17)
Trzhaskovskaya [Trz 01]	theor.	O1s	2.6	0.26
	theor.	C1s	2.6	0.26
Schreiber [Sch 01]	exp.	O1s	2.6	0.31 ± 0.03
	exp.	C1s	2.6	0.31 ± 0.03
Stanzel [Sta 04]	exp.	O1s	2.6	(0.26)
Schulte [Sch 05b]	exp.	O1s	2.6	0.31
Jackson [Jac 00] corrected by Woodruff [Woo 05]	exp.	O1s	2.975	0.34.
	exp.	O1s	2.975	0.33
Gerlach [Ger 05]	exp.	C1s	2.980	0.275
Stadler [Sta 06]	exp.	C1s	2.6	0.24 ± 0.02
Gerlach [Ger 07]	appl.	O1s	2.63	0.31
	appl.	C1s	2.63	0.31
	appl.	O1s	2.98	0.26
	appl.	C1s	2.98	0.30
Stadler [Sta 07]	exp.	O1s	2.6	0.27
	appl.	C1s	2.6	0.27

Table 3.1: *Overview on quadrupole parameter Q for the O1s and C1s transitions found in literature. The parameter Q depends on the photon energy. The values are converted to an experimental setup with the electron analyzer placed 45 degrees with respect to the x-ray beam. The Q-values given in brackets appeared to be wrong (see text). The second column denotes the method of the determination of the non-dipolar parameters (experimentally, theoretically, or if the specific values of Q were only applied in the evaluation presented in the noted reference). Comments to the values and to the experimental conditions are given in the appendix.*

phase shift parameter Δ

[Jab 03]

photon energy	Δ_{O1s}	Δ_{C1s}
50 eV	1.5724	2.0132
2630 eV	-0.2674	-0.2007
10000 eV	-0.1440	-0.1096

[Lee 01]

photon energy	Δ_{O1s}	Δ_{C1s}
2630 eV	-0.33	-0.22

Table 3.2: *Values for the phase shift parameter Δ for different photon energies, taken from the NIST database [Jab 03] and from the paper of Lee et al. [Lee 01].*

3.3.4 Quadrupole parameters used in the present work

For the evaluation of an XSW experiment, it can be crucial to choose the correct quadrupole parameter. For the present work, it seemed to be most reasonable to use the Q values Schreiber et al. derived on incoherent multilayers of the same material on the same substrate, PTCDA on Ag(111) [Sch 01]. For Δ, the theoretically derived values by Lee et al. were used [Lee 01]. The quadrupole parameters used in the present work are summarized in table 3.3.

For the fit of the photoelectron- NIXSW profiles the following formula was applied:

$$Y \propto 1 + RS_R + 2C_F\sqrt{R}\,|S_I| \times \cos(\nu - 2\pi C_P + \psi). \tag{3.25}$$

By varying the values of coherent fraction C_F and the coherent position C_P in the fitting routine, the calculated curve is fitted to the experimental data.

quadrupole parameters
(for the experimental geometry of this work
$\boldsymbol{\theta} = \mathbf{45}^\circ$, $\boldsymbol{\phi}_{\text{incident}} = \mathbf{0}^\circ$, $\boldsymbol{\phi}_{\text{reflected}} = \mathbf{180}^\circ$)

parameter	transition C1s	 O1s
$\boldsymbol{\Delta}$	$\mathbf{-0.22}$	$\mathbf{-0.33}$
$\boldsymbol{\gamma}$	**1.32**	**1.32**
$\boldsymbol{\delta}$	**0**	**0**
$\boldsymbol{\beta}$	**2**	**2**

derived parameter	C1s	O1s
$Q\,(\theta, \gamma, \phi, \delta, \beta)$	0.31	0.31
$q = \frac{Q}{\cos \Delta}$	0.318	0.328
$S_R = \frac{1+Q}{1-Q}$	1.900	1.900
$\lvert S_I \rvert = \frac{\sqrt{1+Q^2 \tan^2 \Delta}}{1-Q}$	1.453	1.457
$\psi = \arctan(Q \tan \Delta)$	-0.069	-0.106

Table 3.3: *Quadrupole parameters used in this work. The parameters, shown in the upper table (bold letters), are independent of each other. See text for references.*

3.3.5 Error estimation: influence of the multipole parameters

Depending on the position of the detector, a backward / forward asymmetry exists. Hence, for light elements, as for C or O, the XSW result can be strongly falsified, if this asymmetry in the angular distribution is neglected. The resulting values for the coherent positions and the coherent fractions can be underestimated or overestimated more or less strongly by only using the dipole approximation. This effect depends on the actual coherent position and coherent fraction of the investigated system. Therefore, the size of the error cannot be predicted in advance. [Lee 01].

For the evaluation, particular values of the quadrupole parameters Q and Δ were selected. It is not clear, if those values are the correct multipole parameters. Depending on the values for C_F and C_P, a small difference in the multipole parameters can influence the results more or less strongly [Lee 01].

In order to test this influence, the quadrupole parameters were changed systematically and fitted to the experimental data.

In the fitting routine the parameters S_R, $|S_I|$ and ψ were employed which depend on Q and Δ. Rewriting the corresponding equation (3.25) as a function of Q and Δ gives:

$$Y \propto 1 + R\frac{1+Q}{1-Q} + 2C_F\sqrt{R}\frac{\sqrt{1+Q^2\tan^2\Delta}}{1-Q} \cdot \cos(\nu - 2\pi C_P + \arctan(Q\tan\Delta)). \tag{3.26}$$

The phase ψ

The phase $\psi = \arctan(Q\tan\Delta)$ strongly depends on Q and Δ. The influence of Q and Δ on ψ is shown in figure 3.5.

For the results of this work, it appeared to be advantageous to work with the effective coherent position $C_{P,\mathrm{eff}}$. Due to the uncertainty in the multipole parameters, the variations in the coherent positions (in the present work) are mainly dependent on the phase ψ. By neglecting the phase ψ (i.e. setting $\psi = 0$) , the fitting routine does not change. Assuming the chosen value for Q

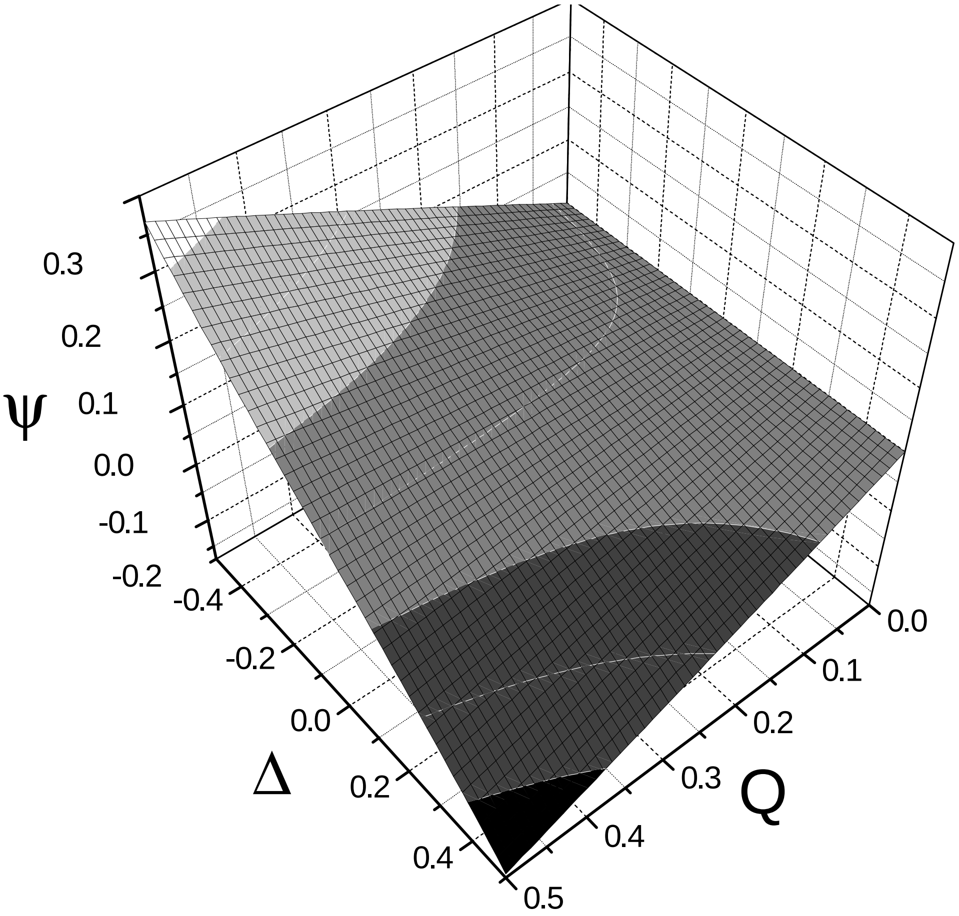

Figure 3.5: *The plane represents the resulting values for the phase ψ depending on the multipole parameters Q and Δ.*

to be true and provided that the exact phase Δ is known, the correct coherent position C_P can be calculated from the effective coherent position as:

$$C_P = C_{P,\text{eff}} + \psi/2\pi.$$

The negligence of the phase ψ in $C_{P,\text{eff}}$ leads to a shifted value for the coherent positions, depending on the size of ψ. In table 3.4, this shift due to the distinct values of ψ is given.

error estimation for C_P due to the phase ψ

	$Q\,(\theta = 45°)$	ψ	error of C_P $C_P = \psi/2\pi$	error of C_P in Å
C1s: $\Delta = -0.22$	0.24	−0.054	−0.009	−0.020
Lee et al. [Lee 01]	0.31	−0.069	−0.011	**−0.026**
	0.34	−0.083	−0.013	−0.031
C1s: $\Delta = -0.19$	0.24	−0.046	−0.007	−0.017
Gerlach et al. [Ger 05]	0.34	−0.071	−0.011	−0.027
O1s: $\Delta = -0.33$	0.26	−0.089	−0.014	−0.033
Lee et al. [Lee 01]	0.31	−0.106	−0.017	**−0.040**
	0.34	−0.116	−0.018	−0.044

Table 3.4: *Possible values for the systematical errors in the coherent position, due to the disregard of the phase in the XSW equation. The error of the coherent position in the last column is calculated with the distance of the Ag(111) lattice planes. The bold values for C1s and O1s correspond to the necessary correction of the effective coherent positions obtained in this work, provided that the chosen multipole parameter correspond to the correct values.*

Systematic errors due to the multipole parameters Δ and Q

The errors of the results due to uncertainties of Q and Δ are strongly coupled to the actual coherent positions and coherent fractions. In order to estimate the error range for the results of this work, different multipole parameters were tested on the data of this work.

The parameter Δ is found in the interference term $|S_I| = \frac{\sqrt{1+Q^2 \tan^2 \Delta}}{1-Q}$. In order to test its influence on the XSW results, the parameter Δ was tentatively set to zero in a fit of one exemplary C1s XSW profile. The data were fitted with various values of Q. A second fitting series was done with non-zero values of Δ, here the values derived by Lee et al. [Lee 01] were taken. In both cases the phase ψ was set equal to zero, yielding an effective coherent position $C_{P,\text{eff}}$. No change in the effective coherent position $C_{P,\text{eff}}$ was observed. In the values of the coherent fraction C_F, only a small difference of less than 3% was found (see figure 3.6b).

As can be seen from table 3.1, the proposed values for $Q\,(\theta = 45^\circ)$ at an energy around $E = 2.6\,\mathrm{keV}$ vary from $Q = 0.26$ to $Q = 0.34$ for the O1s transition, and from $Q = 0.24$ to $Q = 0.37$ for the C1s transition. In order to test the influence of Q on the XSW results, a systematic variation of Q in the range of $Q = 0.20$ to $Q = 0.36$ was done. Fits of three different O1s XSW profiles were conducted with the various Q values (see figure 3.6a). In agreement with Lee at al. [Lee 01], for the data of the present work only a small influence of Q on $C_{P,\mathrm{eff}}$ was found. The maximal deviation occurred to be $\Delta C_{P,\mathrm{eff}} = 0.025$, in the most cases the deviation is below $\Delta C_{P,\mathrm{eff}} = 0.014$ which is in the range of the statistical errors of the data. The influence of Q on the C_F values is significantly larger, partially yielding C_F values which are too large and hence are not plausible (not shown here). This latter effect has to be attributed to incorrect values for Q. Hence, values of $Q \leq 0.26$ (for the experimental setup and photon energies used in the present work) have to be considered as to be too low leading to unphysical results, although these values are theoretically predicted.

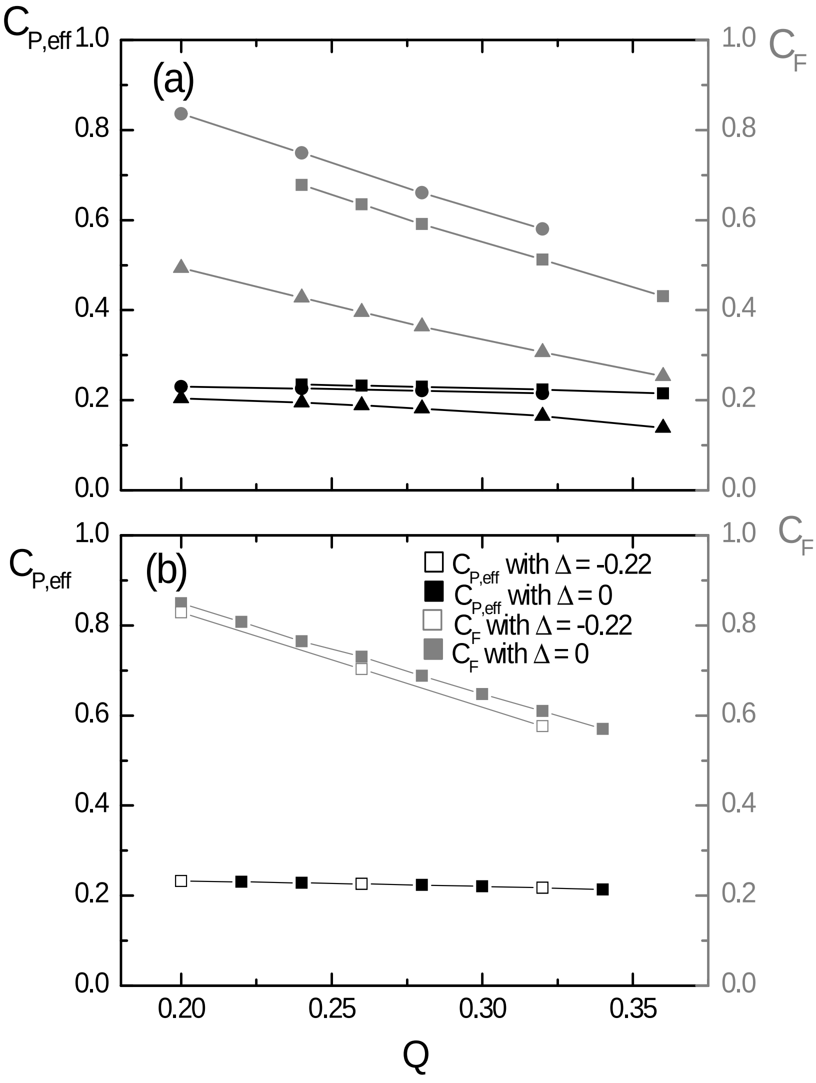

Figure 3.6: *Results for the effective coherent position (black) and the coherent fraction (grey) by fitting the calculated curves to the experimental data (monolayer at room temperature). The asymmetry parameter Q was set to different values in the fitting routine. a) Fit results for 3 different O1s data sets. The coherent position only exhibits a small deviation, whereas the coherent fraction is very sensitive to the change. b) Fit results for one C1s data set. The open symbols represent the results with $\Delta = -0.22$, the solid symbols represent the results with $\Delta = 0$. It can be clearly seen that the influence of Δ (in the tested range) on $C_{P,eff}$ is negligible.*

3.4 Experimental

The NIXSW experiment was conducted at the European Synchrotron Radiation Facility (ESRF) in Grenoble in France. By circulating high-energy electrons (6 GeV), synchrotron light is produced in the large storage ring (844 m circumference) of the synchrotron. The experimental setup is located at the end station of the undulator beamline *ID32*, which has a spectral range from 2.5 keV to 30 keV. The photon energy can be tuned by two piezo motors, which move a Si(111)-monochromator crystal ($\Delta E/E = 10^{-4}$). The synchrotron beam is guided to the ultra-high vacuum (UHV) chamber which is equipped with a hemispherical electron analyzer, a LEED optics, an ion gun, a quadrupole mass spectrometer, and gas lines for sample preparation. The sample is mounted on a manipulator with three translational and two angular degrees of freedom. Thereby, the sample can be moved to various positions, needed for preparation (i.e. LEED, ion sputtering, sample heating, evaporation) and measurements.

For the experiments in this work, the Ag(111) crystal had to be azimuthally oriented in the sample holder. Otherwise, the Bragg reflection of the $(\bar{1}11)$ planes could not have been investigated. This orientation had to be done, because the azimuthal rotation of the sample ($\bar{\theta}$) is only possible up to a few degrees. In order to use a $(\bar{1}11)$-Bragg reflection, the oriented crystal needs to be rotated by an angle $\phi = 70.5°$ perpendicular to the beam. If not oriented properly, the $(\bar{1}11)$-Bragg reflection could eventually not be measured, because the possible rotation $\bar{\theta}$ on the manipulator is too small.

Before reaching the UHV chamber, the synchrotron beam passes a horizontal slit with variable width from 1 mm to 1.6 mm. To measure the primary photon intensity, a mesh of aluminum (MeshI0) is put into the beam. Thereby, the intensity can be determined during the experiment. To measure the absolute intensity, a Si photodiode can be moved into the direct beam. During the experiment, the reflected beam was detected on a fluorescence screen. This is a copper plate, mounted directly behind the beam entrance of the chamber. It is covered with fluorescent phosphorus, hence the reflected beam can be easily seen by the eye (via a camera). The photo current of this plate can be

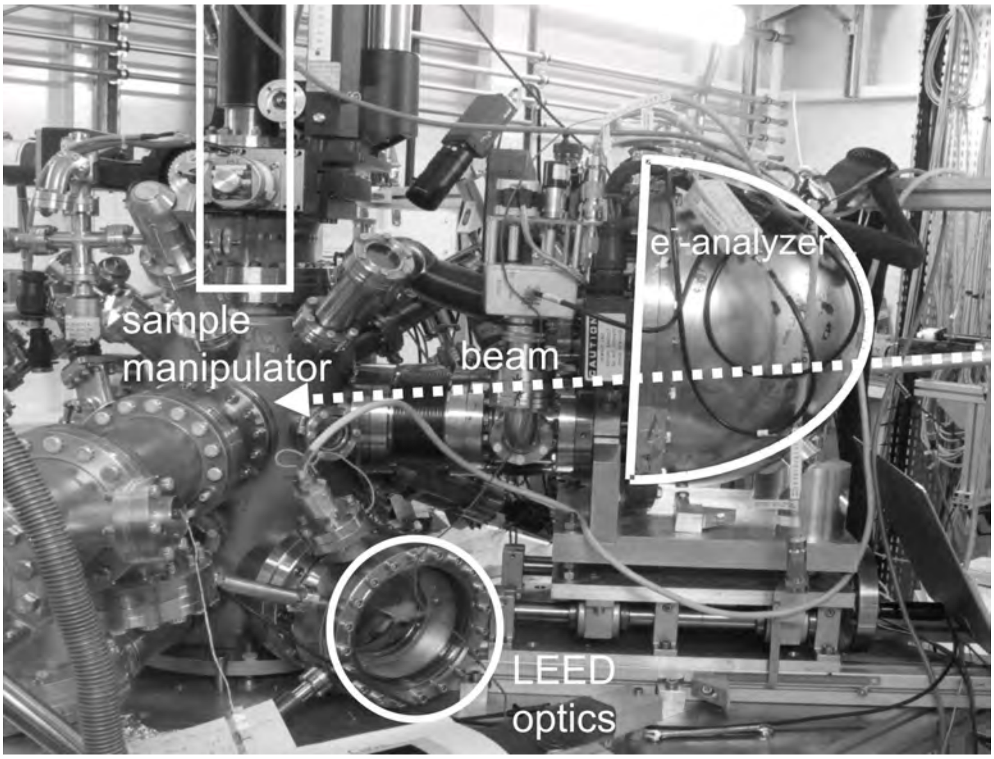

Figure 3.7: *UHV chamber used for the NIXSW experiment in Grenoble. The electron analyzer lies in the horizontal plane of the x-ray beam. In this plane they include an angle of 45 degrees.*

recorded, and the measured value is used for the reflectivity in the evaluation.

The sample can be cooled via a flexible copper wire with liquid helium or with liquid nitrogen. Thereby, temperatures of less than 90 K or less than 170 K can be achieved with liquid helium or liquid nitrogen, respectively. The pressure in the chamber during the experiments was 5×10^{-10} mbar at maximum.

The hemispherical electron analyzer was placed at 45° off the beam direction. It lies in the same horizontal plane as the photon beam.

In order to deposit the organic material on the sample, a home-built Knudsen cell was attached to the UHV chamber. The organic material was located in a glass crucible within this cell and could be resistively heated up to the evaporation temperature.

3.5 Data analysis

For the data analysis of the NIXSW experiment, first the PE yield for the particular element was determined. Therefore, the large background had to be subtracted from the PE feature of interest, as can be seen in figure 3.8. This was done with the program *PHIXPS* by T. L. Lee, or, alternatively, with the program *CasaXPS* by N. Fairly.

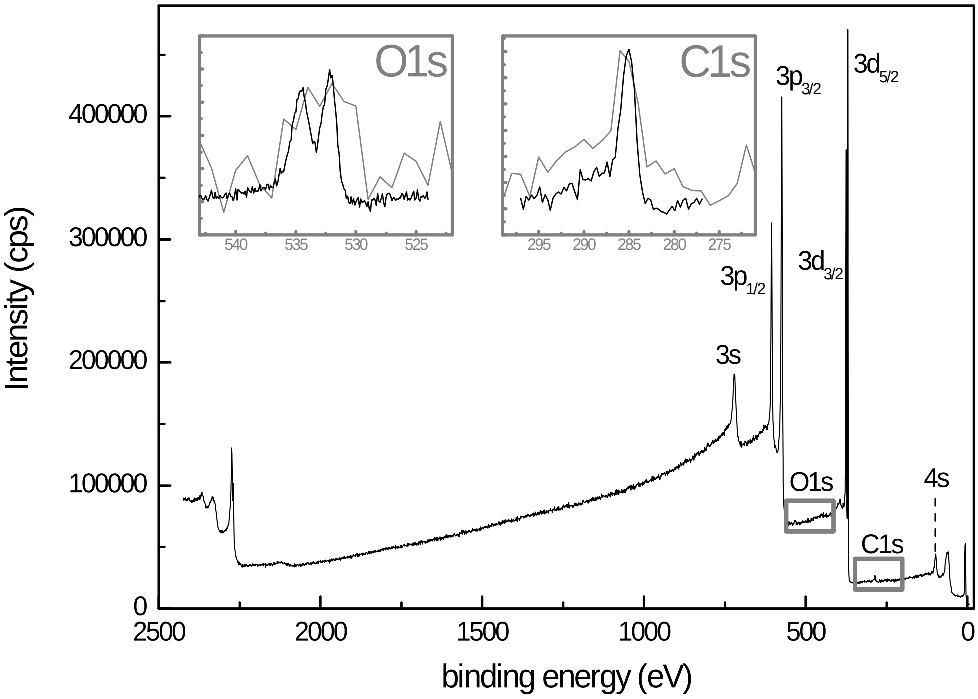

Figure 3.8: *PE survey (Off Bragg) of PTCDA on Ag(111). For the evaluation of the XSW experiment, the large background had to be subtracted from the total PE signal of the investigated electron transition (O1s and C1s). In the insets the survey spectra (grey) and the corresponding high resolution spectra (black) are shown.*

In one standing wave experiment, typically 30 to 60 PE spectra, with different photon energies around the Bragg condition, were taken. From each spectrum, the background had to be subtracted. If chemical shifted peak features occurred in the PE spectra, a peak fitting was performed, in order to separate the distinct contributions. Using the program *CasaXPS* for the peak fitting, the integral intensity was split into the different contributions. The remaining integral intensities were plotted against the photon energy. These plots are called NIXSW profiles.

Next, the NIXSW profiles were normalized with the beam intensity (meshI0). This was automatically done in the program *PHIXPS,* or by hand for profiles obtained from *CasaXPS*.

Subsequently, the program *DARE* by J. Zegenhagen was used for the fit of the NIXSW profiles for the determination of the coherent position C_P and the coherent fraction C_F. The fit was done in two steps. First, the reflectivity curves, normalized to the beam (meshI0), were fitted. Second, these curves were used for the fit of the NIXSW profiles.

The mosaic spread of the silver crystal was taken into account by using constant default values for the crystal parameters. *DARE* uses one parameter to describe the substrate *and* the experimental setup (monochromator). It is presented in Appendix D for the experiments of this work. In *DARE* the quadrupole parameters S_R, $|S_I|$ and ψ have to be set before fitting the NIXSW profiles. The multipole parameters, used in this work, are found in section 3.3.4.

3.5.1 Graphical representation of the result: the Argand diagram

The NIXSW profile of an adsorbate on multiple sites is described by equation (3.3), which is repeated here again:

$$I \propto 1 + R(\nu) + \frac{2}{N}\sqrt{R(\nu)}\sum_{i=1}^{N}\cos(\nu - 2\pi C_{P_i}). \qquad (3.27)$$

The important part of this formula is the sum $\frac{1}{N}\sum_{i=1}^{N}\cos(\nu - 2\pi C_{P_i})$ over all atom positions. It is convenient to present this result in the complex Argand diagram. In 1994 this type of diagram was introduced by Woodruff [Woo 98] for the presentation of NIXSW results, which is now commonly used. The coherent position C_P and the coherent fraction C_F are interpreted as the phase and the amplitude of the complex exponential function:

$$C_F \cdot \exp\left(2\pi i \cdot C_P\right) = \frac{1}{N}\sum_{i=1}^{N} \exp(2\pi i \cdot C_{P_i}) \qquad (3.28)$$

In an Argand diagram the imaginary axis is plotted versus the real axis. Therefore, in this diagram the XSW result correspond to a polar vector starting at the origin, the length is given by the coherent fraction C_F, and the angle is given by the coherent position $2\pi C_P$. The sum in equation (3.28) can be conveniently performed by vector addition in this diagram, as illustrated in figure 3.9.

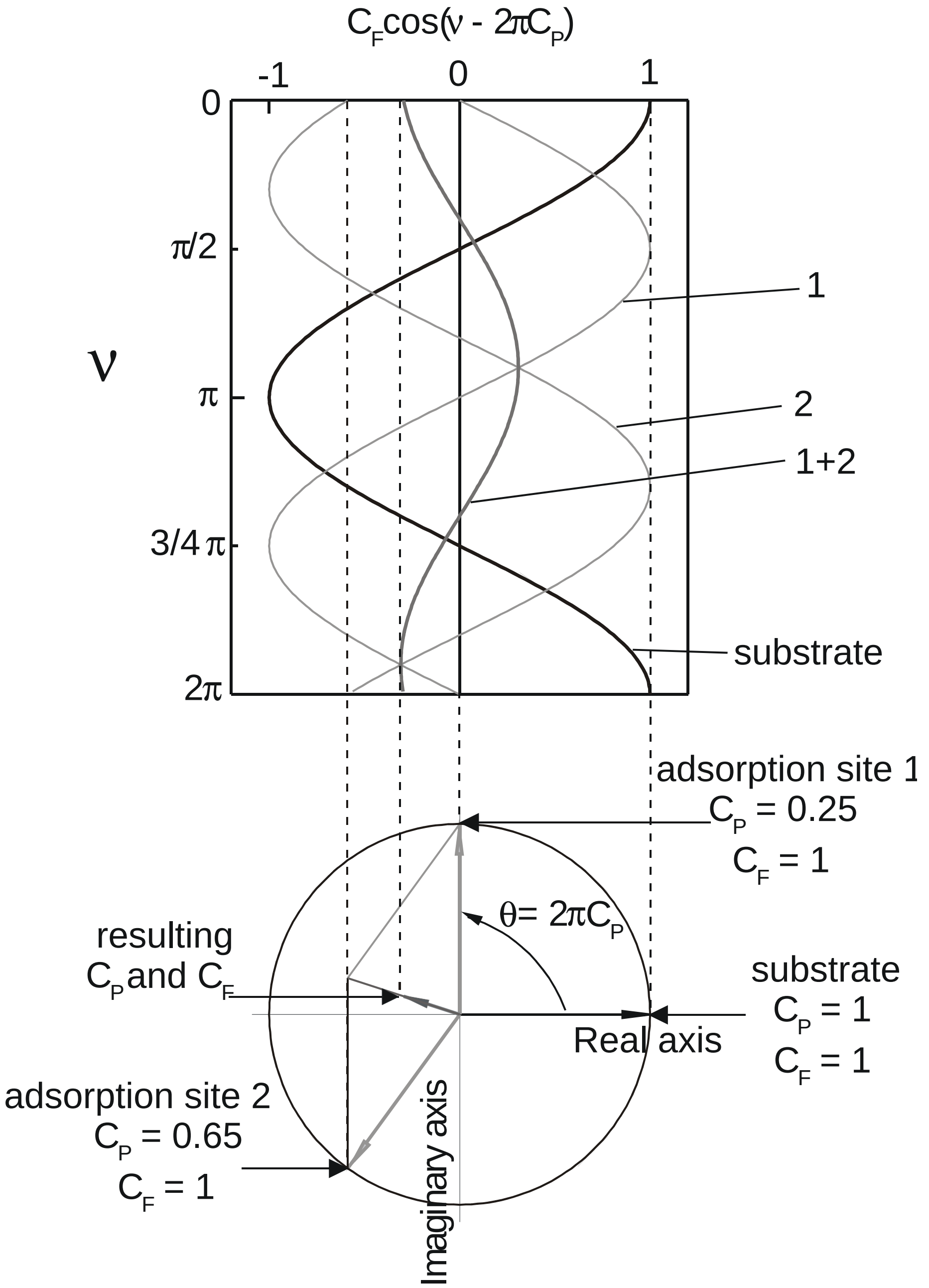

Figure 3.9: *Top: Different vertical positions of the adsorbate yield different phase shifts of the cosine function. Regarding two uniformly distributed adsorption sites (1 +2) (light grey curves), the resulting cosine function (dark grey curve) is phase shifted by* C_P *and has an amplitude of* C_F*. The thick black curve represents the cosine of the substrate. The dotted lines represent the values of* $C_F \cos(2\pi C_P)$ *for the distinct adsorption sites (Note:* $\nu = 0$*). Bottom: Argand diagram illustration. The two adsorption sites are represented by the two light grey vectors. By vector addition the resulting dark grey vector is obtained. Please note that the length of this vector is drastically reduced, the value of the coherent fraction* $C_F = 0.3$ *is very low. In this particular case of two adsorption sites, the coherent position,* C_P*, corresponds to the average vertical distance of the adsorbate.*

Chapter 4

NIXSW – the stable monolayer phase

3,4,9,10-perylenetetracarboxylic dianhydride (PTCDA) deposited on Ag(111) at room temperature adsorbs in a stable chemisorbed state with long-range structural order, forming the so-called herringbone pattern [Glö 98]. More information about the properties of this phase can be found in the chapter 2. In the following the monolayer of this room temperature phase is named just *monolayer*.

In this chapter the evaluation and the results of the NIXSW investigation on the monolayer phase of PTCDA on Ag(111) are presented.

4.1 Experimental

In order to determine the vertical distances of the atoms in the PTCDA monolayer with respect to the silver substrate, NIXSW data were taken at the ESRF in Grenoble / France at the beamline ID32. The layout of this beamline is described in chapter 3.4. Data were taken in three beamtimes, in July 2003 (J'03), November 2003 (N'03) and November 2004 (N'04). The same silver crystal and the same batch of PTCDA were used for all experiments conducted in three beamtimes. The silver(111) crystal was cleaned by repeated cycles of argon ion sputtering and annealing at temperatures from 650 K to 750 K. The crystal quality was checked by LEED and x-ray photoelectron spectroscopy (XPS).

The organic material, used in the experiments, was purified by gradient sublimation [For 97]. The preparation of well ordered monolayers of PTCDA proceeded as follows: By evaporating of the material from a Knudsen cell, multilayers of PTCDA were grown. Subsequent the sample was heated up to 550 K for several minutes. Thereby only the monolayer remained on the substrate, while the multilayers were desorbed.

The vertical positions, obtained in an NIXSW experiment, are given in units of the substrate lattice. Therefore, the exact value of the lattice distance is essential. For the silver (111) lattice planes, this value is 2.3592 Å at room temperature [EckKan 71]. It was used in the evaluation of the data measured at room temperature. The nominal Bragg energy for this lattice distance is 2627.7 eV (at a Bragg angle of 90°). At low temperatures, a thermal contraction of the lattice constant can be seen from the energy shift of 10 eV in the Bragg energy. From the thermal expansion coefficient $\alpha = 18.9 \times 10^{-6}\,\mathrm{K}^{-1}$ [AshMer 76] of silver one calculates for the thermal expansion of a (111) lattice plane from 100 K to 300 K a value of 0.0089 Å[1]. From this contraction, the nominal Bragg energy for the silver (111) lattice planes at 100 K is calculated at 2637.6 eV. At temperatures around 100 K, the measured value indeed is shifted by 10 eV with respect to the room temperature value.

In a standing wave experiment the photon energy is varied in the vicinity of the Bragg energy. In contrast, the so-called "off-Bragg" survey spectra were taken with a photon energy far off the Bragg energy of the silver substrate (ca. 10 eV below or above the nominal Bragg energy). Hence, no standing wave effects due to the vertical adsorbate position and distribution contribute to an off-Bragg spectrum. Therefore an off-Bragg spectrum represents the intrinsic PE spectrum. This is particularly relevant with regard to the chemical shifts in a spectrum. If the chemical shifted atoms occupy distinct vertical positions with respect to the crystal surface, the shape of an "on-Bragg" spectrum can differ significantly from the shape of the intrinsic PE spectrum, obtained at off-Bragg photon energies.

For the determination of the coherent position and coherent fraction a

---

[1] The thermal expansion coefficent is defined by $\alpha = \frac{1}{l}\frac{\Delta x}{\Delta T}$.

series of NIXSW experiments were conducted. The result for a particular atom species, given below, correspond to the arithmetic mean of the results for the different data sets of this atom species. The given error corresponds to the standard deviation $\sigma = \sqrt{\frac{\sum_n x^2 - (\sum x)^2}{n(n-1)}}$ of the arithmetic mean. If no error is given, only one data set was used.

4.1.1 Monochromator instabilities

During beamtime J'03 the monochromator movement was not reliable. The steps in photon energy were apparently not equally spaced. This can be already seen from the reflectivity curves (see figure 4.1), whose shapes vary for the different data sets. Also, the fit of the theoretical reflectivity does not match very well to some of the data. The irregular steps in energy due to monochromator instabilities can lead to modified results of the experiment. Hence, only those data sets were used, for which the reflectivity curves fit sufficiently well to the theoretical curve. This ensures that only data with regular steps in photon energy were considered in the evaluation and no errors due to monochromator instabilities change the results. In beamtime N'03 and N'04 the monochromator ran much more stable, the measured reflectivity curves fit well to the theory (e.g. , see figures 4.15 and 4.21).

4.2 Silver substrate results

An excellent quality of the silver crystal is essential for the standing wave experiment. Before carrying out the NIXSW experiments, the quality of the crystal surface was checked by LEED. A characteristic LEED pattern of the Ag(111) surface, showing sharp LEED spots (figure 4.2), was recorded, revealing a good quality of the Ag(111) surface. However, LEED only is a surface sensitive and not a bulk sensitive method.

A good estimation of the bulk crystal quality can be given from an NIXSW experiment which is a bulk sensitive method. The first indication for a good bulk crystal quality is a sharp reflectivity curve (Darwin-Prins curve), which exhibits the typical shark fin shape, as can be seen in figure 4.3. In addition,

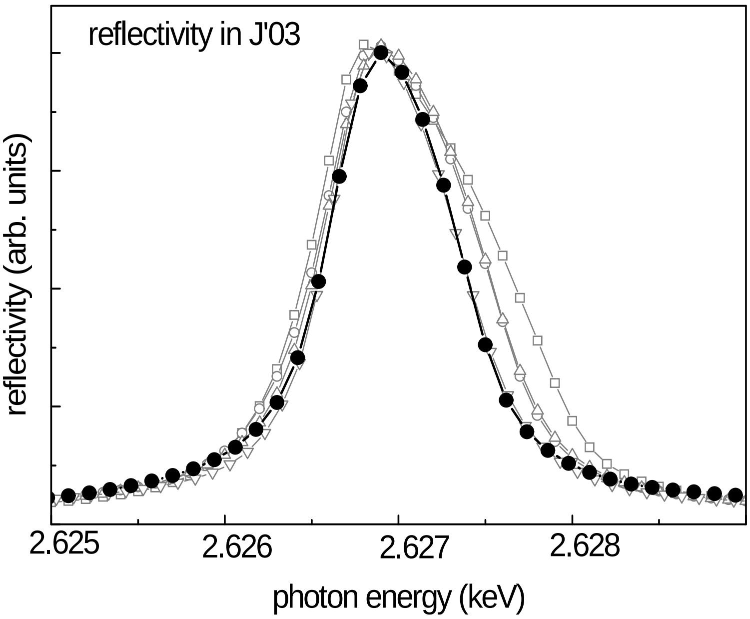

Figure 4.1: *Measured reflectivity curves in beamtime J'03. A big spread can be seen in the curves that should be identical. The spread is due to monochromator instabilities. In the evaluation, only data corresponding to reflectivity curves with the shape of the black curve were considered. All other reflectivity data and corresponding standing wave data were not used due to irregular steps in the photon energies.*

the resulting values for the coherent fraction and the coherent position should be close to the ideal value of $C_F = C_P = 1$.

In this work, the NIXSW investigation of the silver crystal was done with the Ag MVV Auger signal. The off-Bragg Auger spectrum is shown in figure 4.3. A typical NIXSW profile of the Ag MVV Auger signal and the corresponding reflectivity curve are presented in figure 4.3. The value of the coherent position, obtained by the fit, is close to the theoretical value. Due to the mosaicity of the crystal and presumably surface reconstruction, the coherent fraction lies approximately 14% below the expected value. The results of numerous NIXSW scans taken in the three beamtimes are given in table 4.1. However, these results reveal a good quality of the silver crystal.

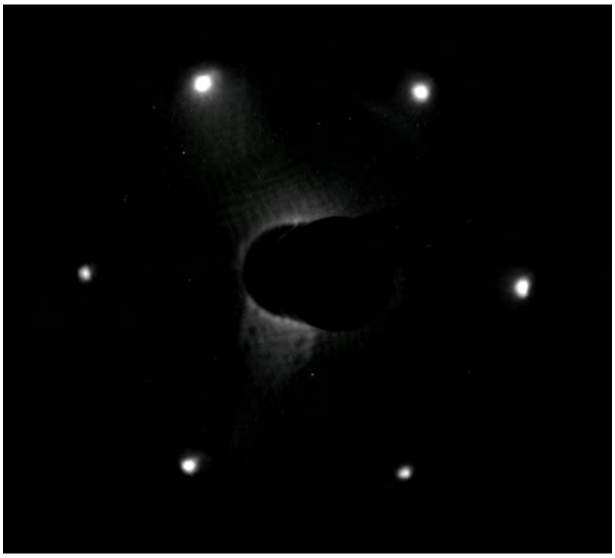

Figure 4.2: *LEED pattern recorded on the Ag(111) sample, used in the experiments of this work.*

The Auger signal is more surface sensitive than the PE signal which is bulk sensitive, therefore, the resulting coherent fraction of the NIXSW experiment can reveal surface reconstruction of the topmost layers of the substrate. However, effects, due to relaxation (contraction or expansion) of the outermost layer spacings are small. For Ag(111) Soares et al. found a bulk-terminated surface, with no contraction or expansion of the outermost layer spacings [Soa 99]. The reconstruction of the surface underneath the organic film, however, is not clear, yet. Schmitt describes the reconstruction of the surface after annealing the PTCDA covered Ag surface in his thesis [Sch 06]. A stepped Ag(775) surface transforms to (111) terraces with double atomic step edges, populated with PTCDA molecules.

Exemplarily, the underlying bulk signal of an Ag MVV scan was evaluated [Bau 07], the found values for the coherent fraction are slightly higher (approximately 2%) than for the Auger values. The values for the coherent position are closer to 1 This is a hint of the reconstruction of the topmost layers of the silver crystal.

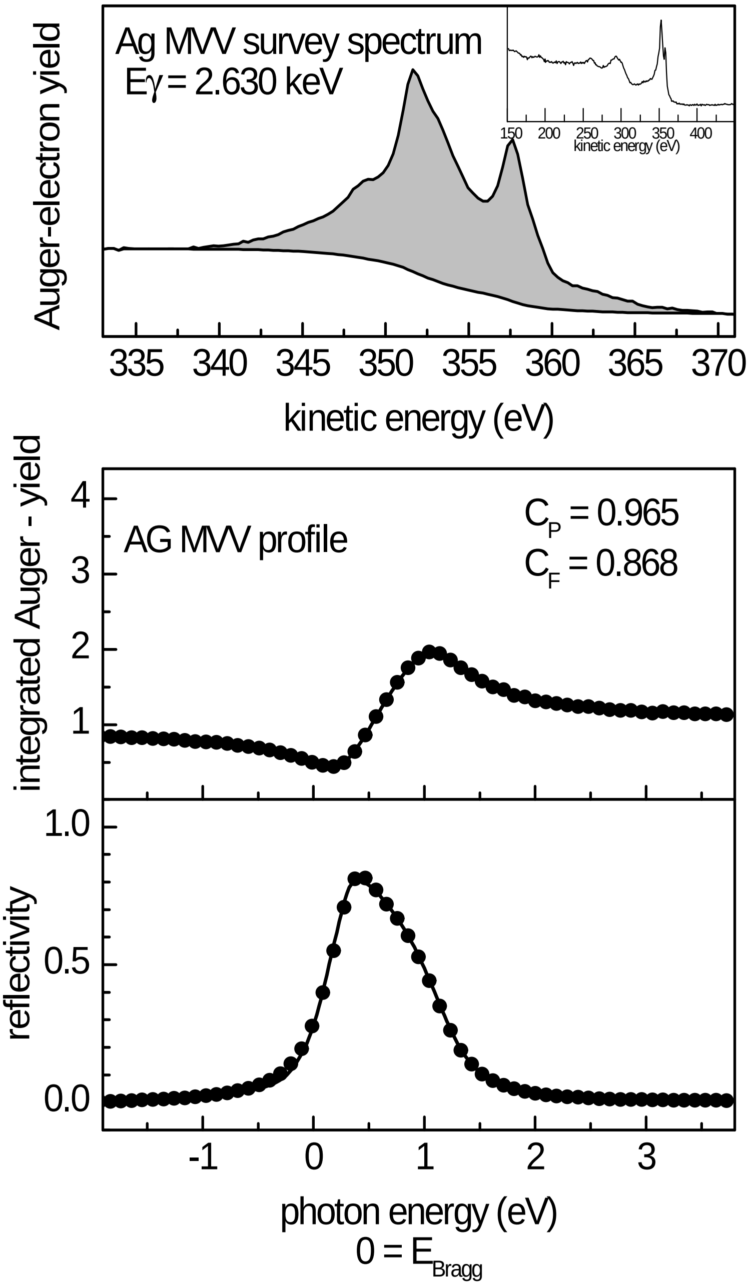

Figure 4.3: *Top: Auger spectrum of Ag MVV taken with a pass energy of the electron analyzer of* 46 eV*. For analyzing the peak area, a Shirley background (see appendix E.1) was adapted to the Auger signal. In the inset, an off-Bragg PE spectrum over a larger energy range is shown. Center: Typical Ag MVV NIXSW profile. The points represent the data and the solid lines the corresponding fit. The data were taken in beamtime N'03 with a pass energy of* 58 eV*. The corresponding results for the coherent position and fraction are given in the figure. Bottom: Corresponding reflectivity curve, it has the typical shark-fin shape which corresponds to a good crystal quality.*

Ag MVV results

(111) diffraction / RT

beamtime	number of spectra	C$_P$	C$_F$
J'03	2	0.992 ± 0.003	0.893 ± 0.011
N'03	3	0.991 ± 0.007	0.876 ± 0.067
N'04	4	0.985 ± 0.004	0.855 ± 0.011

($\bar{1}$11) diffraction / RT

beamtime	number of spectra	C$_P$	C$_F$
J'03	1	1.000	0.964
N'03	2	1.000 ± 0.000	0.877 ± 0.055

(111) diffraction / LT

beamtime	number of spectra	C$_P$	C$_F$
N'03	1	0.965	0.868
N'04	12	0.972 ± 0.007	0.902 ± 0.029

Table 4.1: *Results of the NIXSW fits for the silver substrate based on the Auger MVV transition. The results are listed for the different beam times, for different sample temperature (room temperature and low temperature), and for the distinct diffraction planes. However, all resulting coherent positions and fractions are in the same range and reveal a high quality crystal. The errors correspond to the standard deviation of the results.*

4.3 ($\bar{1}$11) results for carbon and oxygen

In order to determine the exact lateral position of the PTCDA molecules on the Ag(111) surface, ($\bar{1}$11)-NIXSW scans were taken on the monolayer films. Such a determination of the lateral position was done by Kilian for the molecule end-capped quaterthiophene (EC4T) on Ag(111) via triangulation [Kil 02b].

Several ($\bar{1}$11)-NIXSW scans on the C1s and O1s transition were recorded in this work. The evaluation yielded values for the coherent fraction below $C_F \leq 0.2$ for both atom types. In that state of the evaluation, the used quadrupole parameters was with $Q = 0.20$ quite too low. With the better value for the quadrupole parameter of $Q = 0.31$, exemplary NIXSW scans were evaluated again. These scans revealed an even lower value of the coherent fraction.

Therefore, a further evaluation of these NIXSW scans was not done in this work, since a triangulation as it was done for EC4T, is not possible due to the low values of C_F, which already are in the range for incoherent films. The reason for these low values can be found in the high number of atoms for each species in the monolayer.

4.4 Carbon results

The PTCDA molecule has seven chemically different carbon positions. This is due to geometrical reasons (figure 4.4) but only valid for the gas phase. The unit cell of the monolayer of PTCDA/Ag(111) includes two molecules on distinct positions on the silver substrate. The chemical environment is also different for the carbon atoms on the distinct positions on the substrate [Kra 06].

A typical off-Bragg PE spectrum for the C1s transition is shown in figure 4.5. The value for the off-Bragg photon energy for this spectrum was $E\gamma = 2.617\,\text{keV}$ (the nominal Bragg energy has a value of $E\gamma = 2.6277\,\text{keV}$).

The distinct contributions, due to chemical shift and to satellites, are not resolved in the spectrum, because of the relatively low pass energy of the electron analyzer (47 eV). Zou et al. presented high resolution photoelectron

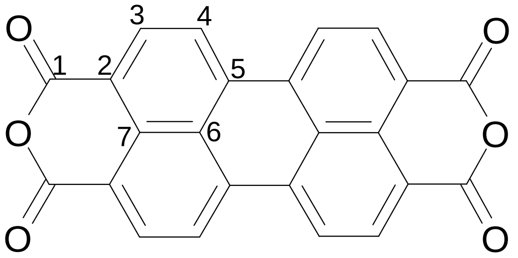

Figure 4.4: *PTCDA molecule. Due to geometrical reasons the molecule has 7 chemically different positions.*

spectroscopy results of 0.9 monolayer of PTCDA on Ag(111) [Zou 06]. In their spectra the main C1s peak clearly consists of two peak features. The smooth flank at binding energies from 290 eV to 286 eV in figure 4.5 (top) exhibits at least three distinguishable peak features in their spectrum. In the C1s spectra taken in the present work, all these features are not resolved due to the used analyzer resolution.

Schöll analyzed the contributions of the different carbon atom types to the total photoemission spectrum. He attributed the main peak feature to the ring carbons, whereas the carbons of the anhydride group (denominated carbon 1 in figure 4.4) contribute only at higher binding energies to the spectrum. If these carbon atoms occupy different vertical positions on the substrate surface, this should be seen in the PE spectra of a standing wave experiment. In this case the shape of the C1s spectrum would change for various photon energies (close to the Bragg energy). Indeed, the principal component analysis (PCA)[2] proposes two components for the carbon. The fit of these two principal components to the PE spectra of the standing wave removes the noise from the data (target factor analysis (TFA)). This result shows that there is a difference in the C1s-peak shape within the standing wave. However, the difference is only subtle (and therefore, not shown here), and the NIXSW profiles obtained from differential fitting of the spectra were not reliable. Eventually NIXSW scans with a high resolution pass energy of the electron analyzer and long acquisition times could make a differential analysis possible.

---

[2] A short introduction to PCA and TFA is given in appendix G.

For the C1s spectra, only subtraction of a Shirley background (see Appendix E.1) was practicable. No region could be defined for adapting a linear background. Therefore, in all C1s PE spectra of the standing wave experiment, a Shirley background has been subtracted.

In the resulting NIXSW profile, each point corresponds to the remaining area of the background subtracted PE spectrum. Figure 4.5 shows the NIXSW profile and the corresponding reflectivity curve for the C1s transition. In table 4.2 (on page 60) the results for carbon are listed for the different preparations and pass energies.

In beamtime J'03 seven C1s scans were taken on one preparation. In table 4.2 the average value over these scans was taken. However, regarding each scan after the other, a tiny declining trend for the values of the coherent position and fraction can be observed (After 24 hours, a decline of 4.7% was found for the value of the coherent position and a decline of 18% for the value of the coherent fraction. Considering the distance of the carbon atoms to to the Ag surface, the decline of the coherent position only corresponds to less than 1%). The decline is shown in figure 4.6.

These variations within values obtained from the film of preparation A in beamtime J'03 can have different reasons. They can have a statistical origin. Another possibility is a beam induced rearrangement of the molecules. Such an effect also can be a time depending effect. However, this effect is very small, therefore, as resulting value the average of these values can be taken without restriction.

In beamtime N'04 three NIXSW scans were taken on the C1s transition again (on preparation C, D and E). However the differences in the results are striking compared to the results obtained from preparation A and B, as can be seen in table 4.2.

The results obtained from preparation E are not reliable. This NIXSW scan was acquired after half a monolayer of the precursor and an additional large amount of co-adsorbed water was annealed at 600 K for 3 minutes. It is not clear, whether the molecules are still intact after such a procedure. Hence, this values will not be further discussed.

Much more interesting are the results for preparation C and D. The first

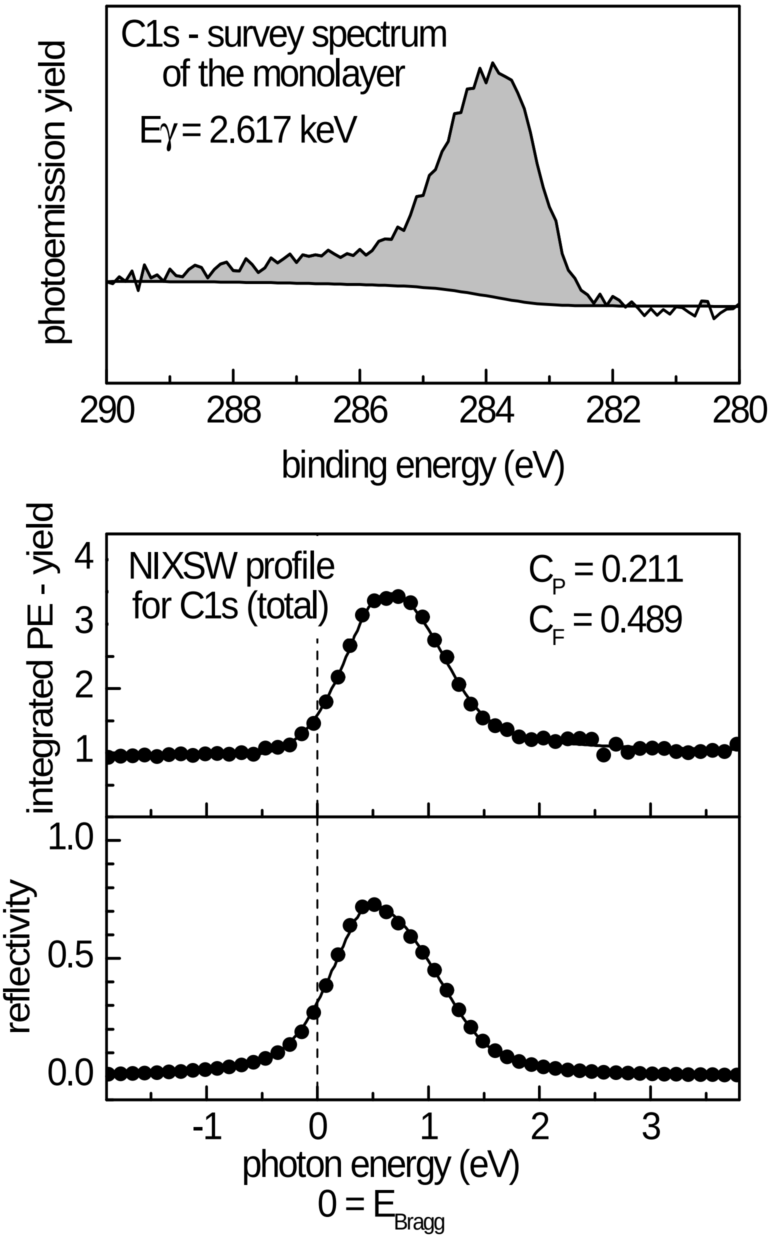

Figure 4.5: *Top: survey spectrum of the C1s-transition for the monolayer. The pass energy of the analyzer was* 47 eV*. This spectrum was taken in beamtime N'04. (p114, p122, p126). For analyzing the peak area, a Shirley background was adapted to the spectrum. Center: C1s NIXSW profile and reflectivity (bottom) for the monolayer phase. The points represent the data and the solid lines the corresponding fitting result. The corresponding results for the coherent position and fraction are given in the figure. The data were taken in beamtime N'03 with a pass energy off* 47 eV *(Pt1_111).*

result corresponds to half a monolayer at room temperature, which was annealed. The LEED spots of this film were not very intense (figure 4.7, left).

Surprisingly, the value of the coherent position lies $\Delta C_P = -0.05$ below the average value obtained from preparation A and B. This corresponds to $\Delta C_P = 0.1\,\text{Å}$. By depositing additional PTCDA molecules on this film and the subsequent annealing, the spots in LEED pattern became more intense (figure 4.7, right).

The results of this subsequent NIXSW scan reveal that the values for the coherent fraction and coherent position obtained from preparation D are closer to the values of preparation A and B. The reason for this is given in the following.

It is known that the PTCDA molecules first occupy the steps of the Ag(111) surface, before they start to order in the typical herringbone structure on the terraces [Glö 98] [Sch 06]. Therefore, at the coverage of half a monolayer, all steps were decorated with molecules and the growth of the herringbone structure did already begun. The existence of the herringbone structure can be concluded from the LEED pattern, recorded on the 0.5 monolayer film. Unfortunately, the ratio of molecules decorating the steps to molecules lying flat in the herringbone structure is not known.

After the additional deposition of organic material, a coverage of the full monolayer is reached. In this situation all (111) terraces are covered by flat lying molecules arranged in the herringbone structure. Nevertheless, in the results of the full monolayer approximately the same contribution of the steps decorated with molecules is included. With the knowledge of the two coverages, the values for the coherent fraction and coherent position of the pure herringbone structure, without the contribution of the molecules on steps, can be calculated. In vector notation of the Argand representation the vector for the pure herringbone structure is given by

$$\overrightarrow{C1s}^{\text{corr.}} = 50\% \cdot \overrightarrow{C1s}^{1\text{ ML}} - \overrightarrow{C1s}^{0.5\text{ ML}}.$$

Thereby, *1 ML* corresponds to a full monolayer and *0.5 ML* to half a monolayer. This is graphically shown in figure 4.8. The corrected values are given in table 4.2. The corrected value of the coherent position is in excellent agreement with the averaged values of preparation A and B. From this result, it can be concluded that in preparation A and B the quality of the crystal surface was superior, and only suboptimal in the preparations C and D. Hence, the results for preparation A and B can be considered as the final results for the carbon in the monolayer PTCDA on Ag(111) ordered in the herringbone structure.

C1s results with a pass energy of 47 eV

prep.	spectra	ML	$C_{P\text{ eff}}$	$C_{P\text{ eff}}$(Å)	C_F
A J'03	7	1	0.214 ± 0.004	2.863 ± 0.010	0.547 ± 0.043
B N'03	1	1	0.211 ± 0.020	2.857 ± 0.047	0.489 ± 0.080
average	8		$\mathbf{0.214 \pm 0.004}$	$\mathbf{2.863 \pm 0.010}$	$\mathbf{0.540 \pm 0.045}$

C1s results with a pass energy of 58 eV

prep.	spectra	ML	$C_{P\text{ eff}}$	$C_{P\text{ eff}}$(Å)	C_F
C N'04	1	0.5	0.168 ± 0.020	2.756 ± 0.047	0.256 ± 0.080
D N'04	1	1	0.200 ± 0.020	2.831 ± 0.047	0.418 ± 0.080
E N'04	1	0.5	0.280 ± 0.020	3.020 ± 0.047	0.245 ± 0.080
D corrected	1	1	*0.213*	*2.862*	*0.587*

Table 4.2: *Fitting results from the NIXSW profiles. The first column corresponds to the preparation and beamtime. The column "spectra" denotes the number of evaluated spectra. The errors correspond to the standard deviation of the results from the evaluated profiles. The errors for the result of beamtime N'03 and N'04 were estimated by a confidence analysis of Gerlach et al. [Ger 07]. The results obtained in beamtime N'04 has to be considered with special attention, because for each preparation only one XSW scan was measured. Preparation C corresponds to half a monolayer film which was annealed for 3 minutes at 550 K. More PTCDA was deposited (approximately 2ML) onto this film and subsequently annealed to obtain preparation D. The preparation E corresponds to half a monolayer of the precursor phase which was annealed at 600 K. The coherent parameters differ significantly from those obtained in previous preparations and are not reliable. For the explanation of the corrected values for preparation D see text.*

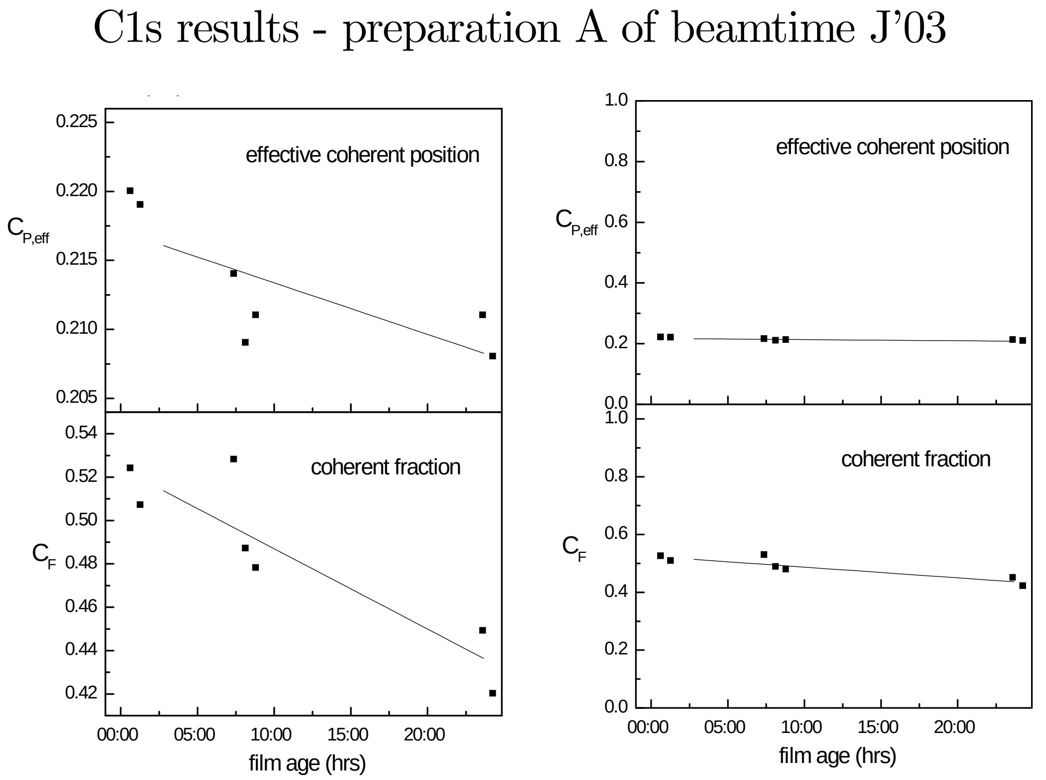

a) b)

Figure 4.6: *Results for the XSW scans of C1s. All data (solid symbols) correspond to the same preparation, the structural parameter are plotted versus the age of the monolayer film. The lines correspond to a linear regression of the presented data. It has to be noticed that the y axes are greatly exaggerated in figure a). In figure b) the y axes go over the whole possible range for the coherent fraction and position. However, a trend to lower coherent positions and fractions with time (or beam exposure) can be seen.*

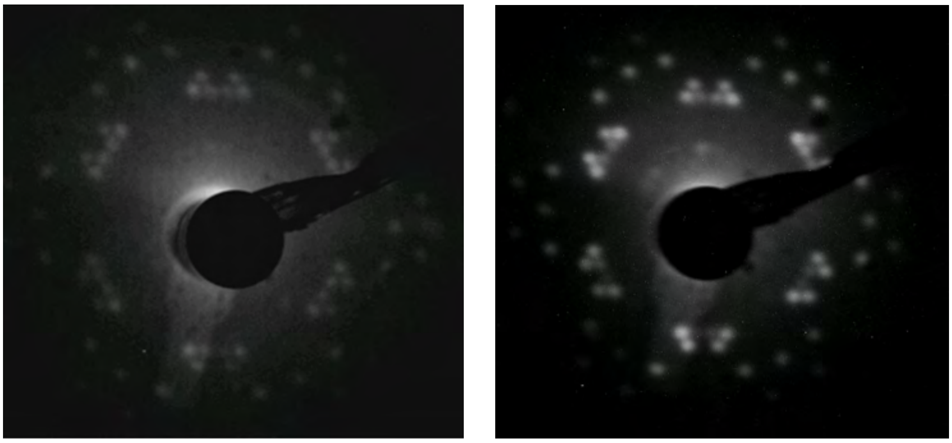

Preparation C; 0.5 monolayer Preparation D; 1 monolayer

Figure 4.7: *LEED patterns of the PTCDA films of preparation C and D in beamtime N'04. The electron energy was approximately 20 eV.*

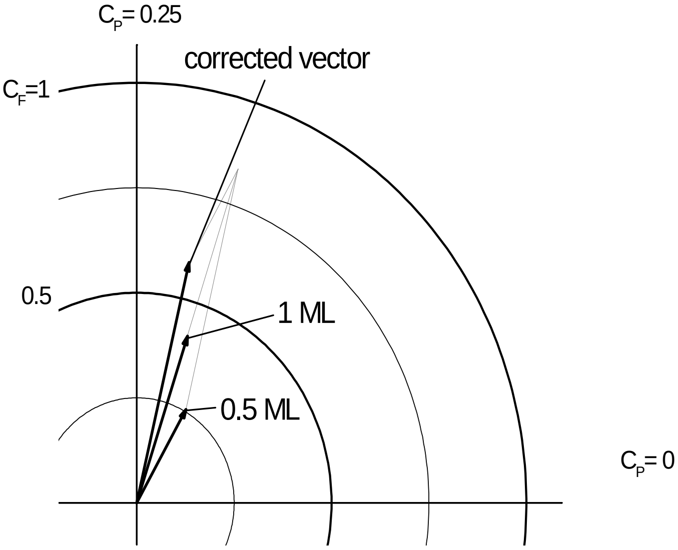

Figure 4.8: *Argand diagram showing the C1s vectors for 0.5 monolayer (prep. C), and for 1 monolayer (prep. D). The intrinsic C1s vector, describing the herringbone structure, can be obtained by vector subtraction. For further details see text.*

4.5 Oxygen results

In this chapter the results for the oxygen are presented. The chapter starts with the NIXSW investigation of the O KLL Auger transition.

For the O1s transition, the results differ for the different preparations. In order to discuss the reasons for this, the experimental conditions for the different preparations are described in the next section.

The NIXSW results of the total oxygen are presented in the following section. "Total oxygen" stands for the signals that were averaged over all oxygen atoms in the monolayer.

In order to describe the structural changes which were observed for the oxygen, a correction model will be presented, subsequently.

The molecule PTCDA has two chemically different oxygen types: The 4 outer carboxylic oxygen atoms and the 2 inner anhydride oxygen atoms (see figure 4.4). It is possible that these chemically different atoms can occupy distinct vertical positions. In the last section, the data were analyzed for the two chemically different oxygen atoms.

4.5.1 Auger O KLL

In beamtime J'03 (preparation A), the Auger transition O KLL was investigated with NIXSW. The advantage of the Auger emission is that no quadrupole contributions add to the electron yield. Nevertheless, the results for the O KLL scans are not identical to the quadrupole corrected O1s results.

Stanzel et al. [Sta 04] explain this discrepancy with different excitation origins for the Auger process. They argue that a core hole can be excited by photons and also by electrons. Therefore, the O KLL-NIXSW signal consists of two contributions, one originating from the photon-excitation which carries the structural information from the oxygen atoms in the overlayer, the other originating from the excitation by escape-electrons from the bulk. The latter contribution is mainly caused by (inelastically scattered) photoelectrons from the Ag substrate which therefore exhibits the structural signature of Ag bulk-atoms in an NIXSW-scan. Therefore, the measured O KLL position vector is the weighted sum of a bulk position vector $\overrightarrow{Ag}$ and the 'real' oxygen position

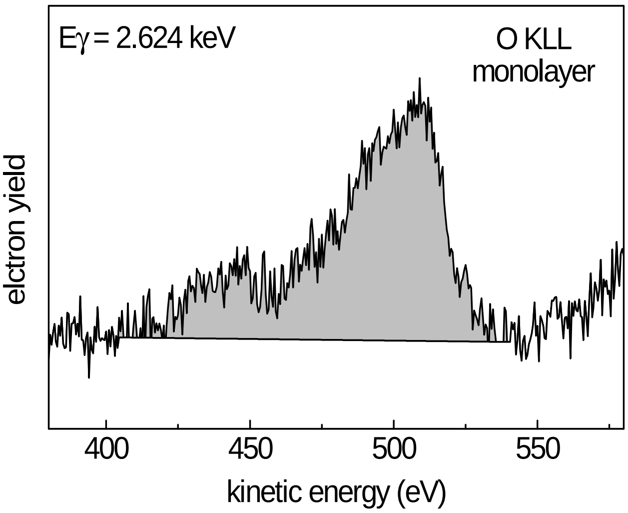

Figure 4.9: *Auger spectrum of O KLL. The pass energy of the electron analyzer was* 46 eV*. For analyzing the peak area, a linear background was adapted to the Auger signal.*

vector $\overrightarrow{OKLL}^{corr.}$:

$$\overrightarrow{OKLL} = (1-a)\cdot\overrightarrow{Ag} + a\cdot\overrightarrow{OKLL}^{corr.}.$$

The corrected values with $(1-a) = 25\%$ and 50% silver contribution, respectively are shown in table 4.3. Stanzel et al. used for the 1,4,5,8-naphthalenetetracarboxylic dianhydride (NTCDA) a 50% silver contribution. For the PTCDA the best agreement of the position vectors $\overrightarrow{OKLL}^{corr.}$ and $\overrightarrow{O1s}_{low\ res.}$ was also obtained for 50%.

A typical O KLL Auger spectrum is shown in figure 4.9. In order to obtain the integrated electron yield, a linear background was subtracted from the Auger spectra. The composition of the O KLL Auger spectrum is relatively complicated for the PTCDA. Nonetheless, it was tried to find a fitting model which divides the two chemically different oxygen, in order to evaluate the integrated electron yields of the distinct oxygen separately. However, OKLL results

	C_P	C_P(Å)	C_F
OKLL	0.091 ± 0.010	2.568 ± 0.023	0.631 ± 0.014
$OKLL_{corr.25\%\_Ag}$	0.191	2.805	0.612
$OKLL_{corr.50\%\_Ag}$	0.211	2.852	0.702

Table 4.3: *O KLL result for the monolayer. The values were corrected for 25% and 50% silver contribution. With the latter correction the same coherent position as for the low resolution O1s data is obtained. The errors correspond to the standard deviation of the results.*

the statistics of the standing wave spectra was too low and no model, yielding satisfactory results for the NIXSW profiles, could be found in this work. Therefore only the average oxygen position was evaluated with the O KLL scans.

In beamtime J‘03 the O KLL electron yield was taken during 9 NIXSW scans. The correction of the O KLL vector is also shown in the Argand diagram of figure 4.10.

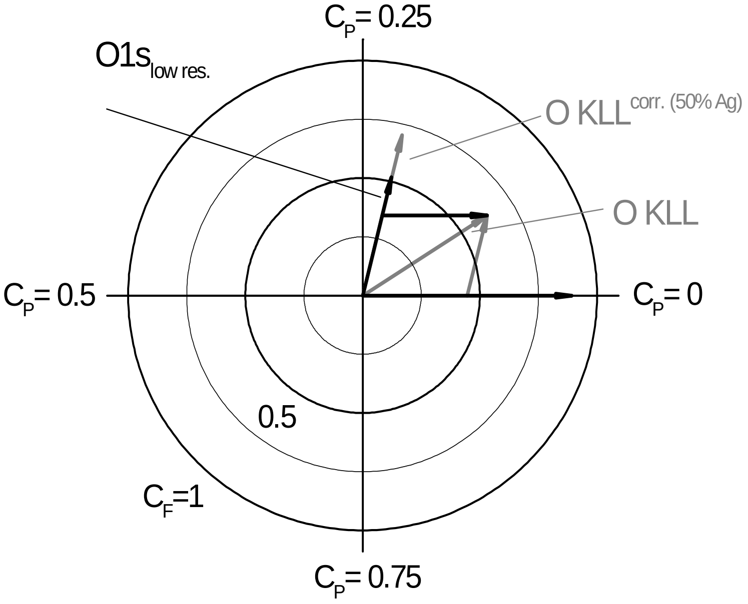

Figure 4.10: *Argand diagram for the total oxygen in the monolayer. The results, obtained from the O KLL NIXSW yield differ from those of the O1s NIXSW yield. By correcting the O KLL values for a silver contribution of 50%, the O1s-low resolution result is obtained (see text).*

4.5.2 Measuring conditions

Small differences in the O1s-PE spectra of nominally identical layers were observed during the experiments. These differences can have their origin in the experimental conditions and / or in the different monolayer preparations. Therefore, the film preparation and the experimental conditions are described in the following.

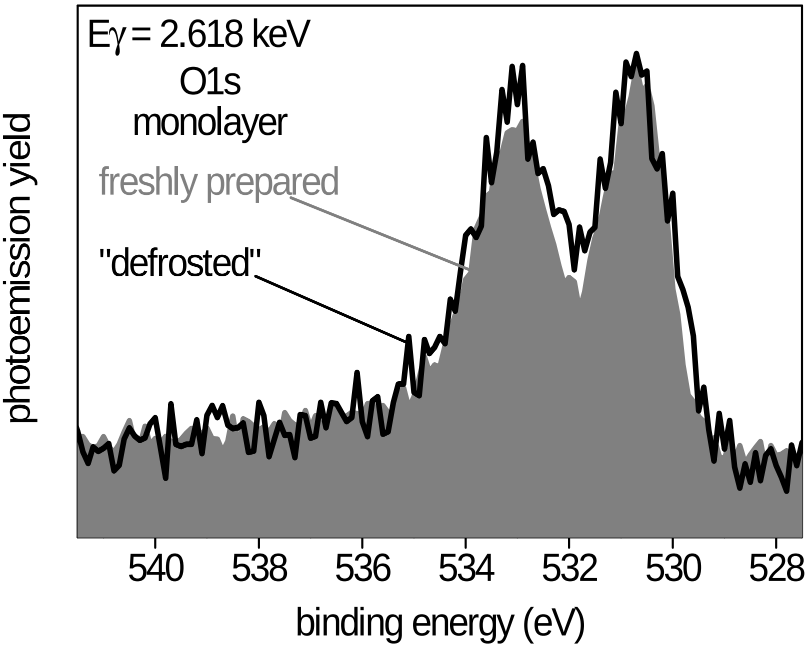

Figure 4.11: *Comparison of two off-Bragg PE spectra of the O1s-transition for the monolayer taken during beamtime N'03. In both spectra, two main peak features, due to the chemical shifted oxygen types of PTCDA, can be seen at the binding energies of* 530.6 eV *and of* 533.0 eV*. The spectrum taken on the defrosted monolayer (black curve - see text) differs slightly in the shape from the spectrum taken on the freshly prepared monolayer (grey). The peak at higher binding energy is slightly larger and the separation of the two peaks is less pronounced. The pass energy of the analyzer was* 23.5 eV *(Pt1_110, Pt1_164).*

The results can be divided into two groups. It occurs that one group with similar results was measured with a low resolution of the electron analyzer. Low resolution stands for a pass energy of the electron analyzer of 47 eV and more. It is not clear, if the difference between the results can be ascribed to the resolution of the analyzer. However, in the following the results of the first group will be nominated as *low-resolution* results. Those in the second group, measured with a pass energy of 23.5 eV of the electron analyzer will be referred to as *high resolution* results in the following.

Oxygen atoms are weak photoemitters. Even with the high-flux rate at the synchrotron in Grenoble (*ESRF*) the counting time needed for the data acquisition of the high resolution spectra was extremely long (up to 6 hours). Therefore only few high resolution NIXSW scans of the O1s transition were taken, due to the limit of time.

The low resolution scans were taken during three beamtimes. In the first two beamtimes J'03 and N'03, the low resolution data for O1s were collected shortly after the preparation of the monolayer (preparation A and B) and hence are considered as being reliable. During beamtime N'04 three different results from three different preparations were obtained. As will be discussed in the caption of table 4.4 (on page 79) in more detail, none of the O1s results from beamtime N'04 will be taken into account for the further discussion.

The high resolution O1s NIXSW spectra were taken during three periods. In J'03, six spectra were taken, but due to monochromator and beam instabilities, only three spectra could be analyzed. The spectra were taken approximately 24 hours after preparation of the monolayer. The sample was kept at room temperature after preparation (preparation A).

In N'03, one high resolution NIXSW scan was taken six hours after the monolayer deposition (preparation B). The sample was kept at room temperature, the scan took six hours. During this time, the photon current lost more than half of its initial intensity. This scan could not be evaluated so far, because of problems in background subtraction in the reflectivity curve. However, because of the very good statistic of this scan, it can be clearly seen, how the peak ratio of the two main peaks in the O1s PE spectrum (see figure 4.11) changes in the standing wave experiment This gives a strong evidence for the distinct vertical positions of the two oxygen species.

The third series of high resolution measurements was performed after measuring the precursor phase in beamtime N'03 (preparation F). The sample with the PTCDA precursor film was cooled for 24 hours at 100 K. Then, the sample was heated up to 550 K, and, in order to increase the coverage, PTCDA was evaporated on the sample again and the sample was heated to 550 K again to desorb the multilayers. LEED measurements revealed the monolayer structure of PTCDA on Ag(111). Two off-Bragg spectra, one before and one after the precursor preparation, are shown in figure 4.11. It can be seen how the high resolution spectra of the second period differ from the ones measured before. The difference is only subtle, however, the dip between the two peaks is less deep for the spectra, taken after the precursor preparation. This feature can also be found in the on-Bragg spectra.

This change in the peak shape could have different reasons. It could be due to an intensity loss of the two peaks or due to the appearance of an additional peak between them.

An additional peak might originate from H_2O. The binding energy for the oxygen of water on Ag(111) was recorded by Carley et al. [Car 90] at 534 eV. The here observed peak is at a binding energy of 531.8 eV (calibrated after Schöll et al. as noted in [Zou 06]). Hence, there is a big difference in the binding energies, but nevertheless Schöll found at this position (2 eV below the value from Carley et al.) an increasing peak with time in low temperature experiments, which he attributed to co-adsorbed water [Sch 05a]. Carley found that water on Ag(111) desorbs at 160 K. The present experiment was done at room temperature. Why should there be any water remaining on the sample? Possibly, the water desorption is influenced by the PTCDA molecules. This could explain also the shift in binding energy of this peak.

Another explanation of this feature could be the intensity loss induced by beam damage of the PTCDA. This was recorded by Schöll for multilayers of PTCDA on Ag(111) for very high beam flux [Sch 03]. However, for monolayers under high flux from the undulator in the synchrotron experiment, no radiation damage was found by Schöll et al. as noted in [Zou 06].

In the present work, a change in the spectra of the monolayer during a time scale of six hours also could not be observed.

In order to fit the PE spectra of the monolayer with the same model, an additional peak was introduced. Otherwise the fitting was not possible with the fitting model deduced on the off-Bragg survey spectrum. The binding energy of this additional peak lies at 532.07 eV and it has a FWHM of 3.5 eV. The fitting model which includes this peak feature is shown in figure 4.12. In section 4.5.5 the fitting models will be discussed in more detail.

Intrinsic O1s photoemission spectrum

In order to be sure that the x-ray beam does not induce any changes to molecular film (and consequential changes to the photoemission spectra), the off-Bragg spectra of this work were compared with high resolution O1s spectra measured by Schöll [Zou 06]. These spectra were taken on freshly prepared PTCDA monolayer films on Ag(111) with a photon energy of 700 eV.

In order to compare the high resolution spectra of this work with the spectra of Schöll, the identical background subtraction had to be done for both spectra (for details see chapter 5.3.1). Figure 4.13 shows the background subtracted spectrum of this work compared with a spectrum of Schöll. It can be seen that the spectra are very similar, however, the peak features are broader in the spectrum of this work. The fitting procedure of the spectra revealed that the peaks in the spectra of Schöll correspond to several Voigt peaks. However, the best fitting model for the spectra taken in this work was obtained with pure Gaussian functions. The Lorentzian contribution, due to life time broadening of the core states, could not be found in the data of this work, because of the finite resolution of the electron analyzer in the experiment.

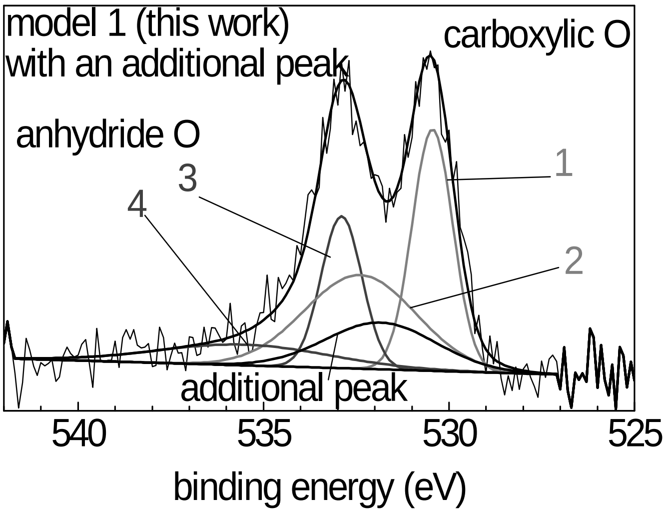

Figure 4.12: *Off-Bragg O1s PE spectrum of the monolayer where the additional oxygen peak is included in the fitting model. The stoichiometry of the PTCDA O atoms was constrained in the fit. The amount of the additional peak to the total spectrum is* 14.7%*. For more details of the fitting models see section 4.5.5.*

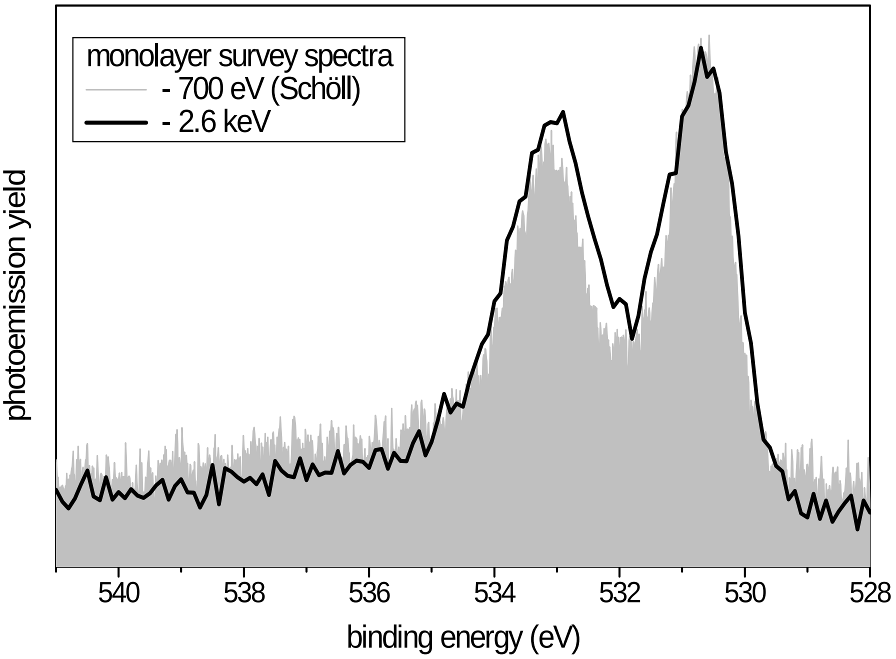

Figure 4.13: *Comparison of the O1s photoemission spectra of the PTCDA monolayer taken in this work (black) and by Schöll (grey) [Sch 05a]. In both spectra the background was subtracted in the way Schöll proposed (see text). The peaks of the spectrum of this work are broadened in comparison to the peaks of the spectra taken by Schöll et al.*

4.5.3 Total Oxygen

In this section the total oxygen results are given, both, as well as for the low resolution as for the high resolution spectra.

For analyzing the O1s part of the PE spectra, the large background which is due to inelastically scattered electrons from the silver substrate has to be separated from the oxygen signal. Two different types of backgrounds were fitted to the spectra, a Shirley background and a linear background. It was found that for the O1s spectra the result of the NIXSW fit is the same, regardless of which background was subtracted. Consequently, for all following O1s spectra, a linear background was subtracted. The fit of the linear background to a typical O1s off-Bragg spectrum is shown in figure 4.14.

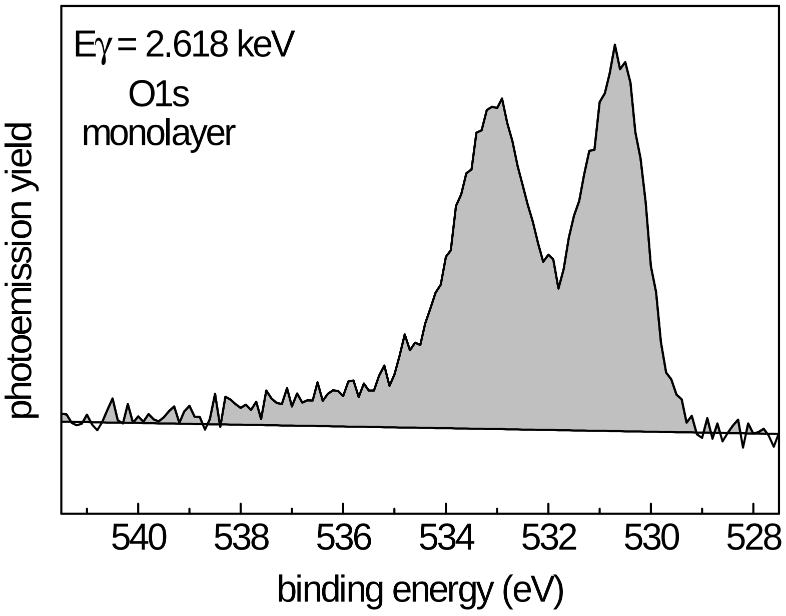

Figure 4.14: *Off-Bragg Photoemission spectrum of the O1s transition for the monolayer. The pass energy of the analyzer was* 23.5 eV*. For analyzing the peak area, a linear background was fitted to the PE spectrum (N'03; Pt1_110).*

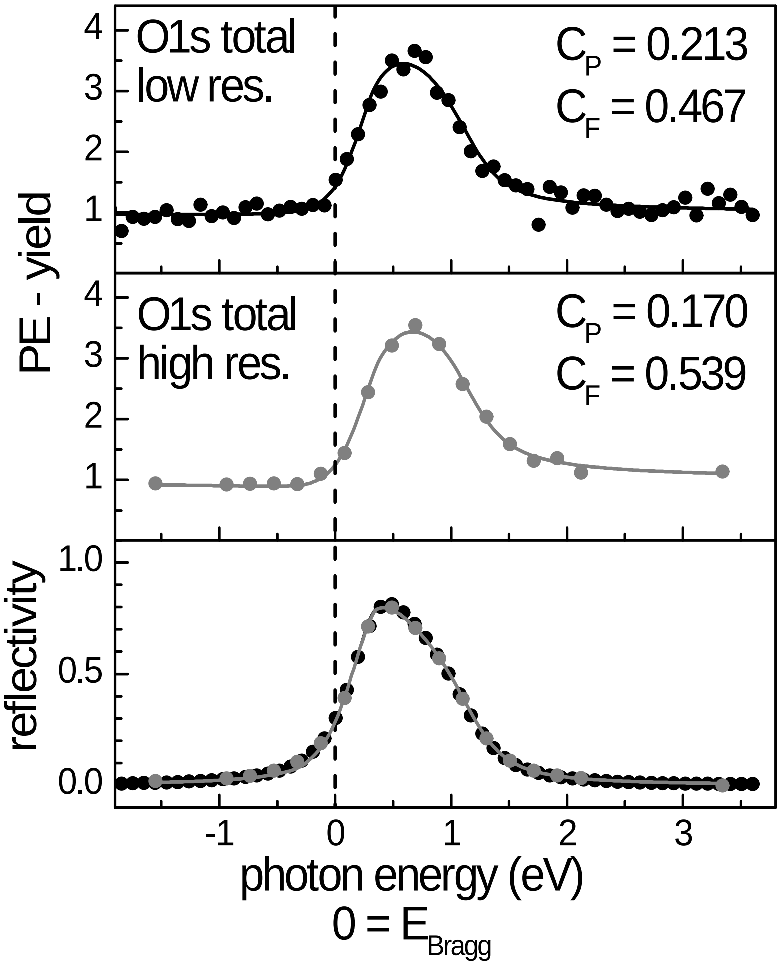

Figure 4.15: *O1s NIXSW profile and reflectivity for the monolayer phase. The data were taken in beamtime N'03 with a pass energy of* 47 eV *(black - Pt1_111) and* 23 eV *(grey - Pt1_165 and Pt1_167). The points represent the data and the solid lines the corresponding fitting result. The corresponding values for the coherent position and coherent fraction are given.*

Figure 4.15 shows the NIXSW-profile and the corresponding reflectivity curve for the O1s transition. As noted before, the photoelectron counting rate depends on the pass energy of the electron analyzer. In order to get a similar statistics in the so-called *high resolution scans* with the pass energy of 23.5 eV, as obtained for the so-called *low resolution NIXSW scans* with a pass energy of 46.5 eV and higher, the acquisition time was raised. A typical acquisition time for an O1s low resolution scan is between 20 minutes and one hour. The high resolution scans take much longer: for one high resolution scan with only 16 measuring points in beamtime N'03, six hours were needed. Already a small shift in any experimental parameter during data acquisition can make the data useless. For the acquisition of the high resolution data, the experiment is close to its limits due to the monochromator stability. Therefore, the data acquisition was performed in two steps for the high resolution scans (see section 4.5.5).

The NIXSW results for the total oxygen are shown in table 4.4 (on page 79).

4.5.4 Correction of the oxygen result

As can be seen in table 4.4 and in the Argand diagram of figure 4.16, a difference in the results for the O1s data depending on the preparation is found. A possible reason for this could be found in the decoration of the step edges on the Ag(111) surface with PTCDA molecules.

As discussed above for the carbon results, it can be assumed that the results for O1s obtained on the freshly prepared films (preparation A and B) correspond to the structural parameters of the herringbone structure. These results are different compared to the results obtained from preparation A and F, which were taken with a high resolution pass energy. With time (or beam influence) structural changes occurred in the film of preparation A. As discussed in section 4.5.2 the film of preparation F also exhibits structural differences due to the conditions of preparation. Therefore, it is clear that the high resolution results have to be corrected, in order to obtain the results for the herringbone structure.

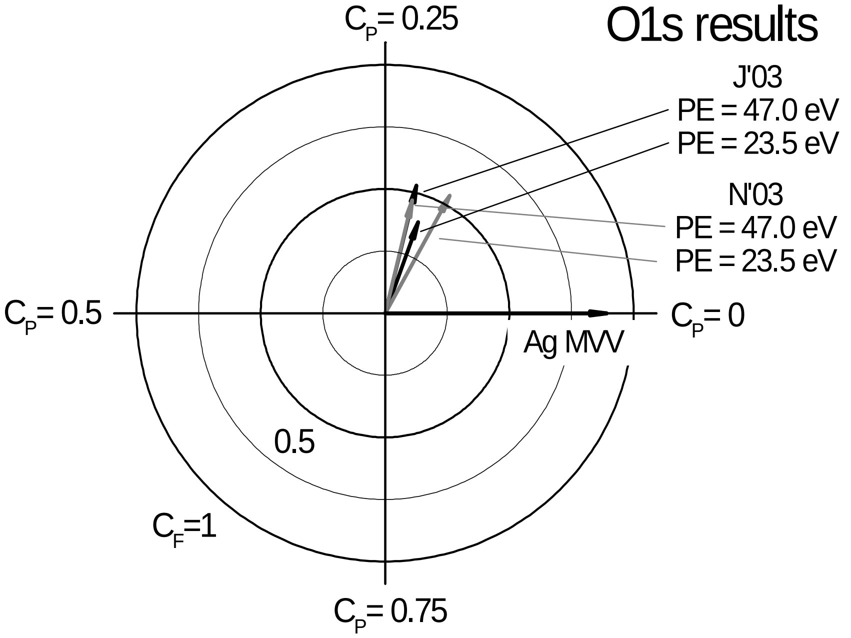

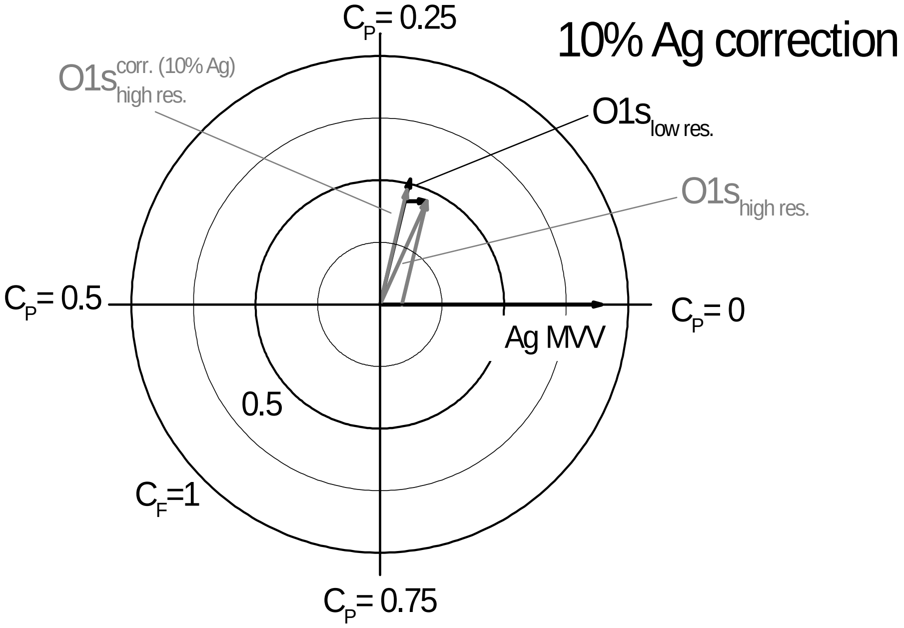

Figure 4.16: *Top: Argand diagram showing the resulting vectors for the silver substrate, and for the total oxygen (obtained from different preparations). Bottom: Using a correction of the structural changed (high resolution) vectors with a bulk-like contribution of 10 %, the results of freshly prepared films (low resolution) are approximately obtained (average values of J'03 and N'03). It has to be noted that individual corrections of the two high resolution vectors, reveal bulk-like contributions of* 7% *and* 17%, *for J'03 and N'03, respectively.*

For the discussion of a correction it is more convenient to consider the Argand vectors (figure 4.16). In the easiest case it can be assumed that the same correction vector is needed for both preparations, only contributing with different percentages to the high resolution vectors. However, these percentages are not known.

The lengths of the high resolution vectors are quite different for the two preparations ($\mathrm{C}_F = 0.41$ for preparation A, and $\mathrm{C}_F = 0.53$ for preparation F). As shown in the confidence analysis of Gerlach et al. [Ger 07], the value for the coherent position has only small error bars, whereas the coherent fraction has much larger error bars. This point complicates the situation, since it is not clear what the exact value for the coherent fraction is.

It must be concluded that the determination of the correction vector is not possible from the available information. Too many parameters are undefined or have an unconfident value. For the determination of a correction vector at least the knowledge of the percentage contribution to the high resolution vector would be required.

However, in the following a correction model is presented, which could explain the observed differences in the results. This model is based on the STM investigation of Glöckler et al. [Glö 98]. The authors observed a decoration of the biatomic steps with PTCDA molecules. Assuming the molecules standing upright to the step edges with their long axis parallel the step, as shown in figure 4.17, in principle all PTCDA oxygen atoms at the step could occupy positions very close to the substrate lattice planes. This position would give for the oxygen atoms a value of the coherent fraction close to the value for the substrate bulk. The resulting value for the coherent position would also be close to the value for the silver. The vectors of the carbon atoms would cancel each other out, because 12 atoms would occupy positions on bulk planes and 12 atoms positions in between them. This yields in an Argand diagram two opposing vectors of the same length. Hence, if such a situation exists, the value of the coherent fraction for the total carbon (occupying The Ag(111) terraces and the step edges as described) would decrease, however, the value for the coherent position would not change. It has to be pointed out that this situation can only exist, because the Ag(111) lattice plane distance (2.36 Å) corresponds approximately to the width of half a molecule (2.2 Å), as can be seen in figure 4.17.

The fitted coherent positions are in units of the lattice constant 2.36 Å, therefore, it seems to be reasonable that the distance of the upright standing molecules to the (111) terraces corresponds to one lattice constant. However, for step edges higher than two layers, it is also possible that this distance corresponds to more than one lattice constant. However, from the data of the present work, no conclusion can be drawn about the absolute adsorption height of the upright standing molecules.

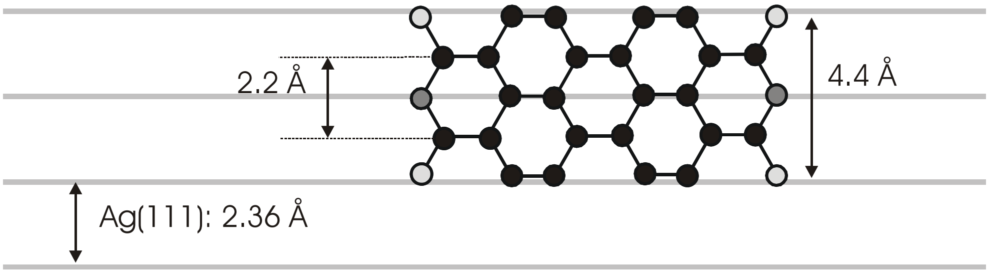

Figure 4.17: *Model for upright standing molecules at step eges of the silver crystal. The lattice planes of Ag(111) have a distance of* 2.36 Å. *The carboxylic oxygen atoms within the functional group exhibit in the molecules of the PTCDA bulk crystal a distance of* 4.4 Å.

Assuming that 10% of the molecules are decorating steps, the vectors in the Argand diagram would have to be corrected in the following way:

$$\overrightarrow{O1s}_{\text{high res}} = 10\% \cdot \overrightarrow{Ag} + 90\% \cdot \overrightarrow{O1s}^{\text{corr.}}_{\text{high res}} \tag{4.1}$$

The vector $\overrightarrow{O1s}_{\text{high res}}$ describes the actually measured high resolution result. For the correction vector, a bulk like vector, $\overrightarrow{Ag}$, with a coherent position of 1 and the measured value of the coherent fraction of the silver ($C_F^{\text{Ag}} = 0.9$) was used. By correcting the high resolution value with this bulk-like contribution of 10%, the coherent position of the low resolution data can be obtained. This is shown in figure 4.16. The values are listed in table 4.4.

O1s total results

beamtime J'03	spectra	C$_{P\ \mathrm{eff}}$	C$_{P\ \mathrm{eff}}$(Å)	C$_F$
prep. A - low res.	5	0.212 ± 0.011	2.859 ± 0.026	0.530 ± 0.058
prep. A - high res.	3	0.199 ± 0.015	2.818 ± 0.036	0.413 ± 0.027

beamtime N'03	spectra	C$_{P\ \mathrm{eff}}$	C$_{P\ \mathrm{eff}}$(Å)	C$_F$
prep. B - low res.	1	0.213 ± 0.020	2.861 ± 0.047	0.467 ± 0.080
prep. F - high res.	1	0.170 ± 0.020	2.760 ± 0.047	0.539 ± 0.080

beamtime N'04	spectra	C$_{P\ \mathrm{eff}}$	C$_{P\ \mathrm{eff}}$(Å)	C$_F$
prep. C - low res.	1	(0.170)	(2.760)	(0.312)
prep. D - low res.	1	(0.167)	(2.753)	(0.343)
prep. E - low res.	1	(0.182)	(2.788)	(0.172)

average (freshly prepared films)

	spectra	C$_{P\ \mathrm{eff}}$	C$_{P\ \mathrm{eff}}$(Å)	C$_F$
A+B - low res.	6	0.212 ± 0.010	2.859 ± 0.023	0.519 ± 0.058

average (structurally changed films)

	spectra	C$_{P\ \mathrm{eff}}$	C$_{P\ \mathrm{eff}}$(Å)	C$_F$
A+F - high res.	4	0.182 ± 0.013	2.799 ± 0.034	0.461 ± 0.086
corr. A+F - high res. with 10% bulk contr.		*0.212*	*2.874*	*0.480*

Table 4.4: *Coherent position and coherent fraction for the total oxygen of the monolayer phase, obtained in different preparations. The column "spectra" denotes the number of evaluated spectra. The errors correspond to the standard deviation of the results from the evaluated profiles. The errors for the results of beamtime N'03 were estimated, based on a confidence analysis for the C1s data of the monolayer PTCDA on silver(111) of Gerlach et al. [Ger 07]. The values obtained in preparation C, D and E in beamtime N'04 are not very reliable and therefore stand in parenthesis. The statistic of the O1s-NIXSW profile taken on preparation C is very low. Therefore, it is not appropriate to recalculate the result of preparation D, in the way it was done for the carbon. From the carbon results it was found that the surface quality in beamtime N'04 was not optimal, a high amount of molecules on step edges was assumed. The resulting values do not correspond to the molecules in the herringbone structure alone. Preparation E, however, corresponds to the defrosted precursor. The film was highly contaminated with water. Due to the described points, none of the result obtained in beamtime N'04 will be considered for the final result. The average results obtained on the structurally changed films were corrected with a Ag-bulk like contribution of 10 percent. With this correction the resulting coherent position is similar to the value of the low resolution data.*

4.5.5 Oxygen separation

The high-resolution O1s PE spectra exhibit a double peak feature. These two main peaks can be led back to the different chemical environment of the two distinct oxygen atoms in the PTCDA molecule, the carboxylic and the anhydride oxygen, respectively. Additionally to these two (*chemical shifted*) main peaks, a number of satellite peaks exist for each oxygen type. These satellites are explained in the so-called *sudden approximation* of the photoemission process. When a core hole is created, the final state can be one in which an electron is in an excited bound state. This process leaves less energy for the emitted photoelectron and gives rise to a satellite at lower kinetic energy (or higher binding energy) which is called a *shake-up satellite*. Therefore the peak features of each oxygen type (in PTCDA) is composed of a main peak and a number of broader satellites at higher binding energies [WooDel 94].

The PTCDA molecule contains two anhydride- and four carboxylic-oxygen atoms. Due to this stoichiometry, the peak area ratio should be 1 : 2 for anhydride and carboxylic oxygen, respectively.

Due to different structural parameters of the two oxygen types, the photoemission spectra should change in their shape in the range of the standing wave excitation energies. In Fig. 4.18 several PE spectra are displayed for which the x-ray excitation energy is near the Bragg condition. One can clearly observe that the relative intensities of the two peaks change as a function of x-ray energy. This indicates that the corresponding oxygen species are located at different heights above the Ag(111) lattice planes. These contributions can be separated in the PE spectra by peak fitting. With the appropriate fitting model, the NIXSW profiles and therefore, the coherent fraction and coherent position can be determined for the anhydride and the carboxylic oxygen atoms separately.

The unit cell of the monolayer structure contains two molecules. The exact lateral position of these two molecules on the Ag(111) surface has been revealed by Kraft et al. [Kra 06]. They found that the anhydride atoms are symmetry equivalent for each molecule in the unit cell. This yields for the anhydride oxygen 2 distinct positions per unit cell. The carboxylic oxygen atoms take in 2 symmetry equivalent positions for each molecule. Therefore, the

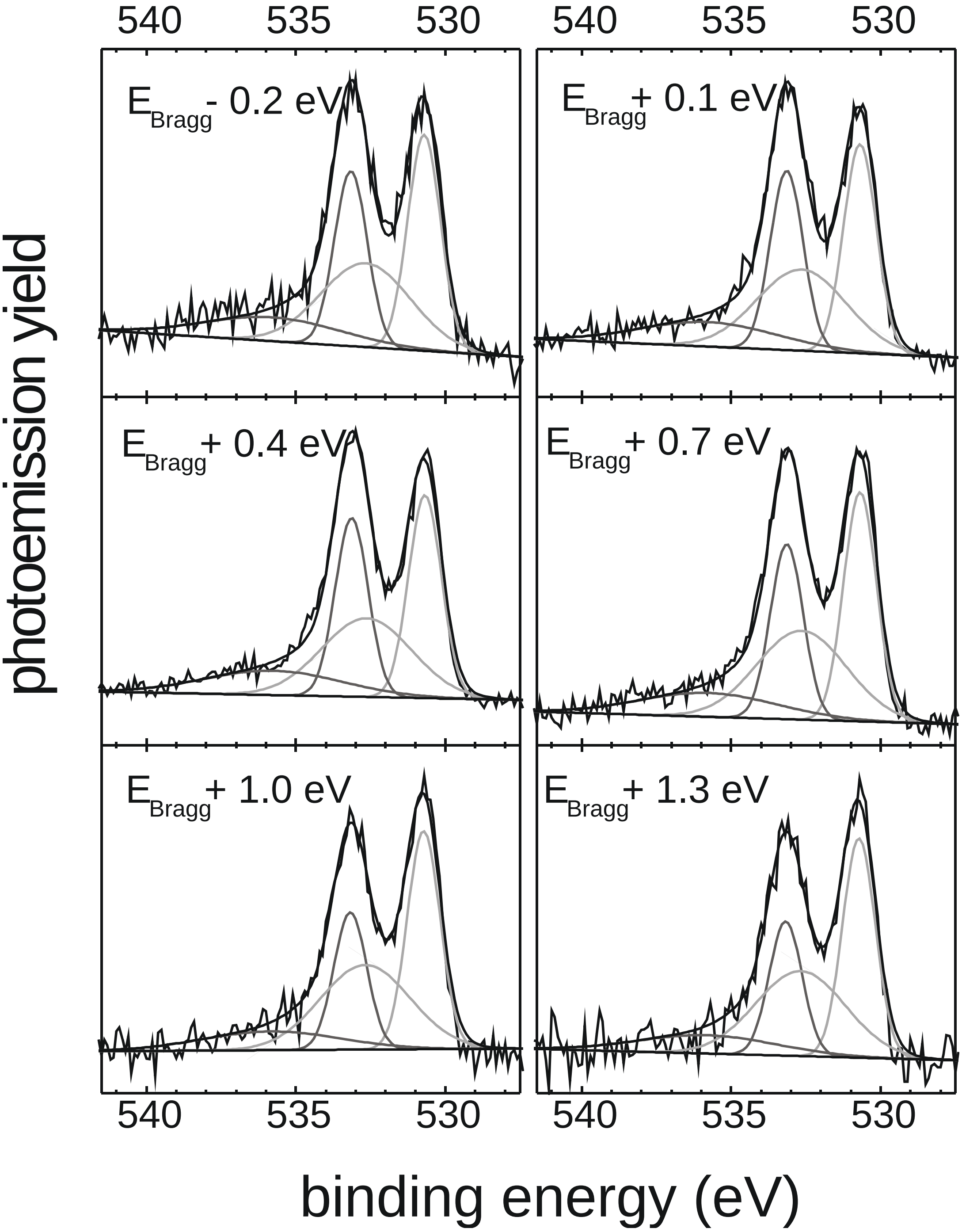

Figure 4.18: *O1s high resolution PE spectra of the standing wave on the monolayer. With increasing photon energy, a change in the peak-height ratio clearly can be seen. First the peak at higher binding energy is larger than the peak at lower binding energy. This ratio changes across the XSW scan to the opposite. The fitting was performed with the model described in the text. The Bragg energy was determined by the fit of the corresponding reflectivity curve.*

carboxylic oxygen atoms occupy 4 different positions in the unit cell [Kra 06]. The NIXSW results, obtained from the differential fitting, hence include 4 distinct adsorption sites for the carboxylic oxygen and 2 distinct adsorption sites for the anhydride oxygen. However, it was found that these are not individually resolved in the photoemission spectrum.

Fitting model

For individual evaluation of the two oxygen types, the knowledge of the peak contributions to the total spectrum is essential. One has to find a fitting model for the PE spectra which separates the distinct contributions as exact as possible.

In the process of photoionization, core level electrons are ejected. Depending on their original chemical state and the physical processes involved, they have different kinetic energies. Therefore the PE spectra are composed of various peak contributions with appropriate shapes. Due to instrumental resolution in a measurement, a broadening of these peaks occurs in the spectra. Typically, such a peak can be described with a convolution of a Gaussian and Lorentzian function. The Gaussian contribution can be led back to the instrumental response, the photoelectron-line shape and to broadening due to Doppler and thermal effects. The Lorentzian contribution is due to lifetime broadening.

In order to decompose the distinct peak contributions in a PE spectrum, one has to find a suitable fitting model leading to the measured spectral envelope. In such a fitting model, the underlying physics has to be taken into account. The number of chemical states correspond to the minimal number of peaks. Due to stoichiometric reasons relative intensities have to be constrained, as well as peak widths of peaks having an identical physical origin.

In literature a fitting model for the O1s transition of the molecule PTCDA on InSb(111)A is proposed [Unw 03]. The shape of the there given PE spectrum looks similar to the shape of the O1s PE spectrum of a monolayer PTCDA on Ag(111). In the fitting model Unwin et al. presented for the PE spectrum, each of the two chemically shifted oxygen atoms leads to a peak at a partic-

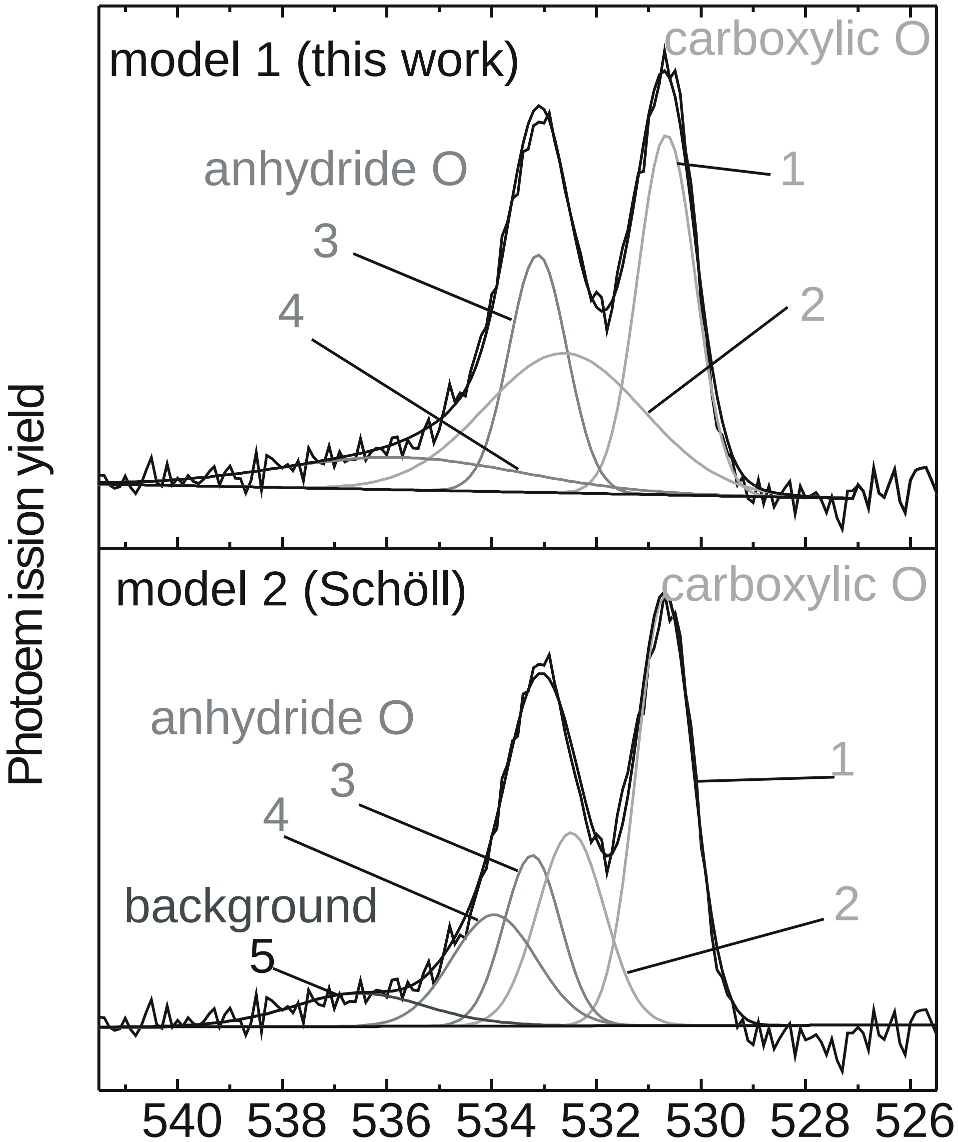

Figure 4.19: *Off-Bragg O1s PE spectrum of the monolayer. Peak 1+2 (light grey): carboxylic O; peak 3+4 (grey): anhydride O. The ratio of carboxylic oxygen to anhydride oxygen is 2:1. Model 1: fitting model deduced in this work (see text); model 2: fitting model developed by A. Schöll. The dark grey peak (5) in model 2 is attributed to the background. In both spectra, a linear background was fitted.*

ular binding energy and also to appropriate shake up features. However, the substrate, used in their work was different, therefore their fitting model only can be used as a guideline. In the present work a fitting model was developed for the decomposition of the O1s PE spectra on the basis of the NIXSW data.

Five high resolution off-Bragg spectra with high statistics were recorded in beamtime N'03. Among these spectra there is one spectrum which is different from the others, so it was dismissed and not used for the peak decomposition. Using the program CasaXPS, different peak features and backgrounds were fitted to the remaining spectra.

In order to minimize the fit residuals for all four off-Bragg spectra, various number of peaks (the number of peaks was tried to keep small), various peak shapes (Gaussian, Lorentz, Doniach Sunjic, and a number of Voigt peaks), and a linear background, respectively a Shirley background were tested. The peaks had to be attributed to the distinct origins, i.e. carboxylic oxygen, anhydride oxygen, or background, respectively. For the development of the fitting model several constraints on the peaks had to be fulfilled. Due to stoichiometric reasons, the peak area ratio between carboxylic and anhydride oxygen (including the shake up's) had to be constrained to 2 : 1. Also the full width of half maximum (FWHM) of the two main peaks were constrained to be equal in value, because they have the same physical origin, namely the O1s transition.

After testing the different models with the corresponding constraints, a selection of the best fitting models for the off-Bragg spectra was chosen. This selection included models with 3, 4, and 5 peaks. The residuals from the fit of the photoemission spectra gave the first estimation of the quality of the model. By applying the different models to all PE spectra of the excitation energies in a standing wave[3], the coherent positions and fractions for the two oxygen types were evaluated. Two parameters determined the "best fitting" model. The residuals of all NIXSW-PE spectra had to be minimal, and the coherent

---

[3] The fitting procedure of the PE spectra of the standing wave experiment was as follows: The peak positions, the FWHM, the peak ratios of the main peak and the shake-up peaks were constrained in the fit of the standing wave PE spectra. Only the total yields for the anhydride and carboxylic oxygen were left as free parameters. The fitting parameters are given in table 4.5a.

fraction of the resulting fit on the NIXSW profiles had to be maximized for both oxygen types. A high value for the coherent fraction indicates a good separation of the different peak contributions in a PE spectrum. An incorrect fitting model leads to a mixing of the distinct peak contributions which yields lower values for the coherent fractions.

The best fitting result was obtained with four pure Gaussians peaks. It is shown in the upper spectrum of figure 4.19. In the following this model will be named *model 1*. The presented spectrum is an O1s spectrum, taken at an off-Bragg photon energy of 2.618 keV. The major peak at a binding energy of 530.7 eV is mainly due to the carboxylic oxygen. The minor peak at a binding energy of 533 eV originates from a combination of the anhydride oxygen peak and a shake-up feature from the carboxylic oxygen. The broad peak around 535.7 eV is a shake-up feature of the anhydride oxygen (see appendix F). The fitting parameters are shown in table 4.5 a.

An alternative model for fitting the PE spectra was proposed from Schöll [Sch 05a]. This model will be named *model 2*, it is shown in figure 4.19. Schöll investigated the monolayer phase of PTCDA on Ag (111) at room temperature with high resolution PE experiments. He deduced the fitting model from the comparison of PE spectra of several organic species adsorbed on different surfaces (e.g.,NTCDA, NDCA, ANQ, BPDCA on Ag(111) and Au(111)). The fitting parameters are shown in table 4.5b for this model. The model 2 was tested on the NIXSW data, too. Contrary to model 1, the shake-up peak of the carboxylic oxygen has less intensity (only 67% of the carboxylic shake up in model 1). The anhydride shake-up feature proposed in model 1 is attributed to the background in model 2. However, the NIXSW results (shown in table 4.6) do not change significantly if this peak is attributed to the anhydride oxygen in model 2.

a.) model 1 (this work)

	Position (eV) (relative to the carbox. O)	FWHM (eV)	area(%) (off Bragg)
carboxylic (1)	0 (BE 530.67 eV)	1.30	32.3
carboxylic satellite (2)	+1.95	3.53	34.2
anhydride (3)	+2.45	1.30	21.3
anhydride satellite (4)	+5.09	5.42	12.2

b.) model 2 (Schöll)

	Position (eV) (relative to the carbox. O)	FWHM (eV)	area(%) (off Bragg)
carboxylic (1)	0 (BE 530.70 eV)	1.27	43.2
carboxylic satellite (2)	+1.79	1.79	22.9
anhydride (3)	+2.53	1.27	17.1
anhydride satellite (4)	+3.26	1.90	16.7
background (5)	+5.84	3.00	–

Table 4.5: *Fit results for the energy positions, line widths and relative peak areas of the PE and satellite peaks in the O1s spectrum for model 1 and the model 2.*

The NIXSW results, deduced by the two models, are shown in the Argand diagram of figure 4.20. In both models, the result for the vertical distance is the same for the carboxylic oxygen. For the anhydride, the resulting vertical distance is different. In model 2 it comes out to be closer to the carboxylic oxygen (by 0.1 Å, this corresponds to 34% of the difference in the differential distance!) compared to the result of model 1.

However, the length of the vectors, derived from model 2 are shorter for both oxygen positions ($\Delta C_F = 0.07$, and 0.12 for the carboxylic and anhydride oxygen, respectively). The vector length represents the coherent fraction which corresponds to the distribution of the oxygen species. These results reveal that the model 1 of this work is the more appropriate one for differential fit of the O1s-PE spectra, because the higher the coherent fraction is, the better is the separation of the two peak contributions. That means that in the result of the fit with the model 2 by Schöll, the peak contributions of the two oxygen species are mixed up, which yields a lower coherent fraction and coherent positions, which are closer to each other. Therefore, the model of this work seems to be the more reliable one.

For chemical shifted atoms, located on different vertical positions the NIXSW method, hence, is a nice tool for the determination of the number, the shape and the position of distinct peaks in the corresponding PE spectrum.

PCA

The Principal component analysis (see appendix G) for the oxygen spectra proposes two components. Applying these two components to the spectra with the target factor analysis, the change of the spectra in the standing wave becomes nicely visible. This is especially the case for the high resolution data from beamtime J'03, which have not such a good statistic. The fit of this smoothed spectra gives also smoother NIXSW profiles compared to those that are obtained from the fit of the raw data. Anyway, the resulting values for the coherent position and fraction remain the same for the processed and unprocessed data. Therefore, the results presented here were obtained from the measured spectra without any further processing.

The low resolution data (obtained on the freshly prepared films) gives two

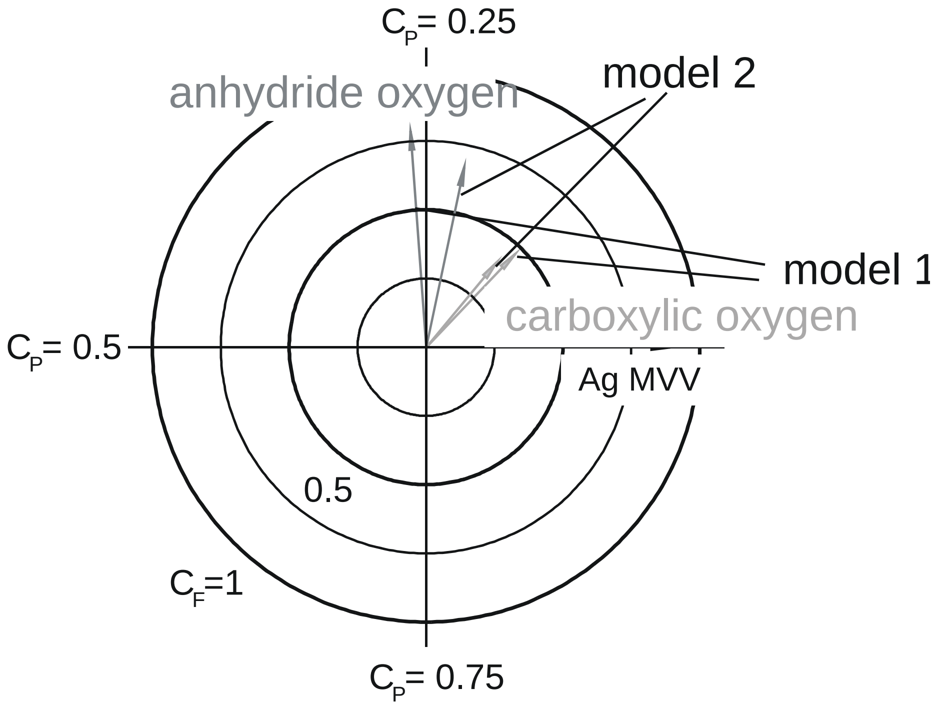

Figure 4.20: *Argand diagram for the NIXSW result of the monolayer. The resulting vectors deduced from the two different fitting models are given. It can be seen that the vectors obtained from model 1 are longer.*

components for the oxygen, as the high resolution (obtained on the structurally changed films) data do. However, it was not possible to do a proper fit to this data, in order to divide the different components from each other. Only the high resolution data was useful for this.

Merged spectra

In order to get a sufficient counting statistics, the acquisition time for a high resolution NIXSW scan can take six hours and more. If during that time instabilities in the photon current or of the monochromator occur, the whole dataset can become useless. To avoid the loss of spectra, the high resolution data of the second period in N'03 were taken into two steps with shorter acquisition times. Two NIXSW scans, with 16 energy steps each, were taken very close to the Bragg energy. Two more scans were taken afterwards with only 4 energy steps, consisting of 2 points close to Bragg energy and 2 points

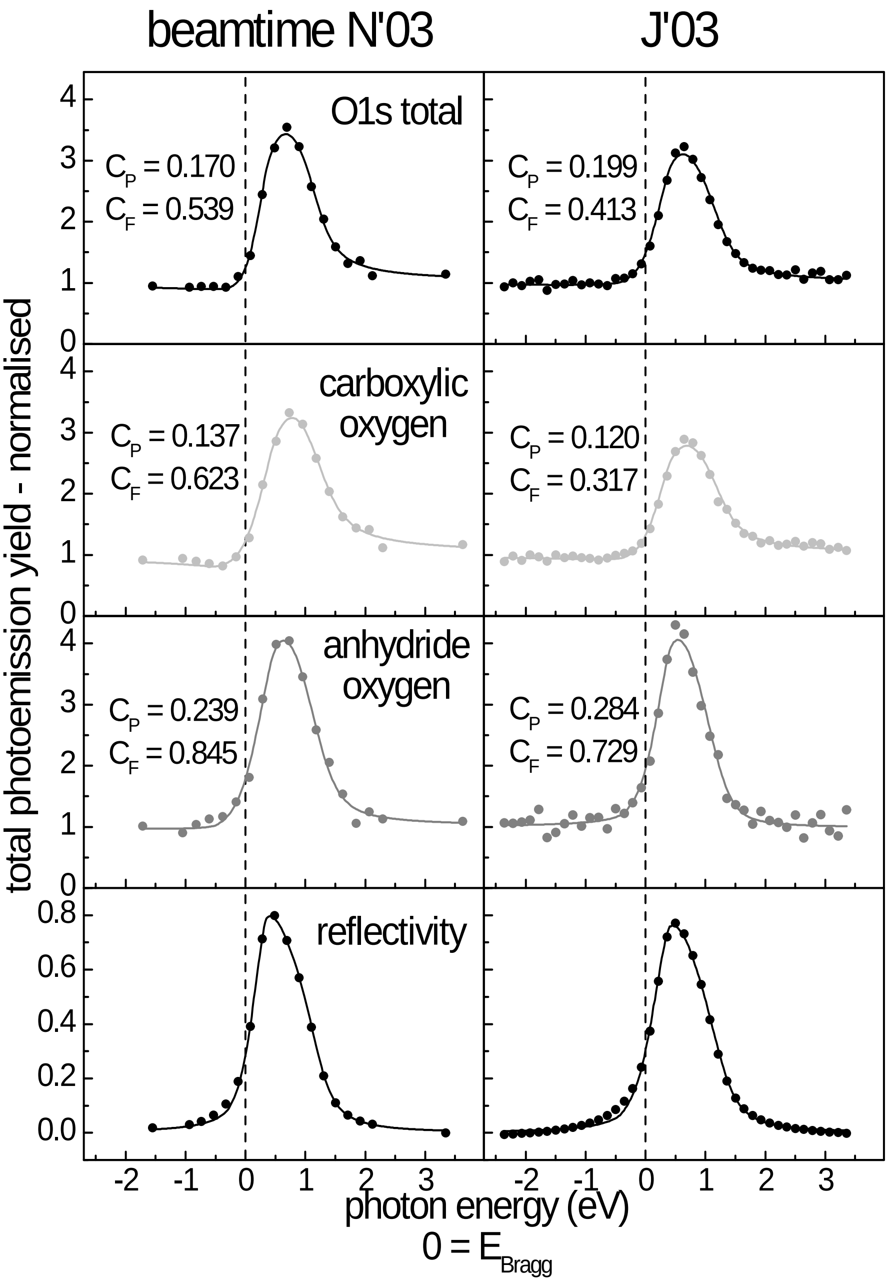

Figure 4.21: *This figure shows the measured NIXSW profiles (dots) and the appropriate fits (continuous line) of the beamtimes N'03 (left) and J'03 (right), obtained from the high resolution PE spectra. The corresponding values for the coherent position and coherent fraction are given. The profiles for the carboxylic and anhydride oxygen stem from the differential fits of the PE spectra. The profiles for the N'03 data were measured in 2 steps and subsequently merged (see text). The profiles for the J'03 data originate from the addition of three high-resolution O1s spectra.*

at off-Bragg energy. In each case, only one scan could be analyzed due to problems with the photon current.

The four point reflectivity curve was normalized to the 16 point reflectivity curve. The normalization was performed in the following way. The intensity of the four point spectrum was normalized to the 16 point spectrum by dividing the reflectivity curves by the photon current (meshI0). Then the two central points (of the four point scan) were fitted to the 16 point curve by linear variation of the energy axis and the intensity axis. The change in the energy axis became necessary due to small shifts (ca. 0.1 eV) of the monochromator which can arise e.g. from small differences in the temperature of the monochromator. The gained energy shift was applied to the NIXSW spectra as well. The intensity normalization was applied to the NIXSW profiles in the same way as for the reflectivity curves. The resulting fits are shown in Figure 4.21 on the left.

Results

The statistics for the high resolution data sets from J'03 are not as good as the statistics for the high resolution data sets from N'03. In order to have comparable statistics, the three high resolution O1s-photoemission spectra from J'03 were added up and evaluated afterwards. The results are consistent with those obtained from the averaged results of the single scans from J'03. The fit of the NIXSW profile is shown in figure 4.21 on the right hand side. For the two oxygen species, the results for the high resolution spectra are shown in table 4.6. The more reliable results are those obtained from model 1. The coherent positions for the total and for the carboxylic oxygen differ only by 0.06 Å and by 0.04 Å for each beamtime (see table 4.6). However, the coherent positions for the anhydride oxygen differ much more strongly by 0.11 Å. This striking difference can be seen in the Argand diagram shown in figure 4.22.

This difference has several reasons. The monochromator did not run very stable in beamtime J'03. Especially the data acquisition for the high resolution scans took a long time. A small drift in the photon energy could have changed the results significantly. Another reason is that the fitting results for an NIXSW profile, yielding a coherent position in the region of $C_P = 0.25$ de-

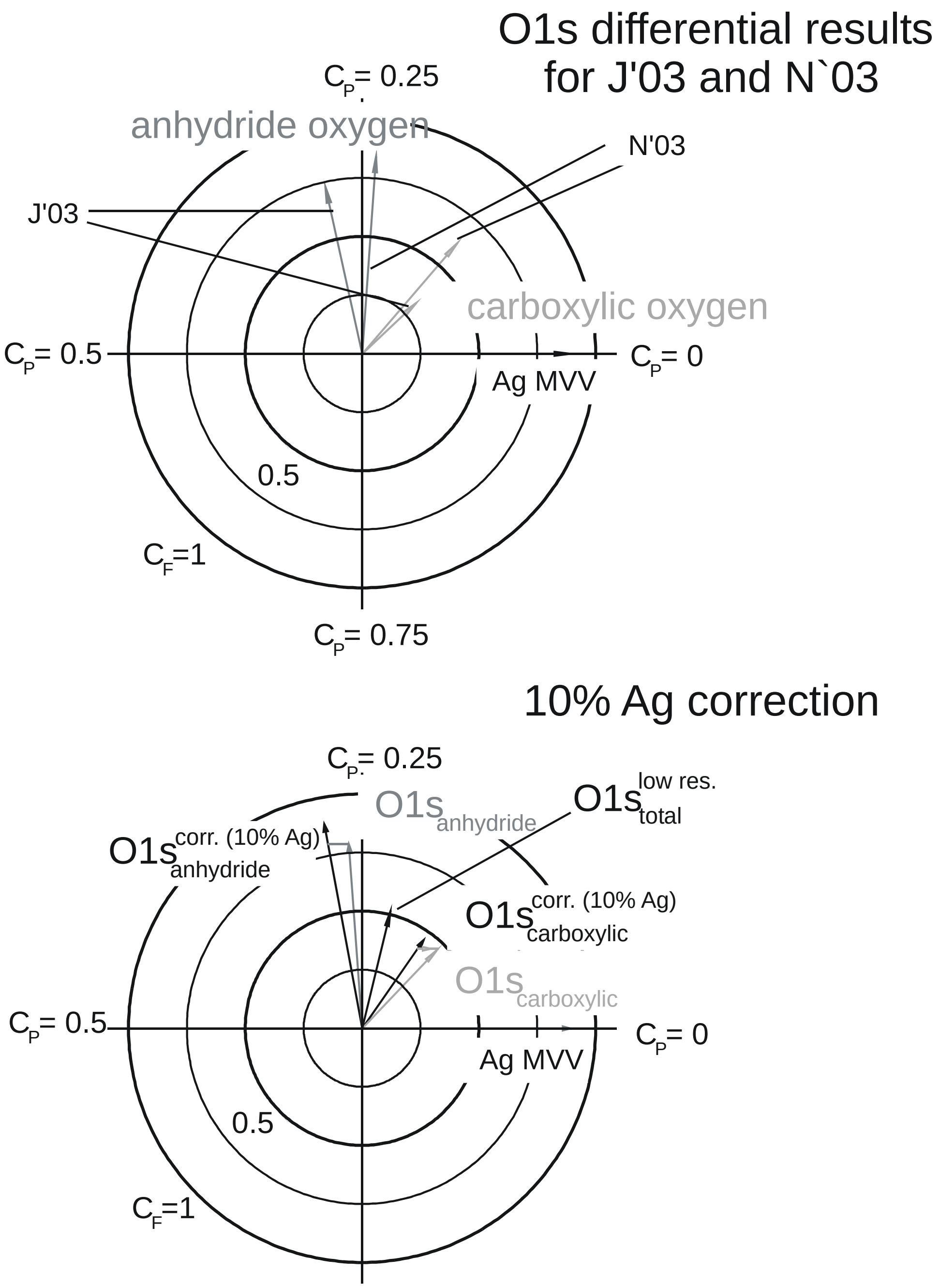

Figure 4.22: *Top: Argand diagram showing the vectors for the chemically different oxygen atoms. The coherent positions for the caboxylic oxygen atoms are identical in both beamtimes. This is not the case for the anhydride oxygen atoms. Bottom: Argand diagram showing the averaged vectors of the diagram above. Additionally, a correction with a bulk-like contribution of* 10% *is presented.*

pends very sensitive on small changes in the data. Regarding the data and the fit for the NIXSW profile of the anhydride in figure 4.21, no actual difference can be seen by eye. By comparing the data and fits in one graph (figure 4.23), it can be seen, that the differences in the data are only small.

As the most important reason for the difference can be assumed the different preparation conditions for the two films, as described in section 4.5.2. The film of preparation A obtained in beamtime J'03 exhibits structural changes with time (or with beam irradiation). The film of preparation F (beamtime N'03) was freshly prepared, however, due to its particular preparation, it obviously exhibits structural changes, too. As can bee seen from the results (coherent position and coherent fraction) of the total oxygen in table 4.6, these observed structural changes are not exactly the same for preparation A and preparation F. It is possible that in fact, the vertical position of the anhydride oxygen exhibits such a difference (0.11 Å) in the two films.

Because the values for the coherent position of the carboxylic oxygen are similar within the errors, and because the data of the NIXSW profiles for the anhydride look very similar, it seems to be reasonable to choose the average value of both results with an adequate high error as the final result for the high resolution NIXSW scans.

Regarding the results for the coherent position and fraction of the total oxygen, identical result should principally be obtained by adding the vectors of the anhydride and carboxylic oxygen in the Argand diagram with respective weights. This is shown in figure 4.24. The vectors of the total oxygen for beamtime J'03 differ only slightly from the added vectors of the carboxylic and the anhydride oxygen. The vectors for the beamtime N'03 vary in length. Both differences likely have statistical reasons. As noted before, the coherent position and fraction of the anhydride oxygen is very sensitive on the fit of the NIXSW profile. Therefore, in this case, it can be assumed that the statistical data spread of the NIXSW profiles is the reason for the difference in the values of the coherent fractions.

Concerning the bulk position correction for the high resolution O1s total

Monolayer results (structurally changed films)

Total oxygen

	spectra	$C_{P\ \mathrm{eff}}$	$C_{P\ \mathrm{eff}}$(Å)	C_F
prep. A	3	0.199 ± 0.015	2.818 ± 0.036	0.413 ± 0.027
prep. F	1	0.170 ± 0.020	2.760 ± 0.047	0.539 ± 0.080
prep. A+F (av.)	4	0.182 ± 0.013	2.799 ± 0.034	0.461 ± 0.086

O1s carboxylic

	spectra	$C_{P\ \mathrm{eff}}$	$C_{P\ \mathrm{eff}}$(Å)	C_F
model 1- prep. A	3	0.120 ± 0.018	2.636 ± 0.043	0.317 ± 0.025
model 1- prep. F	1	0.137	2.676	0.623
model 1 (av.)	4	**0.128 ± 0.012**	**2.656 ± 0.028**	**0.470 ± 0.216**
model 2 (av.)	*4*	*0.139 ± 0.003*	*2.682 ± 0.006*	*0.403 ± 0.115*

O1s anhydride

	spectra	$C_{P\ \mathrm{eff}}$	$C_{P\ \mathrm{eff}}$(Å)	C_F
model 1- prep. A	3	0.284 ± 0.010	3.024 ± 0.023	0.729 ± 0.011
model 1- prep. F	1	0.239	2.916	0.845
model 1 (av.)	4	**0.261 ± 0.032**	**2.970 ± 0.076**	**0.787 ± 0.082**
model 2 (av.)	*4*	*0.217 ± 0.020*	*2.864 ± 0.047*	*0.670 ± 0.089*

Table 4.6: *Results of the differential fitting for the monolayer with model 1 of this work and with model 2 proposed from Schöll. The results obtained from the fit of model 1 are more reliable, as discussed in the text. The column "spectra" denotes the number of evaluated NIXSW profiles. For comparison, the results for the total oxygen are given. The errors for the results of the data from preparation A (beamtime J'03) correspond to the standard deviation of the results from the three evaluated profiles. For the error of the averaged results, the standard deviation resulting from two datasets was taken: 1) the results of the merged profiles obtained in preparation F (beamtime N'03) and 2) the results from the fit of the sum of the three datasets from preparation A (beamtime J'03).*

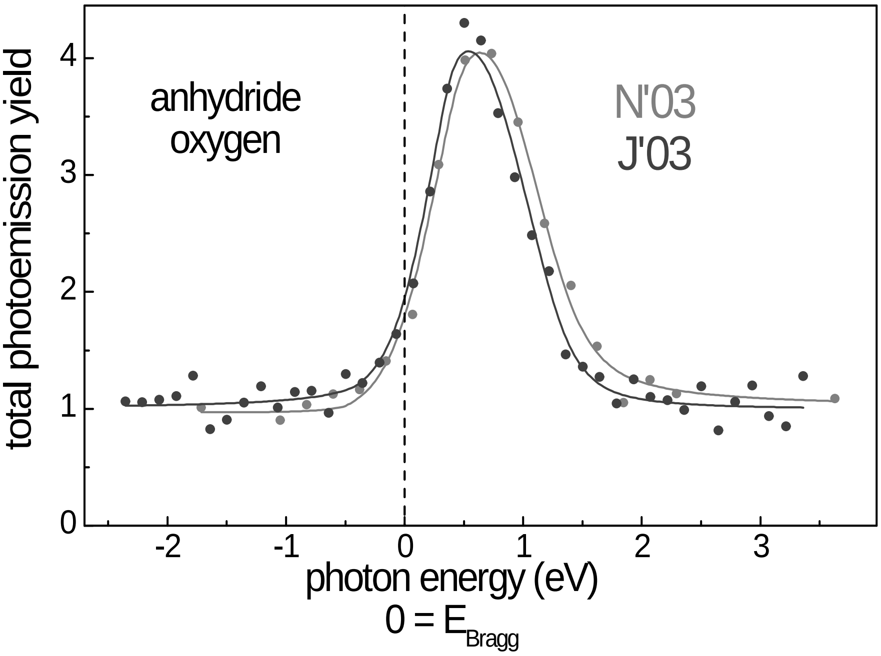

Figure 4.23: *NIXSW profiles (data points and corresponding fits) for the anhydride oxygen of the monolayer for the two beamtimes in J'03 and N'03 are shown. The difference is only small, however, the resulting values for the coherent positions exhibit significantly differences (see text).*

result (see section 4.5.4), the corrected vectors of the two types of oxygen change slightly in their vertical position when the correction with a 10% bulk-like contribution to the differential electron yield was applied. The resulting vectors are shown in the Argand diagram in figure 4.22, the resulting values are listed in table 4.7. It has to be pointed out that this correction model only is based on assumptions, nonetheless the correction of the high resolution results nicely reproduce the low resolution results.

It can be concluded that the main result of this investigation of the monolayer is, that the molecules in the monolayer at room temperature are distorted. The carboxylic oxygen atoms lie below and the anhydride oxygen atoms lie above the perylene core of the molecule. The low resolution results of the effective coherent position and the coherent fraction for the carbon and for the

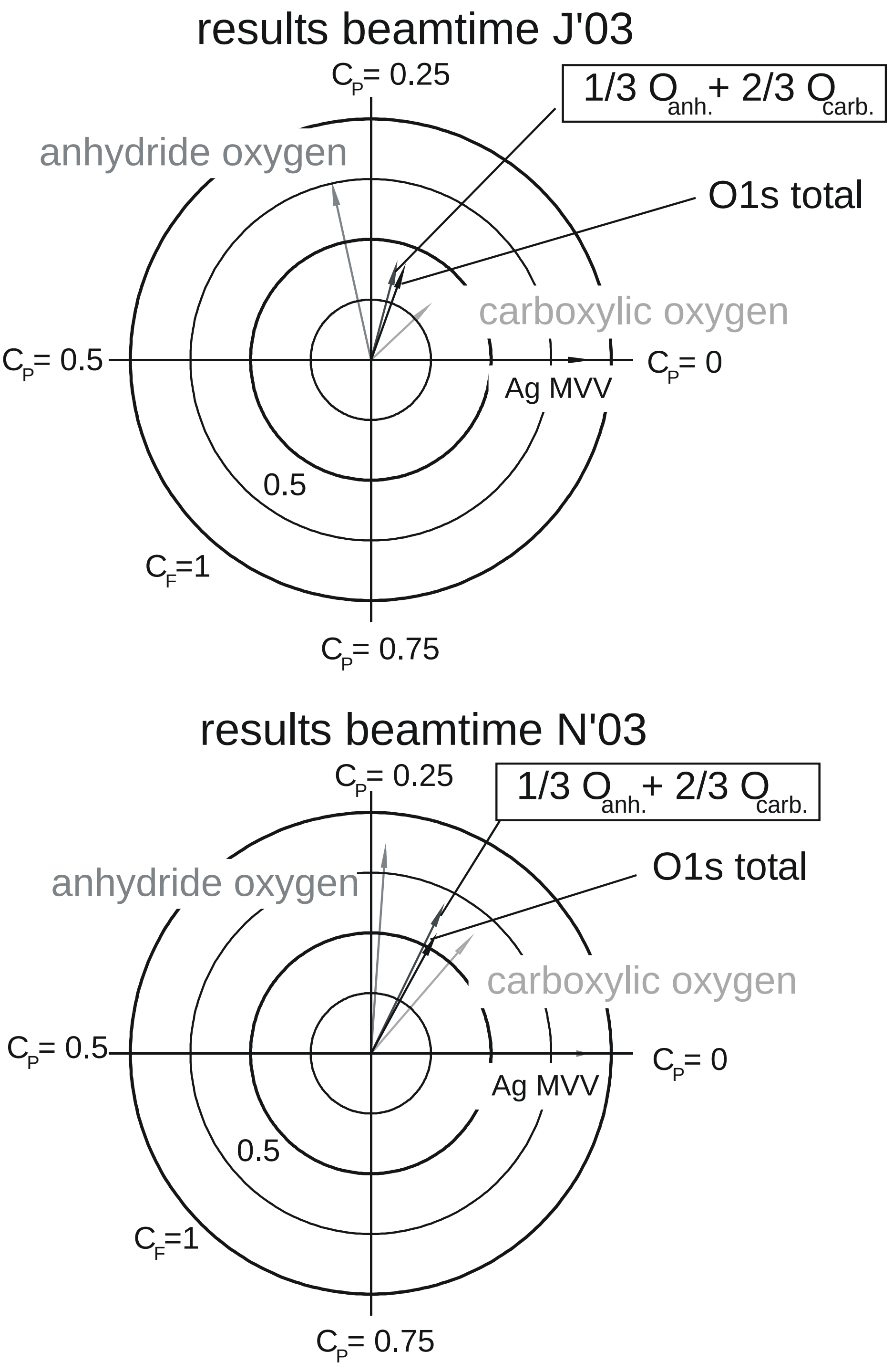

Figure 4.24: *Argand diagram for the high resolution oxygen results. The vectors for the anhydride and carboxylic oxygen, obtained from the differential fits are shown. In addition, the vector for the total oxygen, obtained from the addition of the anhydride and carboxylic oxygen vectors and, on the other hand, obtained from the direct evaluation of the data are displayed. However, the vectors for the total oxygen, received on the two ways differ slightly for beamtime J'03 and vary in the length for beamtime N'03 (see text).*

differential results with a10% bulk like correction

	spectra	C_P	$C_P[\mathring{A}]$	C_F
O1s carboxylic	4	0.153	2.714	0.459
O1s anhydride	4	0.279	3.012	0.887

Table 4.7: *Differential results for the monolayer averaged over two preparations (J'03- preparation A and N'03- preparation F), corrected by a bulk-like contribution of 10%. The column "spectra" denotes the number of evaluated spectra.*

total oxygen are reliable for the chosen multipole parameters. In chapter 6, the discussion of these results is presented in comparison to the results of the precursor.

Multipole parameter Q - Error estimation

For the evaluation in the present work, Q was fixed to $Q = 0.31$ ($\gamma = 1.32$) for both elements, oxygen and carbon (see [Sch 01]). This value was measured on the same system PTCDA on Ag(111) before. Theoretically obtained values for Q are much lower. However, the above value seemed to be a better choice for the system investigated in the present work, because a lower value of Q (e.g. $Q \leq 0.26$) leads to an unphysical results in the coherent fraction for the anhydride oxygen. The value of the coherent fraction should not exceed unity $C_F \leq 1$, however, with a value of $Q \leq 0.26$ this is the case for the anhydride oxygen. The influence of the parameter Q on the effective coherent positions is shown in figure 4.25 for the room temperature phase. It can be seen that no strong influence on the effective coherent positions is found for the anhydride oxygen ($\leq$ 1%) and for the carbon ($\leq$ 5.5%). For the carboxylic oxygen, however, the chosen value of Q can change the result quite drastically. For $Q = 0.26$ the value of the coherent position is 14% larger and for $Q = 0.36$ the value of the coherent position is 17% smaller than the value obtained with $Q = 0.31$.

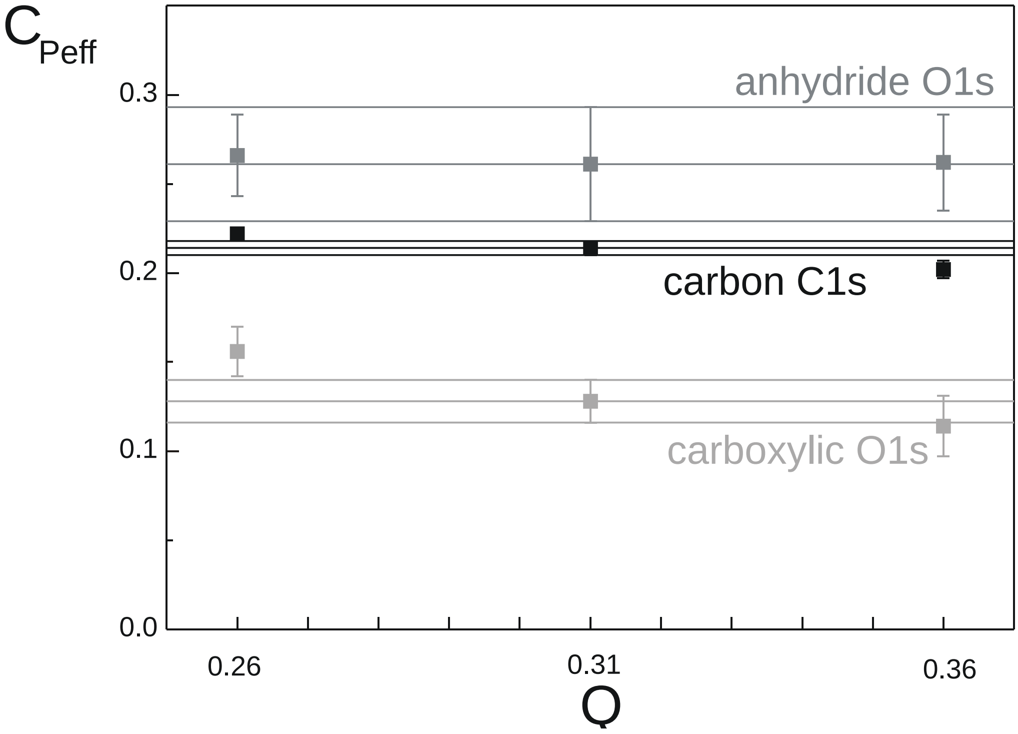

Figure 4.25: *Results for the effective coherent position obtained from fits on the PTCDA/Ag(111) data at room temperature. The fits were done with various values of the asymmetry parameter Q (from* $Q = 0.26$ *to* $Q = 0.36$*) on all data sets. The given error is the statistical error. The solid lines correspond to the statistical error of the data evaluated with* $Q = 0.31$*.*

Chapter 5

NIXSW – the precursor phase

PTCDA deposited on Ag(111) below 160 K yields a metastable phase, which is chemisorbed, but no long-range order exists. In the following this phase will be named *precursor*, since it was believed that this phase due to its metastability corresponds to a precursor of the stable phase at room temperature. More information about the properties of the precursor phase, especially in comparison to the room temperature phase, can be found in chapters 2 and 6, respectively.

5.1 Experimental

The precursor NIXSW data were taken in two beamtimes, November 2003 and November 2004. Only one precursor film was prepared in the first beamtime, and two different films were prepared in the second beamtime. For the preparation of the precursor phase, the Ag(111) single crystal was cleaned as described in chapter 4.1. Subsequently the sample was cooled down to low temperatures (see table 5.1), this temperature was kept during the whole experiment. The organic films were prepared by evaporating the organic material from a Knudsen cell. The PTCDA coverage of the precursor state amounts to less than one monolayer (of the room temperature phase) on the Ag(111) sample. In order to prepare a film below this coverage, the Knudsen cell was calibrated. For the different preparations, the coverages and sample temperatures during preparation and experiment are listed in table 5.1.

The nominal Bragg energy at 100 K for normal incidence has a value of $E_{\mathrm{Bragg}} = 2637.6\,\mathrm{eV}$, which is ca. 10 eV higher than the value at room temperature. This is due to the thermal contraction of the crystal lattice (see chapter 4.1). The (111) lattice constant at 100 K has a value of 2.3503 Å as calculated in chapter 4.1.

precursor preparations

abbr.	preparation	coverage (1≡monolayer of the RT phase)	T_{sample}
N'03	Nov. 2003	0.30 ± 0.10	ca. 100 K
N'04a	Nov. 2004 1st prep.	0.56 ± 0.10	ca. 80 K
N'04b	Nov. 2004 2nd prep.	0.66 ± 0.10	ca. 80 K

Table 5.1: *PTCDA coverages for the precursor and sample temperatures during the different beamtimes. The coverages were estimated by comparing the C1s XPS-signal of a complete monolayer (of the room temperature phase (RT)) with the C1s signal of the precursor. The error was estimated. The first column gives the abbreviations for the different preparations used in the text.*

Changes in the shape of the O1s photoemission spectra were found during the measurements (e.g., see figure 5.4 on page 111). This phenomenon occurred by varying the beam position on the sample. However, in some cases it occurred also during measurements on the same sample spot. This phenomenon, due to the co-adsorption and desorption of water, will be described in detail in section 5.3.2.

When the standing wave experiment was done on the precursor in N'03 for the first time, only one spot on the sample was used for the measurements. During data acquisition using the Ag(111)-Bragg reflection, the sample was not moved relative to the beam and the photoemission spectra for the same excitation energies did not change during the experiment. Then, the experiment was performed in the ($\bar{1}11$)-Bragg condition and afterwards, for comparison, in the (111)-Bragg condition again. For the data acquisition of the different reflection conditions, the sample was moved relative to the beam. Surprisingly, the latter O1s spectra of the (111) plane were completely different to the data measured before on this plane. Since no beamtime was left, the investigation of these changes in the spectra was done in the following beamtime N'04. This time, the sample was moved several times relative to the beam and the oxygen-spectra exhibited striking differences in their shapes. It was found that the observed changes in the data were due to the contamination of water of the sample, as it is described in detail in section 5.3.2. Therefore, the results of beamtime N'04 were not reliable for the precursor.

The data taken in N'03 are much more trustworthy, because in those experiments only one spot on the sample was irradiated with the beam and photon-stimulated desorption could take place (see section 5.3.2). Besides, in N'03, the condensation of water on the sample was presumably smaller compared to the beamtime N'04, because the sample temperature was slightly higher (see table 5.1). The base pressure of the chamber was identical for both beamtimes ($p = 2 - 5 \times 10^{-10}$ mbar), but in N'03 the chamber was baked out already six days earlier with respect to the experiment, which could also be a reason for a lower amount of water in the chamber.

The same multipole parameters were used for the evaluation of the precursor as for the monolayer (see chapter 3.3.4).

5.2 Carbon results

In the precursor phase, the PTCDA molecules on silver (111) exhibit no molecular ordering [Ere 03] [Kil 02a], however if is known from NEXAFS [Sch 05a], and STM [Tem 06a] experiments that the molecules lie flat on the silver (111) substrate. Therefore, a non-neglible coherent fraction is expected from the NIXSW results for the carbon.

A typical off-Bragg photoemission spectrum for C1s transition is shown in figure 5.1. For the C1s spectra, it was only practicable to subtract a Shirley background (for the Shirley function see appendix E.1). Due to the low statistic in the PE spectra and the limited width of the spectra, no region could be defined for adapting a linear background. Therefore, in all C1s PE spectra of the standing wave experiment, a Shirley background was subtracted. Figure 5.1 also shows an exemplary NIXSW profile and the corresponding reflectivity curve for the C1s transition.

In the gas phase, the PTCDA molecule has seven chemically different carbon positions (see figure 4.4). Because of the relative high pass energy of the electron analyzer (47 eV), the distinct contributions, due to chemical shift and due to satellites, are not dissolved in the survey spectrum of figure 5.1. The binding energy, shown in figure 5.1, is calibrated with spectra from Schöll for the precursor [Sch 05a].

precursor C1s results

	cov. (monol.)	spectra	PE (eV)	C_F	$C_{P\ \mathrm{eff}}$	$C_{P\ \mathrm{eff}}$(Å)
N'03	0.30	3	46	0.621 ± 0.063	0.193 ± 0.010	2.805 ± 0.024
N'04a	0.56	5	59	0.344 ± 0.021	0.189 ± 0.012	2.795 ± 0.029
N'04b	0.66	8	96	0.321 ± 0.012	0.236 ± 0.009	2.904 ± 0.021

Table 5.2: *Fitting results for the C1s NIXSW data. PE is the corresponding pass energy of the electron analyzer. The errors correspond to the standard deviation of the results for the different NIXSW scans. In the column spectra the number of evaluated spectra is given.*

Depending on the preparation of the film, different results for the vertical carbon distance were obtained. These values are listed in table 5.2. The coherent fraction for the carbon is significantly higher in the N'03 data compared to the N'04a and N'04b data. One reason for this is presumably the lower coverage of PTCDA in the earlier beamtime. The probability for the molecules on the surface to be influenced by other PTCDA molecules is much lower. Another reason could be the co-adsorption of water, in N'04, which was clearly found in the oxygen data, even though the C1s spectra of the precursor show no evidence for this. Whereas the O1s profiles exhibit significant changes due to photon-induced desorption of water, the C1s profiles did not change during x-ray irradiation of the sample. Therefore, it is not clear, if the co-adsorption of water influences the position of the PTCDA molecules on the surface.

For preparations of N'03 and N'04a (with the pass energies of 46 and 59 eV, respectively), the value for the coherent position for carbon comes out to be

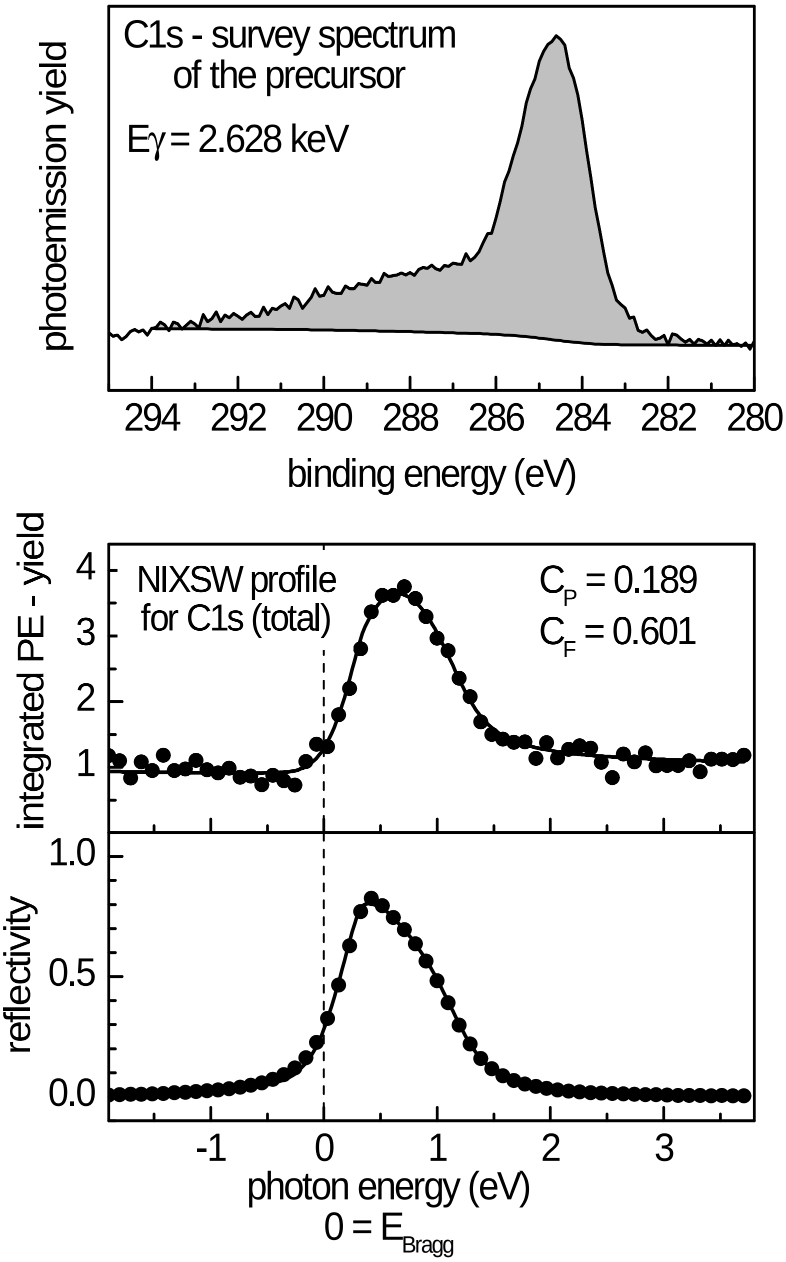

Figure 5.1: *Top: survey spectrum of the C1s-transition for the monolayer. The pass energy of the electron analyzer was* 47 eV*. For analyzing the peak area, a Shirley background was adapted to the spectrum. Center: C1s NIXSW profile and reflectivity curve (bottom) for the monolayer phase. The data were taken in beamtime N'03 with a pass energy of* 47 eV *(Pt1_139). The points represent the data and the solid lines the corresponding fit. The corresponding results for the coherent position and fraction are given in the figure.*

approximately 2.8 Å. This value shows no change for the different coverages of N'03 and N'04a. In the case of preparation N'04b (with a low resolution pass energy of 96 eV), the value is 0.1 Å higher. However, due to the problem of water adsorption in beamtime N'04, the results obtained from beamtime N'03 are the most reliable results. For the discussion in chapter 6, only this values will be taken into account.

5.3 Oxygen results

In the following section the evaluation of the oxygen data for the precursor phase will be presented. Due to the co-adsorption of water, many different peak shapes in the PE spectra were observed. It had to be found out, whether among those there were spectra which represent the *intrinsic* O1s spectra of the precursor, i.e. spectra of an uncontaminated sample. With the 'intrinsic precursor' spectrum, we refer to the O1s spectrum obtained from a film with a coverage less than one monolayer, deposited at low temperatures with no co-adsorbate contributing to the photoemission spectrum.

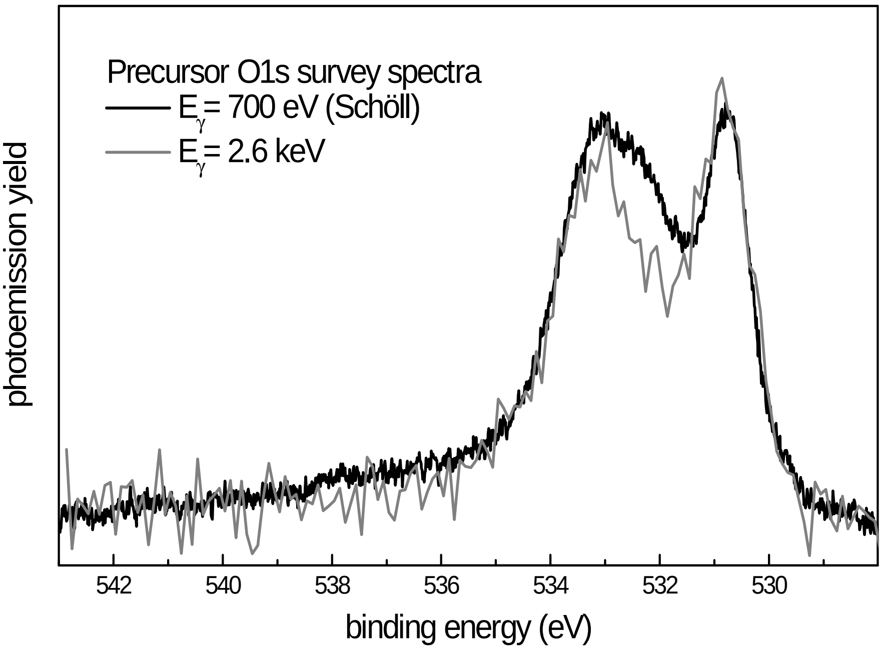

Figure 5.2: *Comparison of the photoemission spectra of the PTCDA precursor state taken in this work during beamtime N'03 (grey) and by Schöll (black) [Sch 05a]. In the black curve, the unresolved peak at* 533 eV *is more intense than in the grey curve. This peak partially originates from water, condensed on the sample. The background was subtracted from both spectra in the way as described in chapter 5.3.1.*

As for the monolayer, the O1s-PE survey spectra measured on the precursor within this work are compared to spectra from other measurements on the same system. Other high resolution O1s-survey spectra on the precursor were measured by Schöll. He took the data approximately 20 minutes after preparation. It can be assumed that those spectra correspond to the intrinsic precursor. In comparison with the high resolution O1s-photoemission spectra taken by Achim Schöll, the high resolution O1s spectra of the beamtime N'03 exhibit a similar shape [Sch 03]. In spectra which he took later, he finds an increasing peak with time due to water adsorption. In the spectra from beamtime N'03 of the present work, this feature (at approximately 533 eV binding energy) has even a smaller contribution to the spectrum. Therefore, not much water could have been adsorbed on the PTCDA film investigated during beamtime N'03 (figure 5.2). No modification with time was observed for the subsequent O1s survey spectra of this preparation. Therefore these spectra can be assumed to correspond to the intrinsic precursor spectra.

Schöll took his data with a photon energy of 700 eV, in our data we used 2.6 keV, so the cross section of x-ray absorption in our data is much smaller, nevertheless the statistic in our data is good due to the long counting times.

5.3.1 Background

In all O1s PE-spectra of the standing wave experiment, a background had to be subtracted in order to obtain the NIXSW profiles. This had to be done very carefully, because an incorrect subtracted background can influence the result. Therefore, a model has to be developed in order to subtract the unwanted background contributions. The background subtraction is discussed in more detail in appendix E.

For comparison of the O1s photoemission spectra taken by Schöll with our spectra, the background was subtracted here in the way Schöll used (see figure 5.2, and 5.3). For the evaluation of the PE spectra across the standing wave, the best "model" for the background, however, appeared to be a slightly modified model. Each model will be described in the following.

- background subtraction proposed by Schöll

The O1s precursor spectra exhibit a slanting background which was fitted with a straight line. The slope was adapted to the background on the low binding energy side. After subtracting this line, a clear Shirley-type background was left, which was subtracted, too. Applying this background subtraction to the spectra taken by Schöll and to our survey data (off-Bragg-energy), the peak profiles became well comparable, as demonstrated in figure 5.2.

- modified background model

The statistics of the photoemission spectra taken in a standing wave experiment is not as good as in most of the survey spectra. To approximate the above described background subtraction of Schöll, the fit was done in one step with a linear fit and an additional broad Gaussian peak, which approximates the Shirley background, at a fixed position and a fixed FWHM. This model appeared to be the best approach for the background, because the stoichiometry for the two distinct oxygen types was reproduced very well in a subsequent fit of the survey spectrum (2:1 - carboxylic O : anhydride O - with no constraints). Also the difference of these two models (see figure 5.3) is small compared to the remaining O1s spectrum.

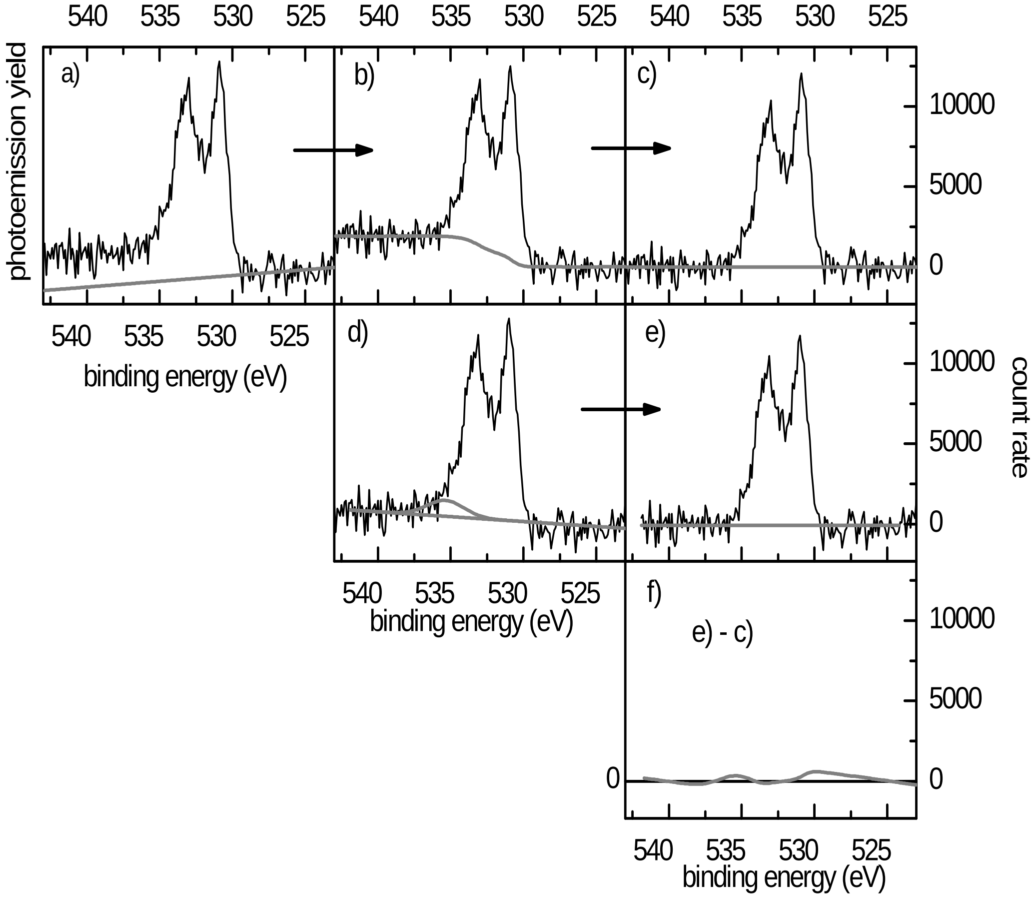

Figure 5.3: *a) - c) Background subtraction of the O1s photoemission spectra the way Schöll proposed. d) - e) For the background subtraction of the PE spectra applied in the present work the model from Schöll was modified. This was done, because the counting statistics in the PE spectra taken at excitation energies close to the Bragg condition was not as good as in the here presented survey spectrum. f) Difference obtained from the two ways of background subtraction. The y-scale is identical to the scales of c) and e), respectively. The difference amounts to ca.* 4% *of the total O1s spectrum.*

5.3.2 Photon-stimulated desorption

At the end of beamtime N'03 the O1s photoemission spectra of the precursor exhibited a significant change in their shape. The first guess for this change was a beam damage. This was investigated in beamtime N'04. However, it appeared not to be a beam damage, but the so-called photon-stimulated desorption (PSD) of water.

The sample was cooled down to less than 100 K, and water adsorption occurred. The oxygen atoms of the water occupied different adsorption sites than the atoms of the investigated PTCDA molecule. Also their chemical bonding is different. Therefore, depending on the amount of adsorbed water (i.e. how long the sample was cooled), the photoemission spectra looked different and the results from the evaluation of the NIXSW scans were different, too.

The questions were, why did the photoemission spectra of N'03 not show any difference with time during the first 24 hours measuring, and why did no spectrum of beamtime N'04 looked like the other? The reason for this can be found in the PSD of water. In N'03 the film was investigated with the x-rays shortly after its preparation. Therefore, not much water adsorption could have been occurred by that time. Due to the high energy of the x-rays (2.6 keV), used in this experiment, photon-stimulated desorption of the water was induced by the beam. The water adsorbed on this film was directly desorbed by the beam. In beamtime N'03 the sample was not moved relatively to the beam and in the corresponding spectra no contribution of water was observed. However in beamtime N'04 the sample was moved relative to the beam a couple of times, and strong changes within these spectra were observed due to water adsorption and desorption.

Molecules, adsorbed on surfaces, can be desorbed by irradiating the surface with electromagnetic radiation. The PSD mechanism can have different origins. It can originate from light induced chemical reactions of the adsorbed molecule, from surmounting the adsorption energy as a result of excitation of molecular vibrations (physisorbed molecules), or from light induced electron transfer processes of the adsorbate and the surface [Gre 98]. It is not clear which of the three processes is the dominant one for the system under investigation, namely water on Ag(111) at 100 K. Several models for the photon-stimulated desorption (PSD) process of water on metal surfaces are discussed in literature [Mar 94] [Hsi 01] [Grö 94].

In figure 5.4 (top), the photodesorption can clearly be seen. First, the spectrum drawn in grey was measured. Nine hours later the spectrum shown with the black curve was measured. The spot of the beam on the sample was not changed between this two measurements. The spectra are normalized to the beam intensity (meshI_0). In the fresh spectrum (grey), the main peak is at lower kinetic energy with a shoulder at higher kinetic energies. After six hours of photon-stimulated desorption, this shoulder turned out to be the main peak, with its position moved to slightly higher kinetic energy. The water was desorbed under the influence of the beam, and with time, the O1s spectrum loses in intensity. Also the shape changes. Presumably, multilayers of water covered the thin film of PTCDA on the sample. By desorbing the water with the beam, the spectrum of the PTCDA precursor is obtained with time. Unfortunately, in the O1s data from beamtime N'04, no intrinsic PTCDA precursor spectrum was taken. All spectra exhibit a composition of the contributions from the PTCDA and from the water.

The contamination by water can also nicely be seen in figure 5.4. During defrosting the sample, the spectra change continuously with increasing temperature. At low temperatures, the spectra show the contamination by water. By warming up the sample to room temperature, the shape of the spectra changes to that of the intrinsic monolayer spectrum at room temperature.

Only in N'03, the intrinsic precursor spectrum was obtained directly after preparation. It exhibits no changes with the x-ray beam which continuously illuminated the same spot on the sample. Besides, comparing it with the spectra taken by Schöll very shortly after preparation, it shows no significant difference in shape.

Therefore, the results presented for the precursor phase correspond to the data obtained in beamtime N'03.

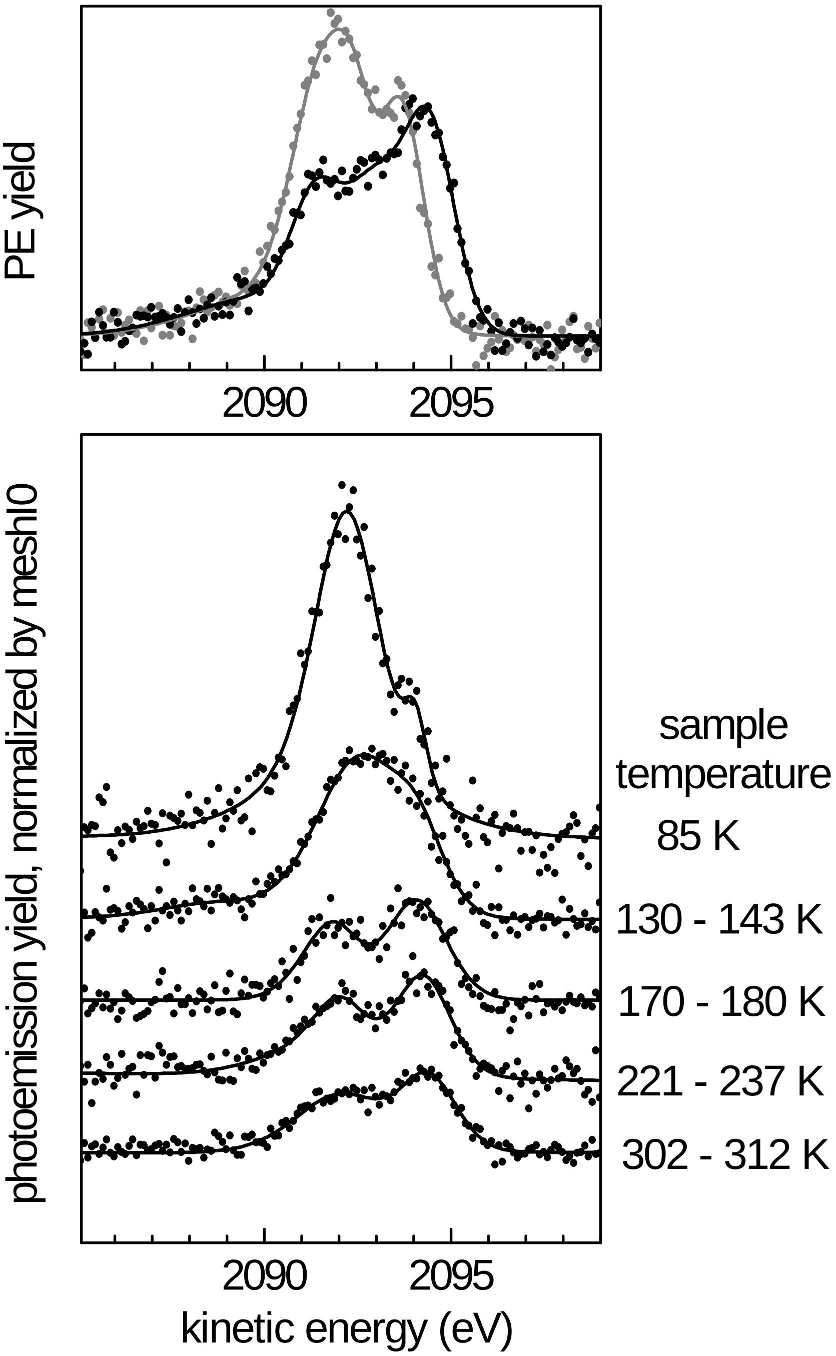

Figure 5.4: *Top: Photon stimulated desorption: O1s photoemission spectra taken at different times (P_151, P_154). Eleven hours after preparation, the spectrum, presented in grey, was taken. This was the first time this spot on the sample was irradiated by x-rays. On the same spot, nine hours later (with six hours x-ray exposure), another spectrum, represented with the black curve, was taken. Below: Photoemission spectra during the defrosting of the sample, contaminated with water. At room temperature, the typical PTCDA monolayer O1s spectrum is obtained. The water was desorbed. The spectra are normalized by the beam intensity (meshI0).*

5.3.3 Total oxygen

As discussed above, only the data taken in beamtime N'03 could be used for the evaluation of the vertical bonding distance of the oxygen atoms. Only those spectra correspond to the intrinsic precursor, all other low temperature spectra exhibit contamination with water. In figure 5.10 (in section 5.4 on page 124) on the left, the total oxygen NIXSW profiles are presented for the high resolution data. In table 5.3, the values for the coherent position and coherent fraction are listed for the low and high resolution data.

precursor O1s total results
preparation N'03, 0.3 monolayer coverage

first period (beam exposure 5 – 8 h)
(low resolution)

spectra	C_F	$C_{P\ \mathrm{eff}}$	$C_{P\ \mathrm{eff}}$(Å)
4	0.466 ± 0.046	0.135 ± 0.009	2.667 ± 0.021

second period (beam exposure 18 – 24.5 h)
(high resolution)

spectra	C_F	$C_{P\ \mathrm{eff}}$	$C_{P\ \mathrm{eff}}$(Å)
2 (+2 merged)	0.230 ± 0.079	0.086 ± 0.014	2.553 ± 0.032
2 (+2 merged) ($O_{\mathrm{carbox.}}$+$O_{\mathrm{anhyd.}}$)	*0.390 ± 0.061*	*0.109 ± 0.006*	*2.606 ± 0.014*

Table 5.3: *Fitting results for the O1s NIXSW data. The results were averaged from the results taken on the precursor film with a beam exposure of 5 to 8 hours (first period) and on a precursor film with a beam exposure of 18 to 24.5 hours (second period). The column "spectra" denotes the number of evaluated spectra. The errors correspond to the standard deviation of the results for the different NIXSW scans. The results obtained in the second period are given for the evaluation of the NIXSW profiles for the total oxygen and additionally for the evaluation of the sum of the NIXSW profiles obtained from the fitted electron yields for the carboxylic and anhydride oxygen. In the latter result the additionally observed oxygen contribution is subtracted from the total oxygen signal (see text).*

In the PE spectra of the XSW scan measured in the second period of beamtime N'03, a new feature occurred in the spectra. It was possible to deduce an Argand vector for this feature (see the section 5.4). This additional oxygen vector occupies an opposite position to the total oxygen vector in the Argand diagram. For the total oxygen result, the coherent fraction is lowered due to this "opposite" contribution with the high coherent fraction of one.

The evaluation of the sum of the NIXSW profiles for the carboxylic and the anhydride oxygen yields a higher coherent fraction and a different value for the coherent position, which also is given in table 5.3 for the second period results. The observed additional vector did not occur in the PE spectra of the first period. It was detected as a third component with PCA in the XSW PE spectra of the second period, however, it was not found in the data of the first period. Only two components were found with PCA there.

Two different vectors for the oxygen are shown in the Argand diagram of figure 5.5. One vector represents the result obtained with a pass energy of 47.0 eV (low resolution) which was measured in the first period. The other vector shows the result where the additional oxygen vector was subtracted, it was obtained with the pass energy of 23.5 eV (high resolution) in the second period. In order to obtain the latter results, the 16 point spectra were merged in the four point spectra for the evaluation, as it was done for the monolayer.

Correcting the vector of the second period, as it was done for the monolayer spectra (see chapter 4.5.4) with a contribution of a bulk like vector of 10%, the value of the coherent position rises to the value obtained in the first period. This correction was introduced here, because the observed changes in the results were assumed to be due to PTCDA molecules which were migrated to step edges. On these steps the molecules are assumed to stand upright, as it is observed for the monolayer with STM [Glö 98]. The value of 10% seems to be a good approximation for the fraction of molecules decorating step edges on bulk position, because with this correction the same values as obtained for the first period were obtained.

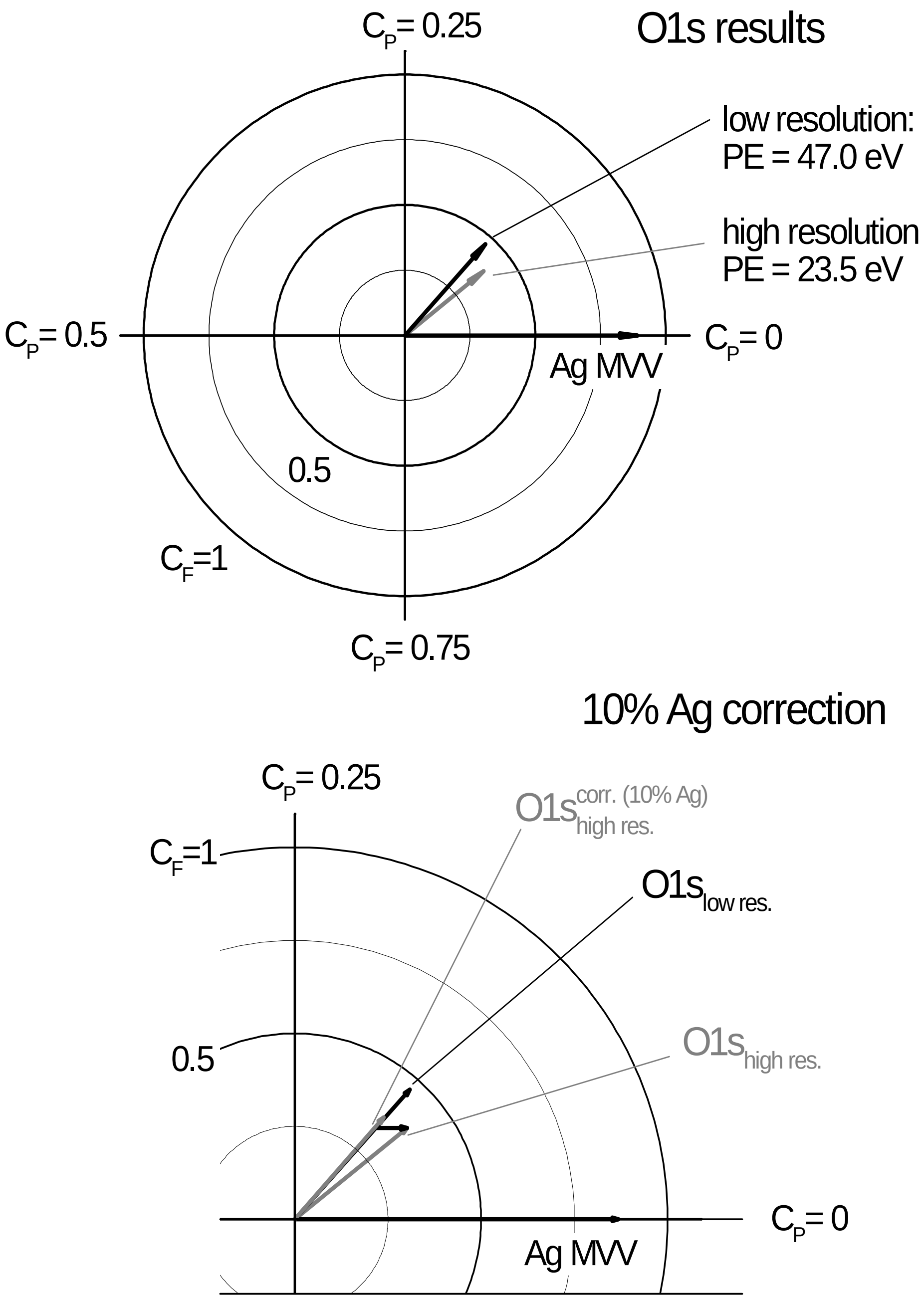

Figure 5.5: *Argand diagram for the precursor results. Top: Resulting vectors of the distinct NIXSW experiments with different pass energy of the electron analyzer. The low resolution data were measured in the first period and the high resolution data in the second period. The presented high resolution vector corresponds the oxygen result without the observed additional oxygen contribution. Below: The correction of the high resolution vector with a bulk like contribution of 10 % gives the same vector position as for the low resolution data.*

5.4 Fitting model for the carboxylic and anhydride oxygen

In the following section the fitting model for the differential fit of the O1s-PE spectra will be presented.

Schöll determined for the precursor O1s spectra five peak contributions by comparing the high resolution x-ray photoelectron spectra of NTCDA (1,8-naphtalene-dicarboxylic acid anhydride) and PTCDA at different temperatures on silver(111) [Sch 03]. This and many other models were tested on the PE spectra of the standing wave scan, as it was done for the monolayer data. It appeared that the model, proposed by Schöll, gave the best accordance to the data and was used in this evaluation, too.

Two peaks were found to be due to the carboxylic oxygen, one main peak and a shake up satellite. For the anhydride oxygen, also one main peak and one shake up satellite could be identified in the spectrum. At slightly higher binding energy (at 537 eV binding energy, 6.3 eV higher compared to the main carboxylic oxygen peak in binding energy), another shake up satellite was found by Schöll. He leads it back to satellite contributions from both oxygen types. This contribution is less than 4 %. Due to the poor statistic in the NIXSW scan, this peak could not be separated in the spectra of the present work.

As for the photoemission lines of the monolayer phase, pure Gaussian profiles were used to fit the low temperature data. A Lorentzian contribution, due to life time broadening of the core states, could not be observed in this data, because of the finite resolution of the electron analyzer in the experiment.

The fitting was done with the program *CasaXPS*. The background (see chapter 5.3.1) and the derived peaks were fitted to the survey spectrum in one step. The survey data were taken far off the Bragg energy for the substrate. For the four main peaks the positions and FWHM were constrained to the values Schöll had found. In the fit with free areas for all peaks, the area ratio for the carboxylic and the anhydride peaks came out to be 2.00 : 1.07, which is in very good agreement with the stoichiometry of the molecule (figure 5.6).

Surprisingly, the photoemission spectra taken within standing wave photon energies exhibit a new feature. It was reproduced in several measurements, so that instabilities of the monochromator were excluded to be the reason. In figure 5.6 (center) an on-Bragg photoemission spectrum is shown with the off-Bragg fitting of the described model. In the residuals at the binding energy of 530.0 eV, this new feature clearly can be seen.

PCA

Three principal components were found by applying the principal component analysis to the high resolution data of the second period. The third principal component corresponds to this new feature. So it can be assumed, that there are at least three different vertical positions of the oxygen atoms. PCA on the first period data only yield two components. This difference indicates the observed structural changes in the precursor film with time (or with beam irradiation). A short description of the PCA can be found in appendix G.

Differential results

In order to make a reasonable fit of the on-Bragg photoemission profiles the new peak was introduced 0.8 eV below to the low binding energy side of the main carboxylic peak, with a FWHM of 1.1 eV. The fitting model is presented at the bottom of figure 5.6. By applying this model to the photoemission profiles of the standing wave, the area of this peak was found to vary from 0% to nearly 20%. In figure 5.7, the photoemission spectra of the standing wave are shown, including the fit with the new model. Another model with an additional peak at the position of 533 eV binding energy (identified by Schöll as oxygen coming from water molecules) with various FWHM even improves the fit quality (smaller residuals), but this additional feature mixes up with the carboxylic and anhydride peaks, the fit becomes "unstable". Hence, the NIXSW-profiles become meaningless and cannot be fitted anymore. In the following, this peak was neglected for the fitting procedure.

Due to different atomic positions, only the area ratio of the different components changes in the standing wave. Therefore, the peaks were constrained in their positions, in the FWHM and in the ratio of the main peak to the corresponding shake-up peak.

The fitting parameters are shown in table 5.4.

fitting parameter for the O1s precursor spectra

	Position (relative to the caboxylic)	FWHM	area (off Bragg)
carboxylic	0 eV (BE 530.84 eV)	1.139 eV	36%
carboxylic satellite	+1.46 eV	1.505 eV	29%
anhydride	+2.52 eV	1.139 eV	23%
anhydride satellite	+3.28 eV	1.724 eV	12%
new oxygen peak	−0.80 eV	1.1 eV	−−

Table 5.4: *Fit results for the energy positions, linewidths and relative intensities of the main and satellite peaks in the O1s precursor spectrum. The sum of the carboxylic and anhydride peak areas corresponds to 100 percent. The new additional peak has a contribution of 3.9 percent to the total area of the oxygen PE spectrum.*

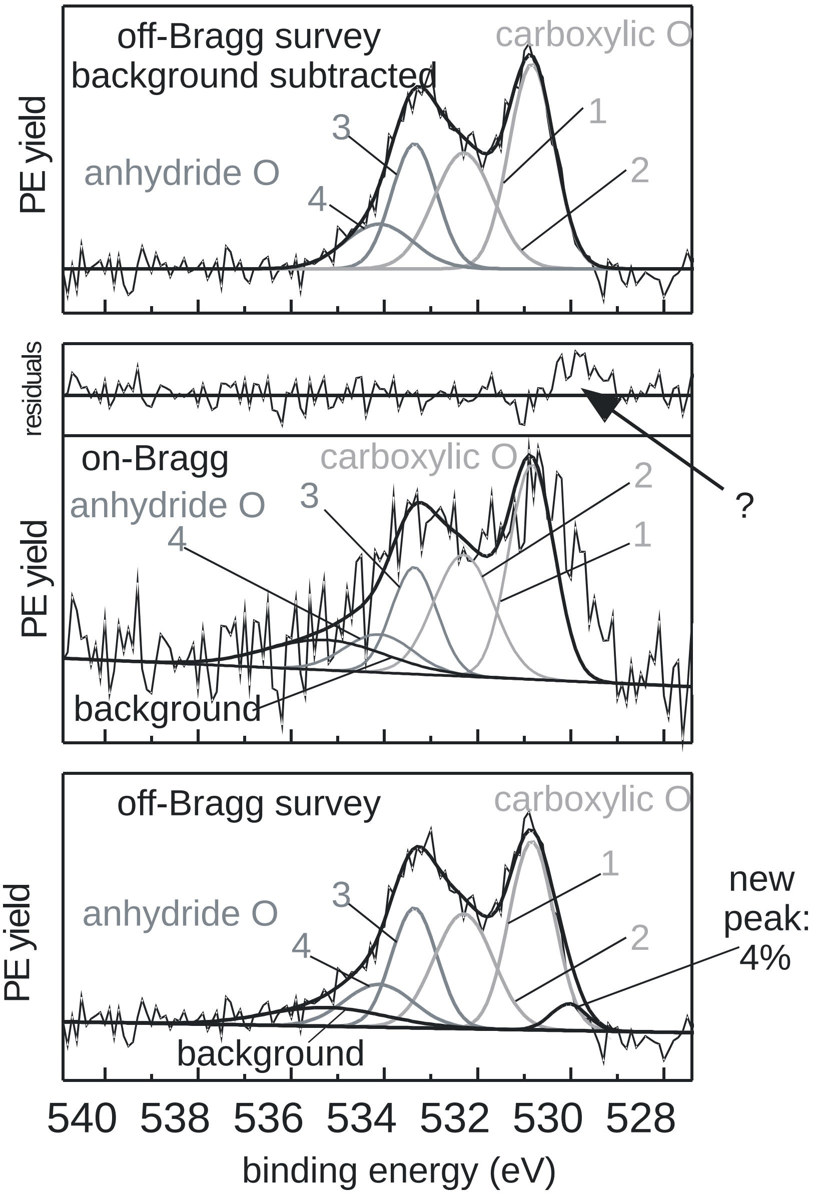

Figure 5.6: *O1s-high resolution PE spectra of the precursor. Peak 1 and 2 correspond to the carboxylic oxygen, peak 3 and 4 to the anhydride oxygen. The peak-area ratio for the carboxylic to the anhydride oxygen is 2:1. Top: survey spectrum taken at a photon energy of* $E = 2.618\,\mathrm{keV}$*. The background was subtracted in the way Schöll proposed. Also the peak model of Schöll was applied. Center: PE spectrum taken at the "on-Bragg" photon energy of* $2635.4\,\mathrm{eV}$*. The fitting profile, deduced from the survey spectrum at off-Bragg photon energy does not yield to a satisfying fit result. A new structure at a binding energy around* $530.0\,\mathrm{eV}$ *appears. This can be clearly seen in the residuals of the fit. Bottom: modified fitting model for the off-Bragg spectrum (*$E = 2.618\,\mathrm{keV}$*). Here the background was treated with the modified model from Schöll, as described in section 5.3.1. This model was used for the evaluation of the PE spectra taken at photon energies close to the Bragg condition. A new peak feature was introduced with approximately 4% of the total PE yield for the oxygen.*

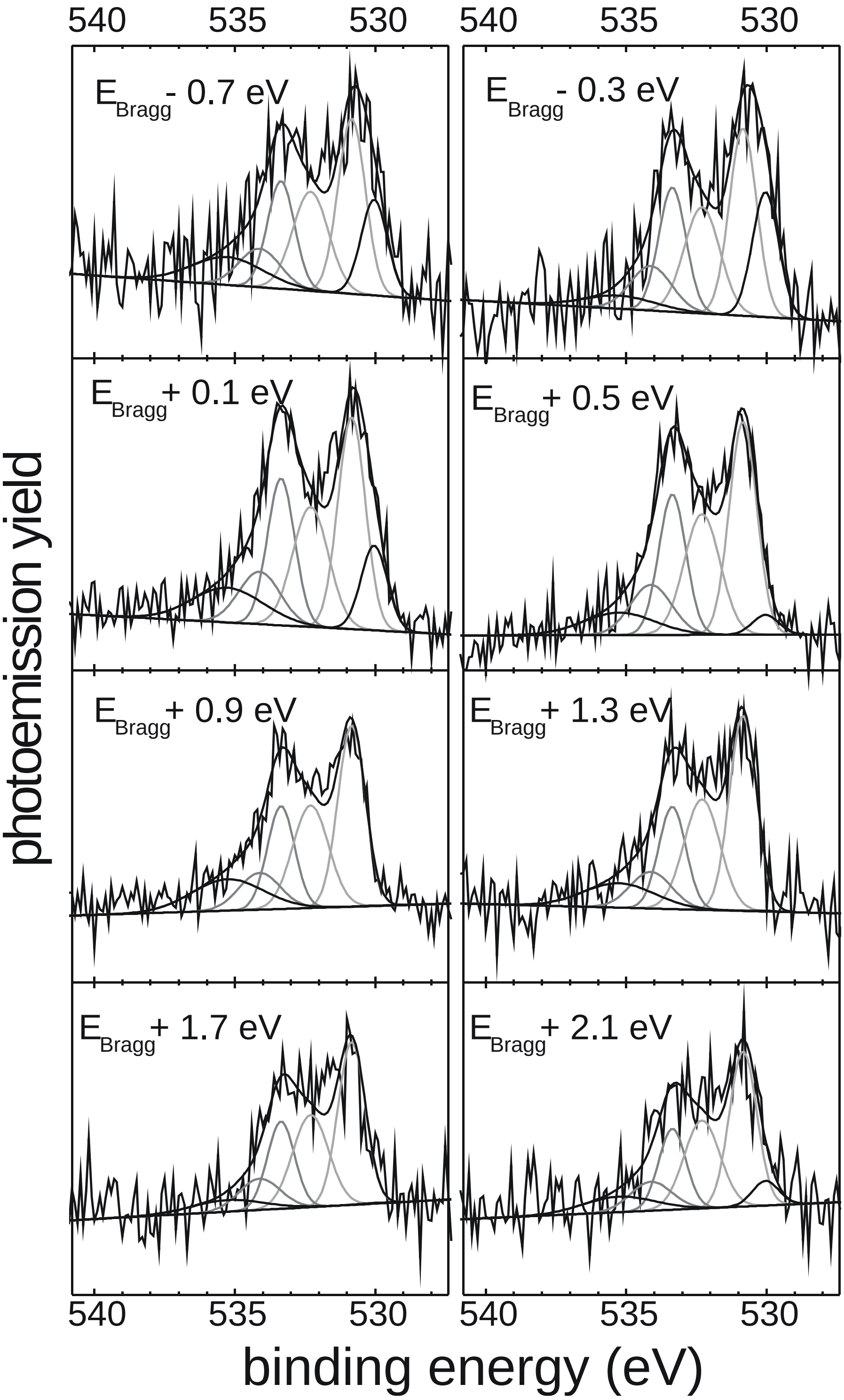

Figure 5.7: *O1s-photoemission spectra taken at an excitation energies close to the Ag(111) Bragg condition. Fitting was done with the model proposed by Schöll [Sch 03] plus an additional peak* 0.8 eV *below the main carboxylic peak. The relative intensities of the peak doublets for the carboxylic and anhydride oxygen exhibit a clearly variation at excitation energies around the Bragg condition. As well the additional oxygen feature at* 530 eV *exhibits a differential variation in the spectra.*

Merged spectra

As for the monolayer, the high resolution data were taken in two steps, in order to avoid the loss of spectra due to experimental / instrumental failure. Two NIXSW scans with 16 points each were taken very close to the Bragg energy. Two more scans with only 4 points each consisting of 2 points close to Bragg energy and 2 points far off the Bragg energy were taken afterwards.

The 4-point reflectivity curve was normalized to the 16-point reflectivity curve[1]. Then the NIXSW-profiles were normalized in the same way. So the 16-point profile could be inserted in the 4-point profile. The normalization of the reflectivity curves is shown in figure 5.8.

The fitting results of the high resolution O1s NIXSW profiles are shown in figure 5.9 and 5.10. The 16-point spectra were again merged in the 4- point spectra. As can be seen, there is no significant difference in the results if either the 4-point spectrum PT1_145 or PT1_146 was used to complement the scan PT1_144. This demonstrates that the merging of the spectra can be performed reliable.

The statistic of the XSW profile of the additionally found oxygen is low, therefore, the fit of its profile is not very good, as can be seen in figure 5.10. The reason for such a low statistic is its small contribution of less than 5% to the total oxygen peak. The other peaks dominate the spectra, and only in the XPS spectra very close to the Bragg energy, its contribution to the total spectrum rises due to its particular vertical position.

The fitting results of the NIXSW profiles are given in table 5.5.

The given errors come from the statistical spread of the evaluated spectra, they correspond to the standard deviation. The Argand diagram for the precursor result is shown in figure 5.11, where the contribution of the additional oxygen nicely can be seen. From the Argand diagram, it becomes clear that such a contribution strongly lowers the value of the coherent fraction, even with a contributions of only 4% to the total spectrum. In the Argand diagram

---

[1] The reflectivity curves were normalized with the photon current (meshI0). Then the two central points were fitted to the 16-point curve by varying the intensity axis. No background was subtracted.

precursor results

a) first period results

	C_F	$C_{P\text{ eff}}$	$C_{P\text{ eff}}$(Å)
O1s total	0.466 ± 0.046	0.135 ± 0.009	2.667 ± 0.021
C1s	0.621 ± 0.063	0.193 ± 0.010	2.805 ± 0.024
Ag MVV	0.868	0.965	2.267

b) second period results

	C_F	$C_{P\text{ eff}}$	$C_{P\text{ eff}}$(Å)
O1s total	0.230 ± 0.079	0.086 ± 0.014	2.553 ± 0.032
O1s carboxylic	0.402 ± 0.046	0.063 ± 0.015	2.499 ± 0.035
O1s anhydride	0.483 ± 0.056	0.204 ± 0.018	2.831 ± 0.042
sum anh. + carb.	0.390 ± 0.061	0.109 ± 0.006	2.606 ± 0.014
O1s additional	1.000	0.652 ± 0.013	3.882 ± 0.032
O1s additional			1.532 ± 0.032
O1s additional			6.232 ± 0.032

c) second period results with 10% bulk- like correction

	C_F	$C_{P\text{ eff}}$	$C_{P\text{ eff}}$(Å)
O1s total	0.364	0.136	2.669
O1s carboxylic	0.360	0.080	2.538
O1s anhydride	0.518	0.233	2.898

Table 5.5: *Fitting results of the NIXSW profiles for the precursor. The most reliable results are obtained in the first period (a) measurements. In the second period (b), structural changes in the film were observed. The position of the additional oxygen can be either above or below the PTCDA molecule. Therefore, three distinct positions are given as result. The errors correspond to the standard deviation of the results for the different NIXSW scans. The fitting result of the coherent fraction for the additional oxygen is equal 1 for all evaluated profiles. However, due to the low statistic for this peak and due to the bad quality of these fits, the result is not very reliable. The error for the coherent fraction can be estimated at 0.3 and for the coherent position at 0.1 at least. (c) Results obtained in the second period, corrected with a bulk like contribution.*

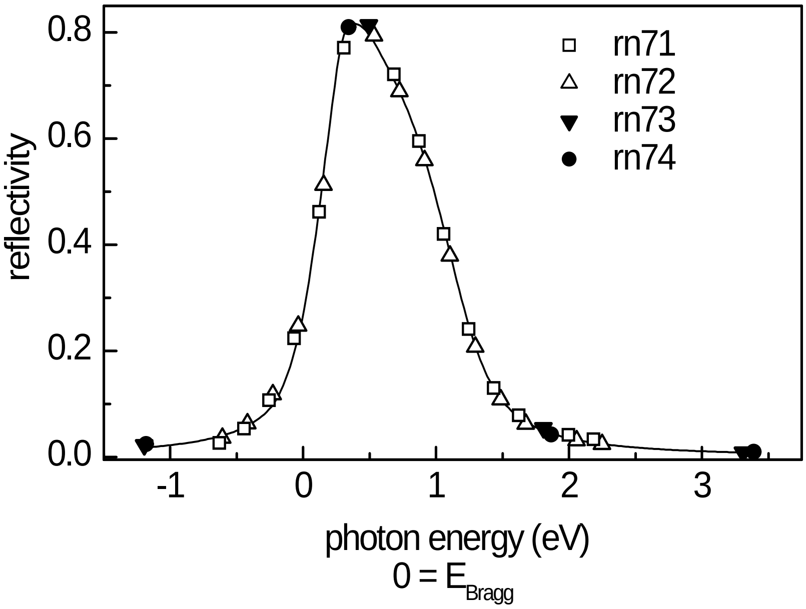

Figure 5.8: *Different normalized reflectivity curves. The solid symbols represent the two curves with the 4 data points (rn73 and rn74); the open symbols show the 16 point reflectivity curves (rn71 and rn72) that were merged into the 4 point curves. Solid line: reflectivity fit to the data with the program DARE.*

of the bottom of this figure, additionally, the vectors corrected with a bulk like contribution are shown.

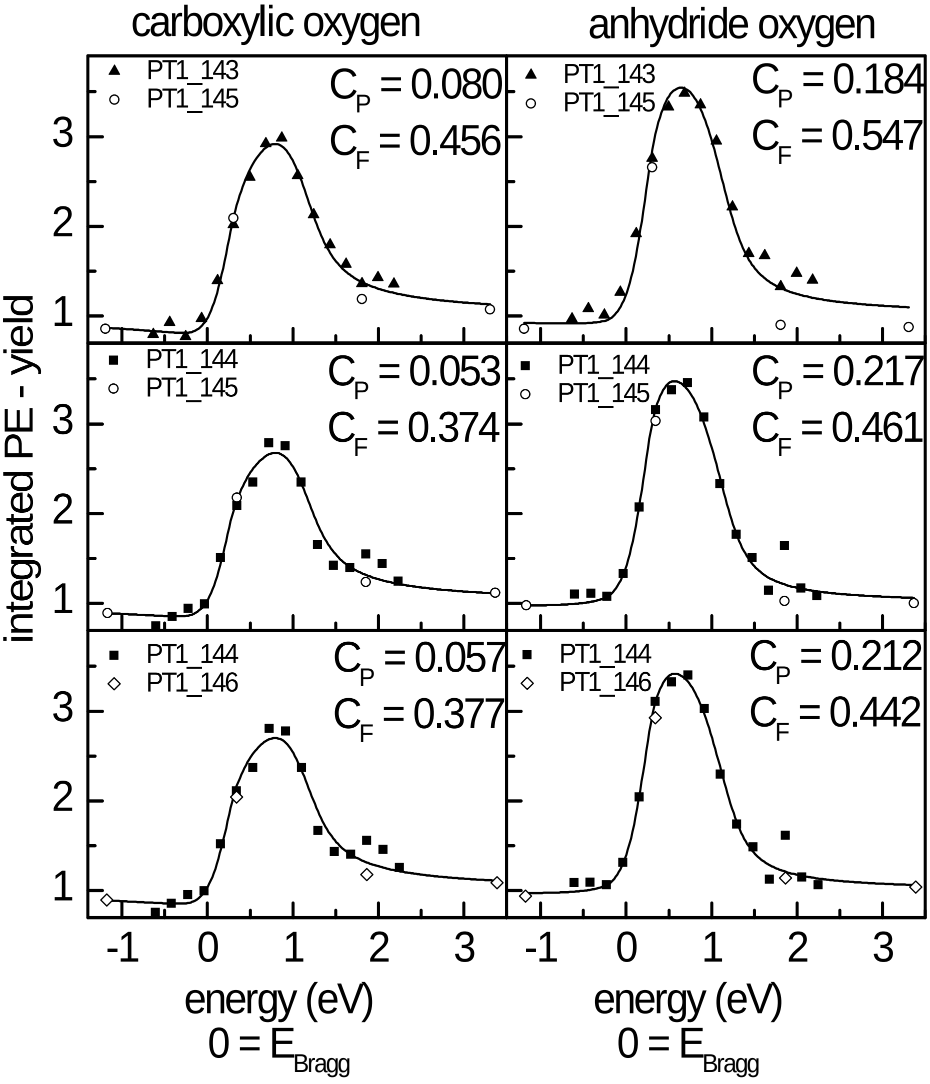

Figure 5.9: *NIXSW profiles for the carboxylic and anhydride oxygen. The 16 point NIXSW profiles (solid symbols) were merged into the 4 point NIXSW profiles (open symbols). The solid lines represent the fit of the data. The corresponding results for the coherent position and fraction are given in the figure.*

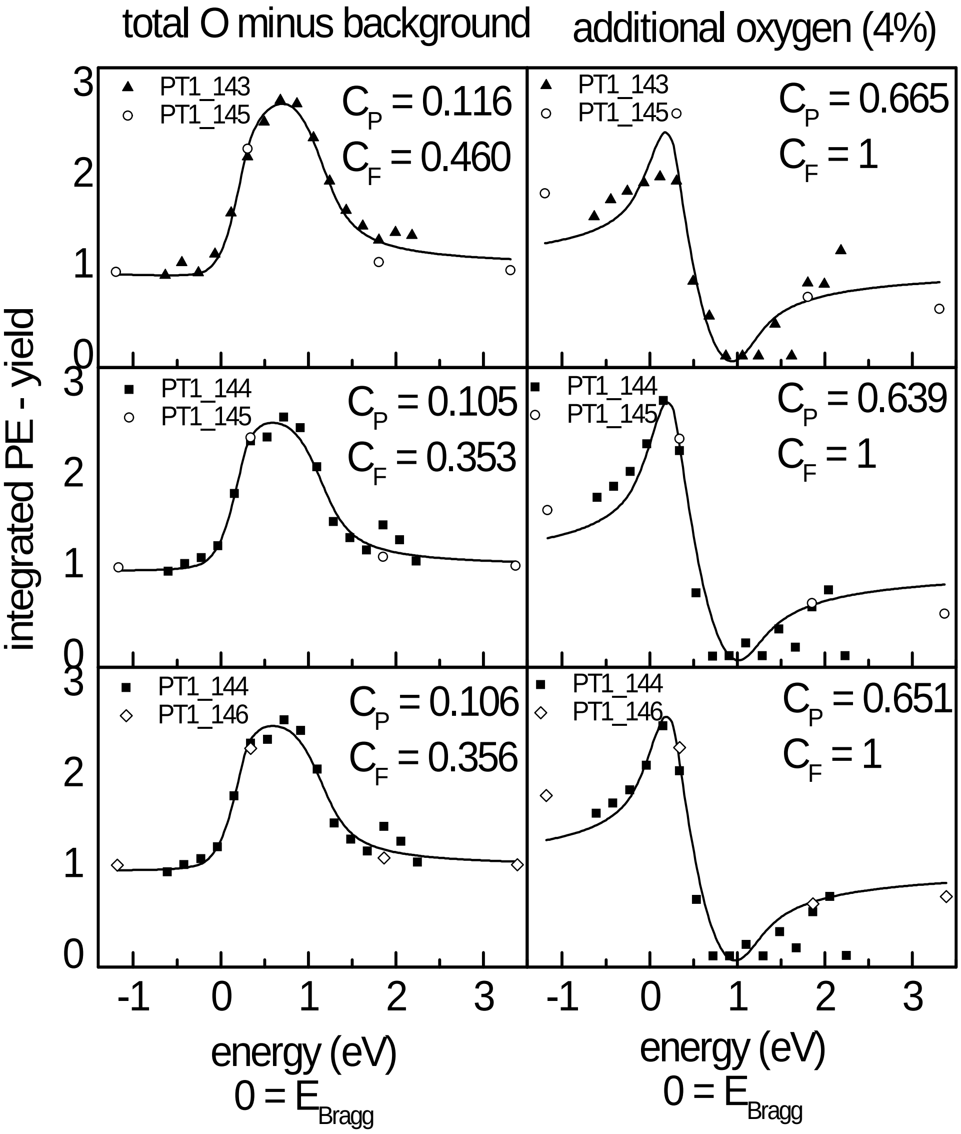

Figure 5.10: *NIXSW profiles of the total and of the additional oxygen. The 16 point NIXSW profiles (solid symbols) were merged into the 4 point NIXSW profile (open symbols). The solid lines represent the fit of the data. The corresponding results for the coherent position and fraction are given in the figure.*

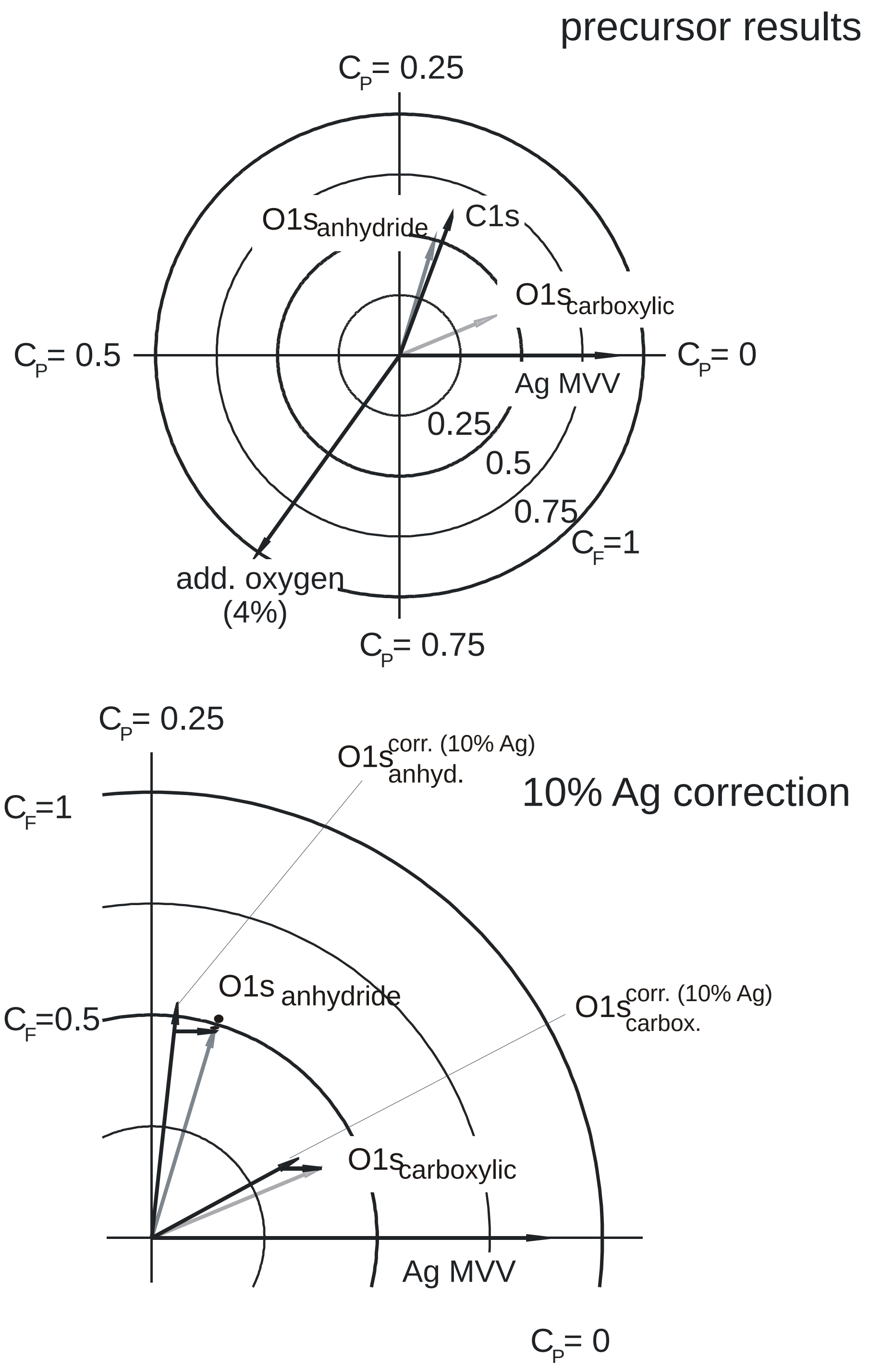

Figure 5.11: *Argand diagram for the precursor data. Top: The carbon vector was evaluated from the first period data. The oxygen vectors are obtained from the evaluation of the second period where structural changes in the precursor film occured. Bottom: The results (obtained in the second period) for the evaluated positions of the distinct oxygen types is corrected with a bulk-like contribution of 10 %.*

Additional oxygen positions

The evaluation of the additional oxygen peak in the PE spectra revealed a certain vertical position for this species on the silver surface. Remarkably, the value of the coherent fraction is equal to 1. This indicates that all atoms of this type occupy an identical adsorption place. Several suggestions for the origin of this oxygen type will be given in the following.

- CO

It could be a co-adsorbant from the residual gas, e.g. CO molecules. However, the desorption temperature for CO on Ag(111) was found to be 53 K [Han 91], therefore it is implausible that CO was co-adsorbed on the surface. Also, no additional contribution as in the oxygen spectra has been found in the carbon spectra.

- Water

The water adsorption with time was measured by Schöll. He found an increasing peak at binding energy very close to the binding energy of the anhydride oxygen. However the binding energy of the additional oxygen lies 0.80 eV below the binding energy of the carboxylic oxygen, far away from the binding energy of the water oxygen atoms. Hence, it can be excluded that this feature comes from the adsorbed water.

- Beam damage

It could be anticipated that the additional oxygen position originates from atoms split-off from the PTCDA molecules due to the high energy beam.

- Additional adsorption sites

The molecules in the precursor phase do not show long range order on the surface. They lie flat, and in some local regions a herringbone structure is found and in other a square phase [Tem 06a]. A possibility could be that an amount of molecules in a specific local arrangement occupies a particular position. Due to the binding energy of the additional oxygen in the PE spectrum, it is only possible that this feature stems from carboxylic oxygen atoms. It even has a lower binding energy than the main peak of the carboxylic oxygen. Therefore the question arises why no additional a feature is observed in the anhydride-oxygen part of the PE spectra. However, such a feature can not be excluded. It is possible, that it only cannot be observed due to the low statistic.

- On top

Another possibility could be that some PTCDA molecules are on top of other molecules, i.e. in the second layer. In the bulk, the intermolecular distance of the PTCDA molecules is 3.23 Å for the (102) planes [For 84]. The vertical distance of the molecules in precursor phase was 2.80 Å. The sum of these values gives a vertical position of 6.03 Å for the second layer molecules which is close to the found value of 6.24 Å. However, it was found that the second layer is more strongly bonded than the higher multilayers [Kil 04]. Therefore, it is not very plausible that the bonding distance for the second layer is larger than in the bulk crystal. Hence, the model with flat lying molecules in the second layer is not very reliable.

- Beam induced step edge decoration

Finally the additional position could stem from PTCDA molecules tilted with respect to the Ag(111) surface, as described for the monolayer phase on page 75, before. The assumed molecules[2] are standing upright at the step edges of the silver with their long axis parallel to the step. This is shown in figure 5.12. In contrast to the monolayer, this time two positions are necessary in order to explain the structural differences observed in the spectra. One position corresponds to upright molecules at step edges, where the oxygen

---

[2] Both models are only possible due to the intramolecular distances in the PTCDA molecules. In one anhydride group, the distance between the carboxylic oxygen atoms is 4.4 Å, and between the carboxylic oxygen atom and the anhydride oxygen atom is 2.2 Å. These distances correspond approximatley to the substrate lattice plane distance of 2.35 Å of the silver or to a multiple of it. The intramolecular distances do not exactly correspond to the substrate lattice planes, however, in a NIXSW experiment the resulting Argand vector would correspond the observed coherent positions with high values for the coherent fraction, because the difference in the positions is only small ($0.05\,\text{Å} \Rightarrow \Delta C_P = 0.05/2.35 = 0.02$).

atoms occupy a position of the bulk lattice planes, as it was described for the monolayer (10% bulk like). The other position corresponds to upright molecules where the oxygen atoms are 1.53 Å displaced with respect to the silver lattice at step edges (additional oxygen).

In the above model the contribution of the carbon in such positions can only be seen by a decrease of the value of the coherent fraction for the total carbon. This is already described on page 75 for the monolayer.

Final results for the precursor

The main result of this investigation of the precursor is that as for the monolayer the molecule is distorted. The carboxylic oxygen atoms are significantly closer to the silver surface than the rest of the molecule.

The final resulting values are listed in table 5.5.

The results corresponding to the first measuring period (a) are the most reliable results. No structural changes were observed in these data. In the data, taken in the second period (b), changes with time (or beam irradiation) were observed. These changes could be explained, if one assumes that there are two types of PTCDA molecules, which are not in the regular planar adsorption geometry. There is indication that approximately 4% of the molecules are tilted with respect to the surface and take a position 1.53 Å displaced with respect to the silver (111) lattice planes. There are also hints for the fact that another amount of approximately 10% of the molecules are tilted with respect to the surface and take in a position with the long axis on the substrate rows.

The high resolution measurements for the separation of the two oxygen types were conducted on these structurally changed films. In order to obtain the result for the flat lying molecules, a correction as described above was applied to the results.

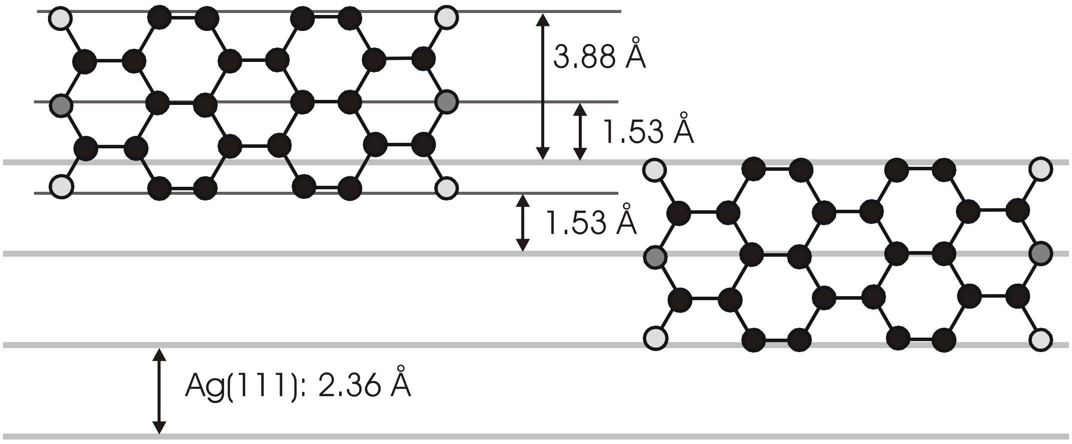

Figure 5.12: *Model of PTCDA molecules standing upright at step edges of the silver with their long axis parallel to the step. The light grey lines represent the silver lattice planes with a distance of* 2.35 Å *(at low temperatures). In order to explain the experimental data, two different positions are necessary in this model. Top left: The additional oxygen position can be explained with this model where approximately* 4% *of the molecules take in the evaluated position. The dark grey lines represent the oxygen atom positions which are* 1.53 Å *displaced with respect to the substrate lattice planes. Right: This model explains the* 10% *bulk like structural changes in the O1s precursor data. As for the monolayer, the molecules occupy adsorption sites with the oxygen atoms positioned on identical vertical positions as the substrate lattice planes.*

Chapter 6

Comparison and discussion of the experimental results – monolayer versus precursor

In this chapter, a comparison of the experimental results, obtained within this work, for the monolayer and the precursor phases is given. The nature of the bonding state for both systems is of important interest. By comparing the NIXSW results of the two phases some new conclusions can be drawn, as will be seen in the following discussion.

6.1 Comparison of the PE-survey spectra

In figure 6.1 the PE spectra of the C1s and O1s transitions for both phases are shown. The excitation energy E_γ was at least $10\,\text{eV}$ below the Bragg energy. The energy axes were calibrated with the high resolution PE spectra measured by Schöll [Sch 05a]. For the O1s spectra the energy resolution is comparable to the resolution Schöll used in his experiments. For the C1s spectra, however, the energy resolution of the present work is considerably lower.

Due to the low resolution, the shapes of the C1s spectra, measured in this work, exhibit no apparent differences for the two phases. Only a small shift can be observed in binding energies of the main peaks. This is in contrast to the PE results of Schöll. He observed significant differences in the C1s spectra of the two phases. In his data, the main peak feature is slightly shifted to higher binding energies for the precursor and the satellites are located on completely different positions [Sch 03]. In the present data these satellites are not resolved due to the employed (low) analyzer resolution. This resolution was used because of the higher count rates for the spectra. The acquisition time for such a NIXSW scan is much shorter compared to that of the high resolution scans.

The difference in binding energies and the shift of the satellite positions indicate a complete different bonding state for the two phases [Sch 05a].

As for the carbon PE spectra, the shapes of the PE spectra of the O1s transition are different for the two phases, too. This can be seen in figure 6.1 on the right.

The minimum between the two peaks is more pronounced in the spectrum of the monolayer. Furthermore, the peak feature at higher binding energies (corresponding mainly to the anhydride oxygen) is broader. From peak fitting of the main carboxylic and anhydride oxygen peaks, it is found that the FWHMs are different for the two phases. In the previous chapters (chapter 4 and 5) the fitting models for the photoemission spectra have been presented. In these, the FWHM of the main carboxylic and anhydride peaks have the values of 1.30 eV for the monolayer and 1.14 eV for the precursor, respectively. These values should be identical due to the same origin of the peaks and the identical experimental setup. However, the reason for this difference could be the limited energy resolution of the analyzer and the much lower statistics of the precursor data. Therefore, it is reasonable that the intrinsic FWHMs are equal in their value and the observed differences are only due to experimental limitations

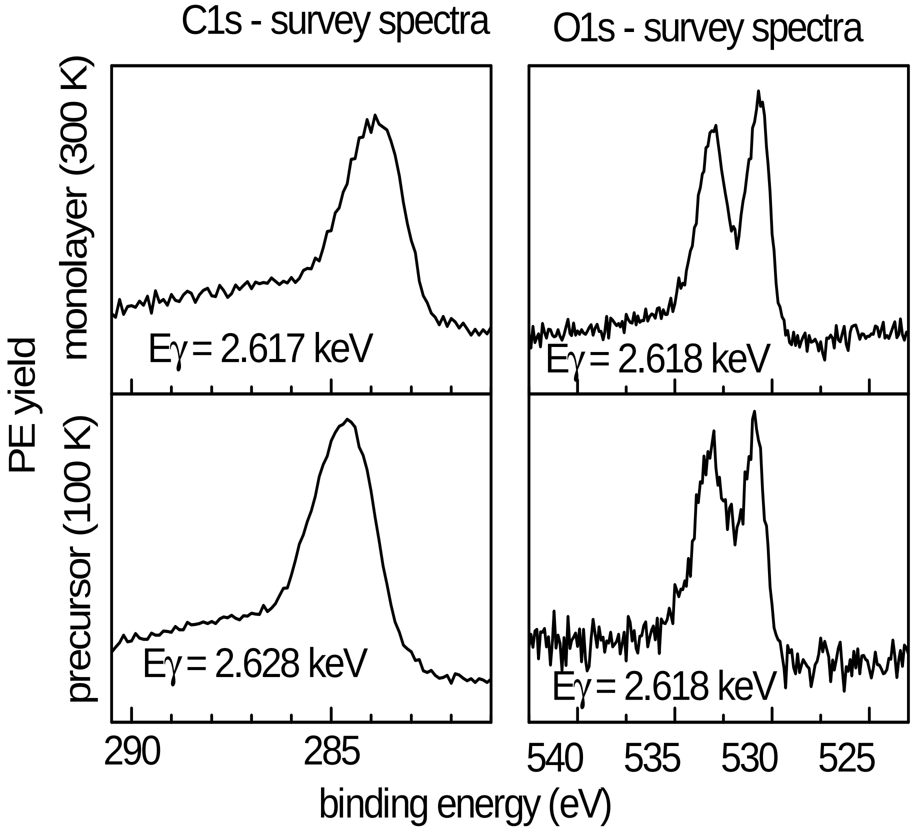

Figure 6.1: *Left: PE - C1s survey spectra of the monolayer and the precursor phase. Right: PE - O1s survey spectra of the monolayer and the precursor phase. All spectra were taken with an "off-Bragg" excitation energy. The precursor coverage corresponds to 30% of a monolayer coverage. The energy axes were calibrated with the PE spectra from Schöll [Sch 05a].*

6.2 Comparison of the fitting models for the O1s-PE spectra

The fitting models of the O1s spectra are prerequisite for the structural results of the different oxygen types in the PTCDA molecules. As reported in chapter 4, distinct fitting models on the same data set yield different results. Here, the final fitting models are presented for the monolayer and for the precursor phase.

In figure 6.2 the final models for the O1s spectra of the two phases are shown. The difference in the positions and FWHM of the carboxylic (peaks numbered with 2 in the figure) and anhydride (peaks numbered with 4) oxygen satellites is striking.

These so called shake-up satellites can be attributed to excitation processes, where a core hole is created and a valence electron excited to a higher state. This process is considered to be so fast that no significant changes of the inital-state wave functions occur on this time scale (so-called sudden approximation). Two holes are created, but only one photo-electron is emitted (2-hole-one-particle state - 2hp) [FreBig 87].

In the monolayer spectrum the shake-up satellite peaks are much broader (nearly three times for the carboxylic satellite, and four times broader for the anhydride) than in the precursor spectrum. The peak area ratio of the main peak to the satellite is very similar for the anhydride oxygen: 1 : 0.57 for the monolayer and 1 : 0.52 for the precursor. For the carboxylic oxygen this ratio is 1 : 1.06 for the monolayer and 1 : 0.80 for the precursor.

In particular this means for the monolayer phase that the satellite intensity deduced by the fitting model is larger than the main PE peak intensity. (One should note that in the multilayer PE spectra of PTCDA on Ag(111), no shake-up satellite for the carboxylic oxygen is observed [Sch 04]). The relatively large shake-up satellite in both phases indicates a good screening of the core hole [FreBig 87].

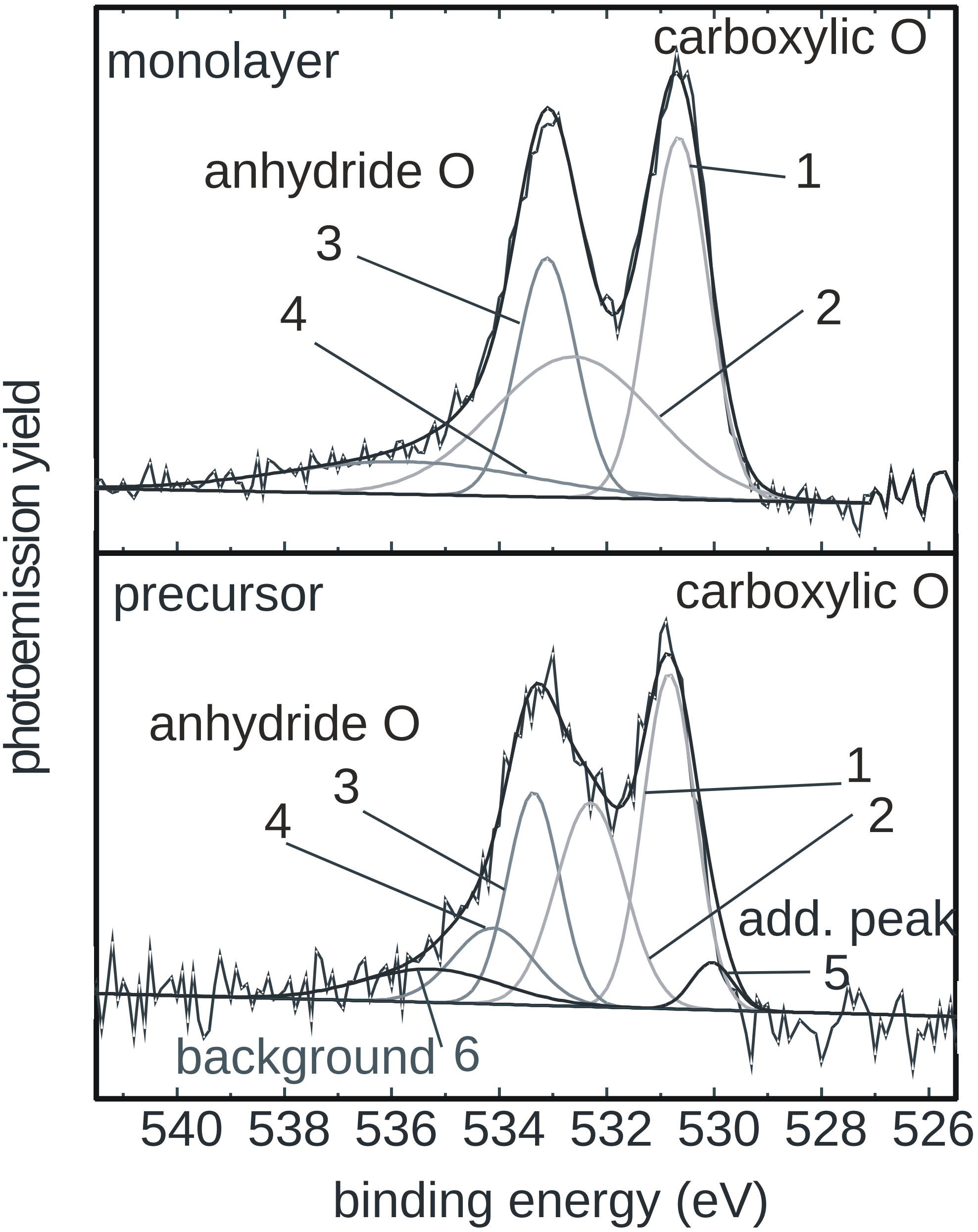

Figure 6.2: *Comparison of the fitting models for the photoelectric O1s transition of the monolayer (top) and the precursor phase (bottom), respectively. Both spectra were taken with an off-Bragg photon energy of* $E_\gamma = 2.618\,\mathrm{keV}$. *Peak 1 and 2 correspond to the carboxylic oxygen, peak 3 and 4 to the anhydride oxygen. Peak 5 is attributed to an additional oxygen, only observed in the precursor data. Peak 6 corresponds to the background signal in the precursor data. For the monolayer, the shake-up features are much broader than for the precursor. In the monolayer spectrum the intensity of the satellite carboxylic peak (2) is higher than the intensity of the main carboxylic peak (1).*

6.3 Comparison of the NIXSW results

In table 6.1 the resulting vertical distances ($C_{P\ eff}$) and the coherent fractions (C_F) are listed for the monolayer and for the precursor, respectively. The results are divided into two groups. The first part of table 6.1 gives the structural parameters of the freshly prepared films for the monolayer and the precursor phase measured with a low resolution pass energy of the electron analyzer. For the monolayer phase it can be assumed that these are the structural parameters for the herringbone structure, as discussed in chapter 4.4. For the precursor these results are considered as the structural parameters of the *intrinsic* precursor phase as it was grown.

The second group (the rest of table 6.1) corresponds to the oxygen results where structural changes were observed due to beam damage or due to structural differences because of particular preparation conditions as discussed in chapter 4.5.3 and chapter 5.3.3. These results were measured with a high resolution pass energy of the electron analyzer.

In order to explain these structural changes, a correction was proposed in the previous chapters. This correction is based on a 10% contribution of the oxygen atoms of both sorts located on (111) lattice plane positions of the silver crystal, presumably at step edge positions.

In the following, the NIXSW results for the two phases will be presented and discussed. It has to be noted again that the given coherent positions correspond to the *effective* coherent positions (see chapter 3.3.4). Therefore, for these results, a systematic error exists, whereas its size is not clear. However, the findings and conclusions deduced from these results will not change much with the application of the appropriate value for the phase Δ of the quadrupole contribution. With the values for Δ, chosen for the evaluation of the present work, the coherent position would be calculated by

$$\begin{aligned} C_P^{O1s} &= C_{P,\mathrm{eff}} - 0.04\,\text{Å} \\ C_P^{C1s} &= C_{P,\mathrm{eff}} - 0.03\,\text{Å}. \end{aligned}$$

NIXSW results: monolayer vs. precursor

Low resolution results (freshly prepared film)

	monolayer		precursor	
	$C_{P\ \mathrm{eff}}$(Å)	C_F	$C_{P\ \mathrm{eff}}$(Å)	C_F
total C	2.86 ± 0.01	0.51 ± 0.05	2.80 ± 0.02	0.62 ± 0.06
total O	2.85 ± 0.02	0.52 ± 0.06	2.67 ± 0.02	0.47 ± 0.05

High resolution oxygen results (structurally changed)

	monolayer		precursor	
	$C_{P\ \mathrm{eff}}$(Å)	C_F	$C_{P\ \mathrm{eff}}$(Å)	C_F
total	2.80 ± 0.03	0.44 ± 0.09	2.55 ± 0.03	0.23 ± 0.08
total*			2.61 ± 0.01	0.39 ± 0.06
carboxylic	2.66 ± 0.03	0.47 ± 0.22	2.50 ± 0.04	0.40 ± 0.05
anhydride	2.98 ± 0.08	0.79 ± 0.08	2.83 ± 0.04	0.48 ± 0.06
additional			3.88 ± 0.03	1.00

High resolution oxygen results,
corrected with 10% bulk position

	monolayer		precursor	
	$C_{P\ \mathrm{eff}}$(Å)	C_F	$C_{P\ \mathrm{eff}}$(Å)	C_F
total	2.87	0.46	2.67	0.36
carboxylic	2.72	0.46	2.54	0.36
anhydride	3.02	0.89	2.90	0.52

Table 6.1: *Comparison of the NIXSW results for the monolayer and the precursor phase. The low resolution results correspond to the results of freshly prepared films. In the high resolution oxygen results, an additional oxygen contribution, depending on preparation conditions or on beam damage effects was observed. Therefore, the high resolution oxygen results are slightly different in comparison to the low resolution results. These high resolution results were corrected with an additional contribution, located on the substrate lattice planes (see text). Two results for the high resolution precursor data of the oxygen are given, total and total*. The first result corresponds to the evaluation of the total PE yield. The second result of total* corresponds to the fitting result for the sum of the carboxylic and anhydride oxygen PE yield, for which the amount of the additional oxygen was not taken into account.*

6.3.1 Carbon: Molecular distances

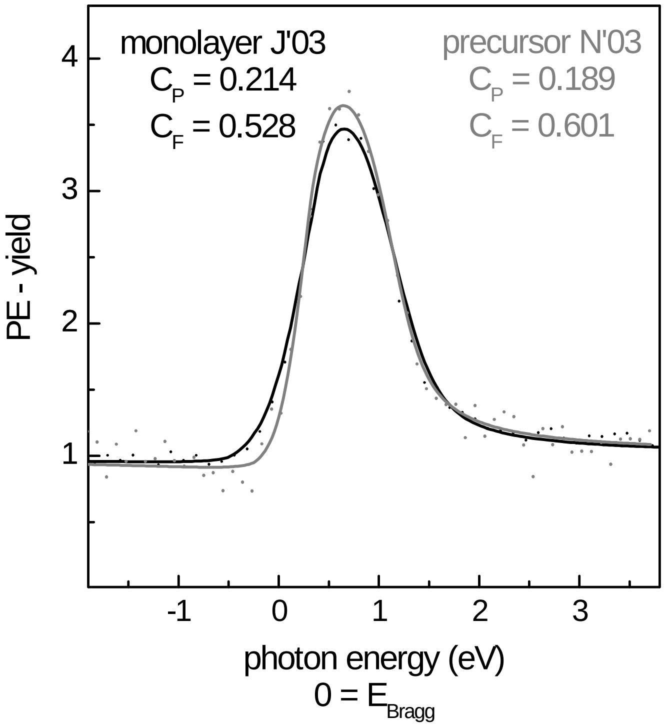

Figure 6.3: *NIXSW profiles of the C1s transition for the monolayer (black) and for the precursor phase (grey), respectively. The difference in the profiles corresponding to a height difference of* 0.6 Å *seems to be only subtle. However, in all profiles of each phase the individual shapes shown here can be found. This indicates distinct structural parameters for the two phases. The points correspond to the electron yield of the different photon energies, the solid lines to the fits to these profiles.*

The structural results for carbon are based on fit results of the NIXSW profiles. Comparing the profiles and the corresponding fits for the two phases, as shown in figure 6.3, it can be seen that the difference between the profiles is only small. However, the particular shape is similar within all profiles of each phase. From fit results, the difference in the vertical position is obtained to be $\Delta C_P = 0.024 \pm 0.004$ in units of the substrate lattice. This value lies clearly outside of the error bars. The lattice distance of the Ag(111) plane is different for the two distinct temperature phases. Taking this into account, one obtains for the difference in the coherent position a value of 0.06 Å.

The results for the carbon contain most prominently the molecular information, since the carbon is the main element in the PTCDA molecule. Therefore, one can conclude that the molecules in the precursor phase lie closer to the substrate surface than the molecules in the monolayer phase.

For an estimation of the absolute distance of the molecules from the surface, always the corresponding values for the coherent fractions have to be considered. For the two phases, the values for the carbon lie in the range of $C_F^{\text{ML-C}} = 0.51 \pm 0.05$ for the monolayer[1] (ML) and of $C_F^{\text{PC-C}} = 0.62 \pm 0.06$ for the precursor (PC). From NEXAFS measurements, it is known that in both phases the molecules are not tilted and lie flat. It arises the question why the value of the coherent fraction is not higher. One reason can be found in the uncertainty of the fitted values for the coherent fraction. As shown in the paper from Gerlach et al. [Ger 07], in the 99.7% confidence level around the minimum of the coherent fraction, the variation of the value is $\Delta C_F = \pm 0.1$! Additionally, C_F varies with the asymmetry parameter Q as shown in chapter 3.

Interestingly, the coherent fraction for the carbon is higher for the precursor than for the monolayer. If this is not attributed to the uncertainty of these values, it indicates that the molecules in the precursor phase lie closer to one plane of the same vertical distance than in the monolayer phase. However, many effects could decrease the value of the coherent fraction.

- A too high value of the asymmetry parameter Q.
- It could be an effect of different heights of the two molecules in the unit cell of the monolayer. Some indications for such an effect exist: In STM pictures of the stable monolayer phase, the two distinct molecules in the unit cell exhibit different tunneling contrasts [Glö 98] [Ere 03]. Also, the electronic structure is different for the distinct molecules within the unit cell as observed by scanning tunnelling spectroscopy (STS) experiments (Tautz et al. as noted in [Kil 07]). Furthermore, from DFT

---

[1] Reliable values for the structural parameters of the pure herringbone structure in the monolayer were estimated from the result of beamtime N'04. This was possible due to different coverages of the monolayer phase. For the C1s data a coherent fraction of $C_F = 0.59$ was obtained for the pure herringbone structure (see page 58).

calculations, different adsorption heights for the two molecule types are obtained ($\Delta C_P = 0.06\,\text{Å}$) [Roh 07]. However, the influence of such a height difference on the coherent fraction is only small. Assuming a coherent fraction of, e.g., $C_F^{\mathrm{C}} = 0.900$ for the two average carbon positions (from DFT), the resulting value for the coherent fraction would be calculated at $C_F^{\mathrm{C}} = 0.897$. This is a very small effect, it can only become stronger, if the difference in the molecular heights would be larger.

- Another possibility is the bending of the carbon core of the molecules themselves. DFT calculations indicate a small bending of the molecules [Hau 05a] [Rur 05] [Hau 05b] [Roh 07]. However, as for the distinct adsorption heights, the bending cannot be the reason for a low value of the coherent fraction alone.

- As discussed in chapter 4 and chapter 5, the molecules adsorbed at step edges presumably have a strong influence on the resulting coherent fraction. The structural parameters of these molecules can be completely different to the parameters of the herringbone structure. Depending on the exact adsorption sites, this influence on the coherent fraction can be more of less strong. Within this work it was possible to observe this influence on the monolayer structure, by comparing the NIXSW results of different coverages below the full monolayer (as shown in chapter 4.4 with one scan for each coverage.)

However, it can be concluded that the PTCDA molecules in the precursor phase lie closer to the Ag surface than in the monolayer phase. This result is very surprising, since the metastable precursor phase was assumed to be less strongly bonded compared to the monolayer phase. The bonding distance, obtained in this work for the precursor phase, however, gives a strong evidence for an ever stronger chemisorptive bonding. This result leads to the question why the (chemisorbed) monolayer phase is a stable phase, although the molecules are further away from the Ag surface than in the precursor phase. This will be discussed at the end of this chapter.

6.3.2 Oxygen

For the monolayer phase as well as for the precursor phase, time dependent changes have been observed in the oxygen results. As for carbon, again, the results obtained on freshly prepared films are the most reliable ones.

Unfortunately, only XSW scans with a low resolution pass energy of the analyzer were taken on these (freshly prepared) films. Therefore, the results of these data only correspond to the total oxygen results. High resolution data have only been taken on the structural changed films. Therefore, a deviation in the structural parameters (compared to results of the freshly prepared films) is present in the results of the differential analysis.

Total oxygen

For the monolayer, the total oxygen results (coherent position and coherent fraction) are, within the errors, identical with the results obtained for carbon as can be seen in table 6.1 on page 137.

The situation is different for the precursor phase, where the value of the coherent position for oxygen lies 0.14 Å *below* the value for carbon. This corresponds to a difference in the vertical position of 0.19 Å compared to the monolayer oxygen. It is striking that the value of the coherent position for the oxygen atoms is so much lower for the precursor phase. The values of the coherent fraction, however, are similar for both phases ($C_F^{\text{ML-O}} = 0.52 \pm 0.06$ and $C_F^{\text{PC-O}} = 0.47 \pm 0.05$). Furthermore, the values of the coherent fractions have a size similar to that of the carbon atoms.

One reason for the relatively low coherent fractions of the total oxygen data may be the distinct heights of the chemically different oxygen atoms to the surface, which will be discussed in the following.

Differential analysis:

The differential analysis was performed on the high resolution data sets. Although, for both phases, small structural changes have been observed with time or with beam irradiation (see chapter 4.5.2 and chapter 5.3.3), the differential analysis bears interesting results which still can be assumed to be valid. This is because the noted structural changes do affect less than 15% of the molecules (ca. 10% bulk like contribution and ca. 4% additional oxygen contribution).

Another important point in the differential analysis is the quality of the fitting model used for the separation of the chemically different atoms. One has to note that a wrong fitting model can strongly influence the results. In particular, the values of the coherent fraction decrease by the use of a wrong model. Therefore, a correct fitting model is essential for the evaluation. However, a small value of the coherent fraction does not automatically imply vice versa that the fitting model is wrong.

The main result that was found for both phases is that the value of the coherent position for the anhydride oxygen lies above the value for the carboxylic oxygen[2].

Monolayer phase: It is quite surprising that the resulting value of the coherent fraction for the anhydride oxygen in the monolayer phase ($C_F^{\text{ML-O-anhyd.}} = 0.79 \pm 0.08$) corresponds to 82% of the value observed for the silver substrate. This indicates a highly ordered film and a good fitting model for the anhydride contribution in the PE spectrum. It reveals that all anhydride oxygen atoms in the monolayer are close to the vertical position of $C_{P\text{ eff}}^{\text{ML-O-anhyd.}} = (2.98 \pm 0.08)\,\text{Å}$. In contrast, the value of the coherent fraction for the carboxylic oxygen ($C_F^{\text{ML-O-carbox.}} = 0.47 \pm 0.22$) is much smaller. This is a hint that the carboxylic oxygen atoms occupy different vertical positions within the unit cell. The value of the coherent position for the carboxylic oxygen in the monolayer is $C_{P\text{ eff}}^{\text{ML-O-carbox.}} = (2.66 \pm 0.03)\,\text{Å}$ which lies clearly below the values for the anhydride oxygen and for the carbon[3].

---

[2] The NIXSW results for the monolayer in the herringbone structure represent 4 distinct adsorption sites for the carboxylic oxygen and 2 distinct adsorption sites for the anhydride oxygen (see chapter 4.5.5)[Kra 06].

[3] How much can the position of the four chemically different carboxylic oxygen atoms (in the monolayer) be split? By assuming two distinct positions and by assuming the values of the coherent fraction to be $C_{F,\text{ A, B}} = 0.8$ (as obtained for the anhydride oxygen), the resulting values for the coherent positions are $C_{P,\text{ B}} = 2.3\,\text{Å}$ and $C_{P,\text{ A}} = 3.0\,\text{Å}$. These parameters yield for the total coherent position of $C_P = 2.65\,\text{Å}$ and for the coherent fraction of $C_F = 0.48$. These resulting values correspond to the measured values for the carboxylic oxygens in the monolayer. This example shows that with the obtained value of the coherent

In the herringbone structure of the monolayer phase, two chemically different types of PTCDA molecules were observed (A and B) [Kra 06]. For each molecule type, two chemically different carboxylic oxygen atoms were found. Their difference is due to the distinct bonding to the neighboring PTCDA molecules. However, the H-O bonding lengths are identical by coincidence for both carboxylic oxygen types of one molecule, A or B respectively. It also has to be noted that the carboxylic oxygen atoms of type A occupy on-top positions on the silver atoms, whereas the carboxylic oxygen atoms of type B occupy more or less bridge positions. Considering these findings and the result of the present work, particularly the coherent fractions for the carboxylic oxygen atoms in the monolayer phase, it can be concluded that the carboxylic oxygen atoms have different vertical distances for the different types of the PTCDA molecules, A and B.

A model for the monolayer phase is given in figure 6.4. In this model two distinct vertical positions for the two molecules in the unit cell are assumed. Only the anhydride oxygen atoms occupy the same position in both molecules. With these distinct positions for the two molecules the values for the coherent fractions of the carbon and of the carboxylic oxygen can be explained. The corresponding values for this model are given in table 6.2

Precursor phase: In the precursor phase, within the errors, the value of the coherent position is the same for the anhydride oxygen and for the carbon ($C_{P\ \mathrm{eff}}^{\mathrm{PC\text{-}O\text{-}anhyd.}} = (2.83 \pm 0.04)$ Å and $C_{P\ \mathrm{eff}}^{\mathrm{PC\text{-}C}} = (2.80 \pm 0.02)$ Å). The value of the coherent position for the carboxylic oxygen clearly lies below the value for the carbon core ($\Delta C_P = 0.31$ Å). This splitting of the two oxygen positions ($\Delta C_P = 0.33$ Å) indicates a strong vertical distortion of the anhydride groups in the PTCDA molecule. However, the value of the coherent fractions C_F is rather small and lies between 0.40 and 0.48 for both types of oxygen atoms. Therefore, it can be assumed that the oxygen atoms, depending on their particular chemical environment (molecular structure) occupy different vertical heights which can differ quite strongly for the different structural en-

---

fraction, it cannot be excluded that the carboxylic oxygen atoms also occupy positions above the anhydride oxygen atoms.

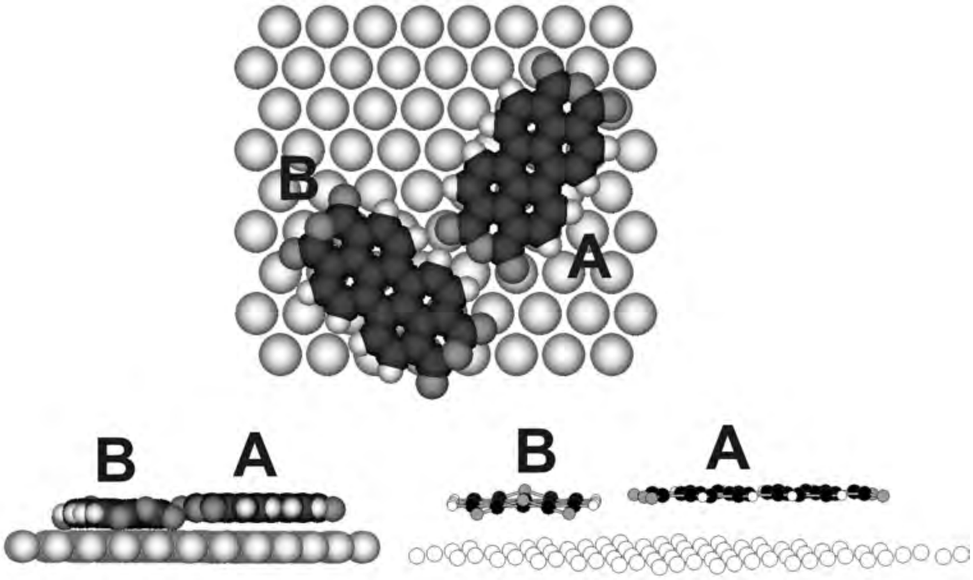

Figure 6.4: *Model, for the description of the observed values for the coherent position and coherent fraction. It was assumed that the two molecules (A and B) lie flat and occupy different vertical positions. See table 6.2 for the employed distances in this model. The x, y-coordinates are calculated from Rohlfing [Roh 05].*

vironments. That means that, in the precursor phase, some of the molecules lie even closer to the surface than it is indicated from the measured coherent position of $C_{P\,\text{eff}}^{\text{PC-C}} = 2.80\,\text{Å}$.

The strong distortion of the molecules in the precursor phase (particular the carboxylic oxygen atoms of the molecules) compared to the monolayer phase was not expected.

Additionally, it has to be noted that as the result for the carbon, the result for the oxygen also indicates different bonding mechanisms of the two phases.

Molecules at step edges of the substrate

As described for the monolayer and for the precursor, a model of PTCDA molecules populating the step edges of the substrate was developed within

	single molecules (with $C_F = 0.80$) A	B	resulting values for one unit cell	
	$C_{P\ \text{eff}}$	$C_{P\ \text{eff}}$	$C_{P\ \text{eff}}$	C_F
C	3.10 Å	2.60 Å	2.85 Å	0.63
carbox. O	3.00 Å	2.30 Å	2.65 Å	0.48
anhydr. O	2.98 Å	2.98 Å	2.98 Å	0.80

Table 6.2: *Structural parameters for the model which is one way to describe the measured values for the monolayer. The parameters correspond to the employed values in figure 6.4.*

this work (see chapter 4 and chapter 5). These, presumably upright standing molecules are assumed to be one reason for the observed structural differences which were found for different preparations and also during the experiment. A correction with a substrate like vector, contributing 10% to the result, was applied for both phases. In doing so, the oxygen values can be corrected to the values obtained on a freshly prepared film. The corrected values are given at the end of table 6.1.

For the precursor phase, a second additional oxygen position was found. Its contribution is around 4% to the total oxygen amount. It was only observed at binding energies close to those of the carboxylic oxygen in the PE spectra. However, it cannot be excluded that such a contribution exists at binding energies in the region of the anhydride oxygen peak, too. This could be a reason for the low value of the anhydride coherent fraction of the precursor phase ($C_F^{\text{PC-O-anhyd.}} = 0.48$). In chapter 5, a model of molecules at step edges of the silver substrate was given in order to explain this contribution.

6.3.3 Final geometric model

In figure 6.5 and 6.6, the results are shown for the monolayer and for the precursor phase. The values of the resulting coherent positions are presented by ball-and-stick models of the PTCDA molecules. The z-axis is expanded with a factor of 3 for a better visualization. The low resolution results for the carbon and the high resolution results for the oxygen are shown in part (a) of the figures. The corresponding Argand diagrams are presented below. The hard sphere model and the appropriate Argand diagrams for the (10% bulk like contribution) corrected values are given in part (b) of figure 6.5 and 6.6.

6.4 Bonding states of PTCDA on Ag(111)

The results of this work give the structural information for a better insight of the bonding mechanism of PTCDA molecules on Ag(111) for the two investigated phases.

Monolayer From electron spectroscopies [Jun 93] [Ere 03] [Zou 06] and the submolecular scanning tunneling contrast [Glö 98], some information on the bonding to the Ag(111) surface has already been gathered: the bonding is chemisorptive, it occurs presumably mainly on the perylene core of PTCDA, and it involves the formation of a partially filled hybrid orbital, originating from the LUMO of the free molecule and Ag 5s electrons. However, the anhydride groups must also be important, as the bonding distance of the carboxylic oxygen atoms is considerably lower to the surface than for the perylene core. DFT calculations revealed negative partial charges on the anhydride groups causing the formation of secondary bonds of the four carboxylic oxygen atoms to the Ag, thereby leading to the vertical distortion of the molecule [Hau 05a] [Rur 05] [Hau 05b].

From DFT, it also can be concluded that the noted two bonding mechanisms, although involving different parts of the molecule, go hand in hand in their mutual effect onto each other: Charge transfer into the LUMO is promoted by Ag-O interactions, supported by in-plane distortions in the perylene skeleton. These distortions lower the energy of the LUMO and hence promote its filling [Hau 05a].

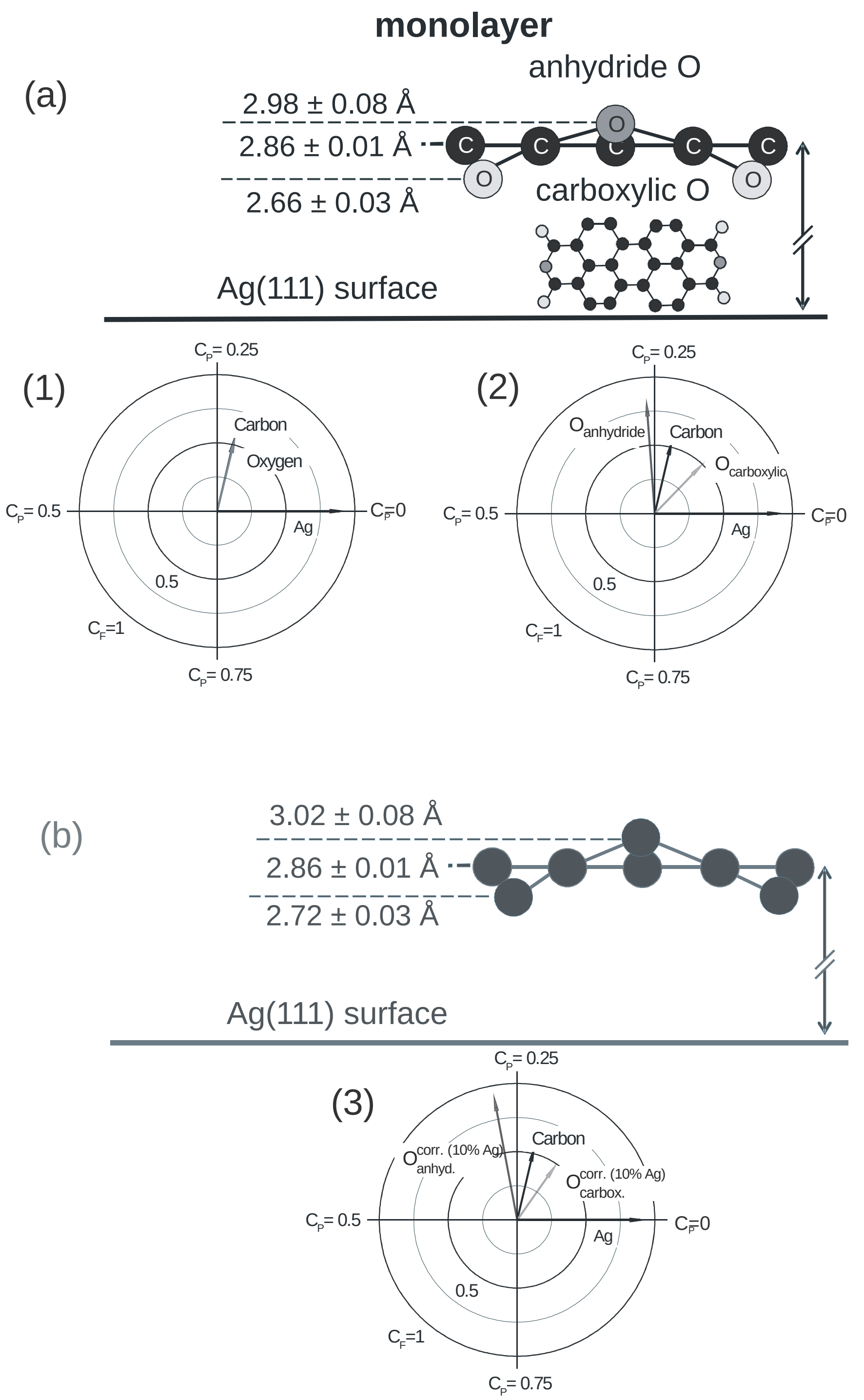

Figure 6.5: *Ball-and-stick model of molecules in the monolayer. The vertical length scale is expanded by a factor of three.* ***(a)*** *Model directly derived from experimental results.* ***(b)*** *Corrected model with 10% bulk like contribution.* ***(1) - (3)*** *Results presented in Argand diagrams.* ***(1)*** *on a freshly prepared film.* ***(2)*** *Same result for carbon as in (1), but for the oxygen, the structurally changed results are shown.* ***(3)*** *Results as in (2) but with the bulk like correction for the oxygen results.*

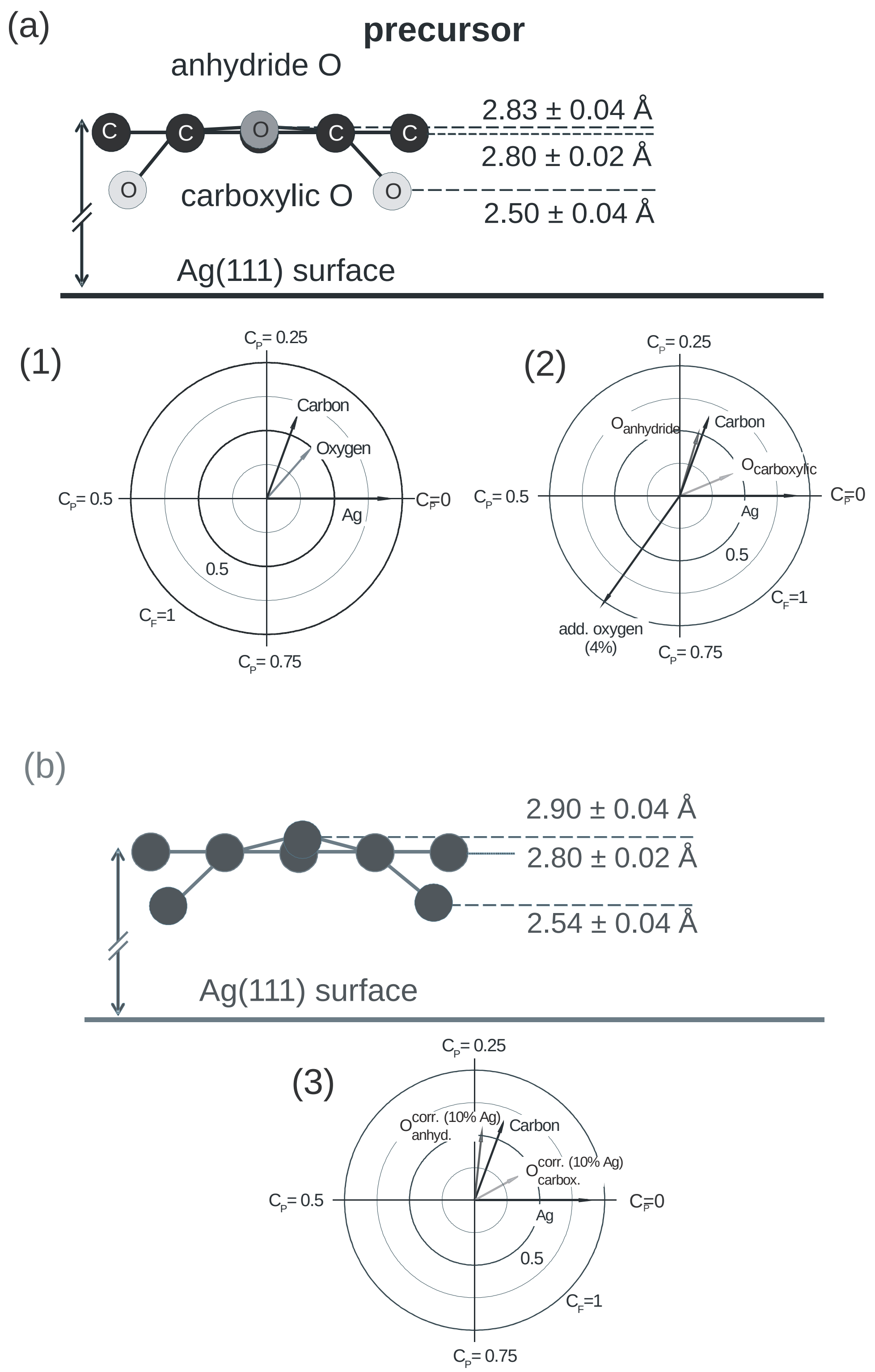

Figure 6.6: *Ball-and-stick model of molecules in the precursor. The vertical length scale is expanded by a factor of three.* ***(a)*** *Model directly derived from experimental results.* ***(b)*** *Corrected model with 10% bulk like contribution.* ***(1) - (3)*** *Results presented in Argand diagrams.* ***(1)*** *on a freshly prepared film.* ***(2)*** *Same result for carbon as in (1), but for the oxygen, the structurally changed results are shown.* ***(3)*** *Results as in (2) but with the bulk like correction for the oxygen results.*

Precursor Within this work, it was found that the average vertical bonding distance of the perylene core of the precursor phase is with $C_{P\,\mathrm{eff}}^{\text{PC-C}} = (2.80 \pm 0.02)$ Å smaller by 1.8% compared to the monolayer phase with $C_{P\,\mathrm{eff}}^{\text{ML-C}} = (2.86 \pm 0.01)$ Å, the difference being clearly above the error bar of the determination. This small bonding distance is a strong evidence that the molecules in the precursor phase are chemisorbed, too. For comparison, physisorbed PTCDA on Au(111) exhibits the much larger bonding distance of 3.27 Å [Hen 07].

Additional support for a chemisorptive bonding is given by the internal vertical distortion of the precursor phase compared to the monolayer phase: for the precursor phase the carboxylic oxygen atoms lie (in average) 0.31 Å below the perylene core, which is a significantly larger distortion than for the monolayer phase (0.20 Å). As discussed above for the monolayer phase, the lowering of the carboxylic oxygen atoms towards the Ag-surface can be interpreted by the formation of secondary bonds between the negatively polarized carboxylic oxygen atoms and the Ag surface. This indicates that in the precursor phase there are significant local bonds to the Ag on the anhydride groups, too.

In the commensurate ordered monolayer phase, however, it additionally has to be considered that the specific intermolecular interactions noted above compete with the O-Ag bonds. Possibly the intermolecular bonds withdraw some electron density from the carboxylic oxygen atoms, thereby weakening the O-Ag bonds and thus lower the distortion, as it is experimentally observed. A further consequence is an increase in the vertical bonding distance of the perylene cores with respect to the substrate.

In the above model, an activation barrier between the precursor and the monolayer phase is related to the relaxation of the internal distortion (loosening the O-Ag bonds) and the simultaneous increase of the overall bonding distance to the substrate. However, the total energy gain is positive, since an energy larger than the activation energy is gained by forming the specific attractive intermolecular bonds, including their possible back-action on the interfacial bonds which are formed in the commensurate, ordered phase.

Chapter 7

Summary

In this work, the bonding lengths of a large π-conjugated molecule which was adsorbed on a metal surface were determined for the first molecular layer.

For the growth of organic films on different substrates, the interactions between the first molecular layer and the underlying substrate play a major role for the properties and functionality of the whole system. This is because these interactions determine the electronic properties of the interface, the molecular order and the subsequent growth behavior of the film.

In this work, the system consisting of the organic molecules 3,4,9,10-Perylenetetracarboxylic dianhydride (PTCDA) grown on a silver (111) surface was investigated. PTCDA on Ag(111) appears in two phases in the first layer: The commensurate long range ordered monolayer at room temperature (RT phase) is a stable phase, whereas the disordered phase which is grown at temperatures below 160 K (LT phase) is a metastable phase. The LT phase changes at temperatures above 160 K to the stable RT phase.

For both phases, the planar molecules are adsorbed in a flat lying geometry. The molecules of the first layer are chemisorbed on the Ag(111) surface. However, for the LT phase it was believed that the bonding is weaker than for the RT phase. The bonding distance of the molecules from the surface is an indication for the bonding strength. Distortions of the molecules from the planar geometry give additional information on the bonding mechanism.

Therefore, in this work, the vertical bonding lengths for PTCDA adsorbed on silver(111) were determined with the NIXSW technique. The measurements on both systems, the RT and the LT phase were conducted at the ESRF in Grenoble / France.

Using NIXSW, the vertical distance of the molecules was investigated by the core-level C1s transition. Since carbon is the main element of the molecules, its vertical distance corresponds to the averaged molecular distance. Furthermore, the distances of the oxygen atoms of the molecules were determined by using the O1s transition.

In the PTCDA molecule, two types of chemically different oxygen atoms exist: the four outer carboxylic oxygen atoms and the two inner anhydride oxygen atoms. For the first time, this chemical shift of one atom sort within a molecule was utilized for a separation of the photoemission spectra which were taken in a standing wave experiment. Within this work, different vertical positions for atoms of the same element could be identified.

The vertical positions of the molecules in the RT and the LT phase were determined, as well as the intramolecular distortions. However, due to multipole effects, systematic errors occur in the resulting values. This is because the exact multipole parameters are not known, yet. These errors lead to small changes in the structural results, however, they affect the effect of the intramolecular distortion only little. Nonetheless, the comparison of the results for the two phases is reliable, since the systematic errors are in a similar range for both systems.

The main results of this work are summarized in figure 7.1. It shows the bonding distances of the atoms of the PTCDA molecule to the Ag(111) surface,

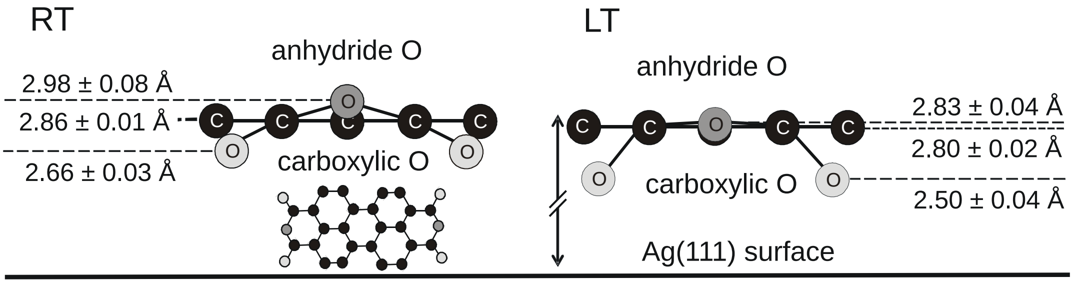

Figure 7.1: *Main results of the present work. The vertical length scale is expanded by a factor of three.*

obtained within this work. For the RT phase an average molecular bonding distance of 2.86 Å was measured (as defined from the average carbon distance). For the LT phase the corresponding value is 2.80 Å. Thus, the molecules in the LT phase are 0.06 Å closer to the Ag surface than the molecules in the RT phase, this result clearly is significant.

In the LT phase, a stronger intramolecular distortion was observed, the oxygen atoms lie 0.14 Å below the carbon core, whereas the molecules in the RT phase do not exhibit such a strong distortion, the result for the (total) oxygen atoms is the same as for the carbon atoms, within the errors.

By analyzing the separated oxygen types the surprising result was achieved that these chemically different oxygen atoms occupy different vertical positions on the surface. For both phases, it was found that the anhydride oxygen atoms are clearly above the carboxylic oxygen atoms. For the RT phase this internal distortion is 0.32 Å. For the LT phase, this difference corresponds to 0.33 Å.

The average vertical distance of the carboxylic oxygen atoms in the RT phase is 0.20 Å below the carbon core and 2.66 Å above the surface. For the LT phase, however, this molecular distortion is larger, the carboxylic oxygen atoms lie 0.31 Å below the carbon core and the average vertical distance to the surface is only 2.50 Å which is 6% smaller than for the RT phase.

The main conclusion of the results obtained within this work is the strong influence of the local environment on the bonding position of the PTCDA molecules. The results also support that the molecules are chemisorbed, both in the RT phase and in the LT phase, since the bonding distance is small for both phases.

As the main bonding of the molecules occurs via the central perylene ring in the RT phase, the internal distortions of the molecules indicate a secondary bonding mechanism between the negatively polarized carboxylic oxygen atoms and the Ag surface. Since the distortion of the molecules in the LT phase is even larger, this indicates that there are significant local bonds to the Ag on the anhydride groups in the LT phase, too. In the commensurate ordered RT phase, however, it has to be additionally considered that the specific intermolecular interactions compete with the O-Ag bonds. Possibly, the intermolecular bonds withdraw some electron density from the carboxylic oxygen atoms, thereby weakening the O-Ag bonds and thus lowering the distortion, as it is observed experimentally. A further consequence is the observed increase in the vertical bonding distance of the perylene cores with respect to the substrate.

The result of this work reveals that the bonding mechanisms of large π-conjugated molecules are even more complex than it was assumed in the past. For the principal understanding of the bonding mechanisms, these newly obtained results are very useful. With the geometrical results, obtained in this work, the parameter space for calculations from first principles can be considerably restricted, which will support the understanding of the involved bonding interactions of such a system.

Finally, this result can help for the general understanding of the bonding at interfaces as an important aspect for the design of future applications. With this understanding, it might even become possible that organic electronics will be completely designed by calculations.

Appendix A

Acronyms

AES Auger electron spectroscopy

DFT density functional theory

EC4T end-capped quaterthiophene

ESRF European Synchrotron Radiation Facility

FWHM full width of half maximum

HOMO highest occupied molecular orbital

HOPG highly oriented pyrolytic graphite

HREELS high resolution electron energy loss spectroscopy

LEED low energy electron diffraction

LUMO lowest unoccupied molecular orbital

NIXSW normal incidence x-ray standing waves

OFET organic field effect transistor

OLED organic light emitting diode

OSC organic semiconductors

PCA	principal component analysis
PE	photoemission
PSD	photon-stimulated desorption
PTCDA	3,4,9,10-perylenetetracarboxylic dianhydride
STM	scanning tunnelling microscopy
STS	scanning tunnelling spectroscopy
TFA	target factor analysis
UHV	ultra-high vacuum
UPS	ultraviolet photoelectron spectroscopy
UV-PEEM	UV photoelectron emission microscopy
XPS	x-ray photoelectron spectroscopy
XSW	x-ray standing waves

Appendix B

Multipole parameters in literature

- [BecPra 89]; C1s; $E = 2.000\,\mathrm{keV}$; $Q = 0.23$ - similar result from nonrelativistic calculation and exact relativistic numerical calculation.
- [Jac 00]; Jackson et al. measured the non dipolar parameters on incoherent films at low temperatures, but they had an error in their fitting routine. The values turned out to be too low.
  - O1s; $E = 2.975\,\mathrm{keV}$ [Cu(111) - $(\bar{1}11)$-reflection]; $\gamma = 1.04 \pm 0.04$;
  - C1s; $E = 3.046\,\mathrm{keV}$ [Ni(111) - $(\bar{1}11)$-reflection]; $\gamma = 0.92 \pm 0.08$;
- [Lee 01]; Lee et al. measured the non dipolar parameters on incoherent films at low temperatures. The maximal error given for the Q values is $s_{Q\,\max} = 0.025$.
  - O1s; $E = 2.661\,\mathrm{keV}$ [Al(111) - $(\bar{1}11)$-reflection]; $Q\,(\theta = 50°) = 0.29$
  - O1s; $E = 2.978\,\mathrm{keV}$ [Cu(111) - $(\bar{1}11)$-reflection]; $Q\,(\theta = 50°) = 0.30$ {0.32 / 0.35 values from [Jac 00] corrected, second value discussed as outrider}
  - O1s; $E = 3.072\,\mathrm{keV}$ [Al(111) - (200) - reflection]; $Q\,(\theta = 50°) = 0.32$
  - O1s; $E = 3.439\,\mathrm{keV}$ [Cu(111) - (200) - reflection]; $Q\,(\theta = 50°) = 0.31$

  - C1s; $E = 2.661\,\text{keV}$ [Al(111) - ($\bar{1}$11) - reflection]; $Q\,(\theta = 50°) = 0.34$
  - C1s; $E = 2.978\,\text{keV}$ [Cu(111) - ($\bar{1}$11) - reflection]; $Q\,(\theta = 50°) = 0.26$ / 0.30
  - C1s; $E = 3.072\,\text{keV}$ [Al(111)-(200)-reflection]; $Q\,(\theta = 50°) = 0.35$ / 0.40
  - C1s; $E = 3.439\,\text{keV}$ [Cu(111) - (200) - reflection]; $Q\,(\theta = 50°) = 0.18$ - The coherent fraction was relatively high, though it was measured on incoherent films. However, for the determination of Q, the coherent fraction has to be zero. Therefore the fit of the parameter Q to the data is rather not valid and the result for the Q-value is less reliable.

- [Trz 01]; Trzhaskovskaya et al. calculated the values for the non-dipole parameters. A relativistic treatment of the photo effect was used. The calculations were carried out in the one-electron approximation for a free atom.

  - O1s; $\gamma = 0.951$ ($E = 2\,\text{keV}$) and $\gamma = 1.20$ ($E = 3\,\text{keV}$) $\Rightarrow$ extrapolated for $E = 2.6\,\text{keV}$ is $\gamma \approx 1.10$
  - C1s; $\gamma = 0.979$ ($E = 2\,\text{keV}$) and $\gamma = 1.22$ ($E = 3\,\text{keV}$) $\Rightarrow$ extrapolated for $E = 2.6\,\text{keV}$ is $\gamma \approx 1.12$

- [Sch 01]; Schreiber et al. measured Q on incoherent films. However, by regarding the XSW scans in paper of Schreiber (figure 2), it can be seen that in the fit of the O1s and the C1s electron yield not identical curves were obtained. The O1s curve has a larger amplitude. This may originate from a coherent fraction which is *not* equal zero, as it was assumed.

  - O1s;$E = 2.6\,\text{keV}$ [Ag(111) - (111)-reflection] $Q\,(\theta = 45°) = 0.31 \pm 0.03$
  - C1s;$E = 2.6\,\text{keV}$ [Ag(111) - (111)-reflection] $Q\,(\theta = 45°) = 0.31 \pm 0.03$

- [Sta 04]; Stanzel et al. made a comparison of the O KLL Auger electron yield with O1s electron yield of NTCDA monolayers on Ag(111). He used for the O1s transition $Q\,(\theta = 45^\circ) = 0.26$. However, in the fitting routine, the non dipolar-parameter was not correctly implemented.

- [Sch 05b]; For the O1s transition, Schulte et al. used in their evaluation $Q\,(\theta = 45^\circ) = 0.31$. Only around that value, the right profiles could be obtained. Their work was done on functionalized fullerenes on Ag(111). However the statistics for the O1s profiles is very low.

- [Woo 05]; In this paper Woodruff et al. give the another correction for the O1s value from Jackson et al. [Jac 00], the one previously discussed as outrider (!) $Q\,(\theta = 50^\circ) = 0.37 \Rightarrow Q\,(\theta = 45^\circ) = 0.34$. In this paper also the corresponding value $\gamma = 1.42$ is given, however, this value corresponds to $Q\,(\theta = 45^\circ) = 0.33$.

- [Ger 05]; Gerlach et al. investigated multilayers of copper phtalocyanine-molecules on Cu(111) and Ag(111) substrates. They deduced the non-dipolar parameter for the C1s transition from those incoherent films.
  - C1s; $E = 2.980\,\mathrm{keV}$ [Cu(111) - (111)-reflection]; $S_R = 1.76 \pm 0.01$
  - C1s; $E = 2.630\,\mathrm{keV}$ [Ag(111) - (111)-reflection]; $S_R = 1.74 \pm 0.01$

- [Ger 07]; Gerlach et al. determined the vertical distance of PTCDA on Cu(111) and Ag(111). The Q value used for the PTCDA on the silver substrate is higher than the Q value used for PTCDA on the copper substrate (having a 350 eV higher photon energy). From theory is known, that with increasing photon energy the Q-values increase. This inconsistency in this paper is compensated with relatively high errors for S_R.
  - C1s; $E = 2.98\,\mathrm{keV}$ [Cu(111) - (111)-reflection]; $S_R = 1.85 \pm 0.1$
  - O1s; $E = 2.98\,\mathrm{keV}$ [Cu(111) - (111)-reflection]; $S_R = 1.72 \pm 0.1$
  - C1s; $E = 2.63\,\mathrm{keV}$ [Ag(111) - (111)-reflection]; $S_R = 1.89 \pm 0.05$
  - O1s; $E = 2.63\,\mathrm{keV}$ [Ag(111) - (111)-reflection]; $S_R = 1.89 \pm 0.05$

- [Sta 07]; Stadler et al. determined the vertical distance of NTCDA on Ag(111). For both transitions, O1s and C1s respectively they used a $Q\left(\theta = 45^\circ\right) = 0.27$.

Appendix C

Evaluation of Q in the present work

Within this work, the asymmetry parameter Q was determined on incoherent films. For incoherent films the value of the coherent fraction is equal to $C_F = 0$. Therefore the measured electron yield should follow this function:

$$\frac{dY}{d\Omega} \propto 1 + RS_R = 1 + R \cdot \frac{1+Q}{1-Q}. \tag{C.1}$$

In beamtime N'04, multilayers of water were adsorbed at low temperatures (100 K) on the top of half a monolayer of PTCDA on Ag(111). Using the obtained spectra, the anisotropy factor Q was fitted. However, for the profiles with the best conformity, the resulting values for Q vary from 0.10 to 0.37 even though the statistical error is negligible (less than 3%). Examples of these fits are displayed in figure C.1. Due to the wide range of values it becomes obvious that the adsorbed water on the PTCDA film was not a totally incoherent film, necessary for a precise evaluation of the parameter Q.

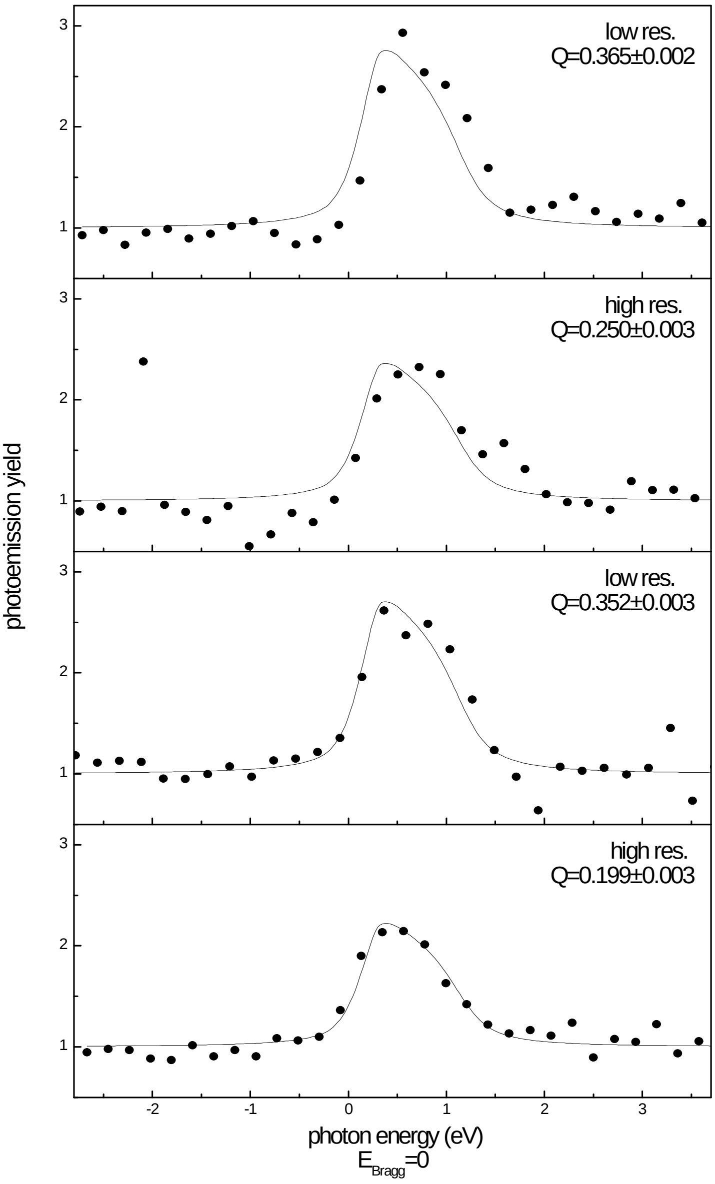

Figure C.1: *Variety of data sets, used for the evaluation of the asymmetry factor Q. The circles represent the experimental data and the lines the corresponding fits. The spectra were measured on the same spot with increasing time (from top to bottom). They were taken with distinct pass energies of the electron analyzer (high resolution:* 23 eV, *low resolution* 58 eV*). It is not clear, why the first two spectra are shifted. Presumably there is a coherent contribution which changes with time. Therefore, the fit of Q on this data is not reliable and can only be used as a rough estimation. The given errors correspond to the standard deviation of the fit.*

Appendix D

Parameter file for *DARE*

For the program *DARE,* the sample and the monochromator parameters are included in a file. The used parameters are listed below.

- Sample parameters

b value: -1
reflection plan: (111)
compound lattice constant: 4.08516 Å
d-spacing value: 2.35857 Å
$\chi_0 = -0.00470000 - i \cdot 0.000570000$
$\chi_1 = -0.00349000 - i \cdot 0.000560000$
$\chi_2 = -0.00349000 - i \cdot 0.000560000$
Debye-Waller factor: 0.980000

- Monochromator parameters

b value: -0.8
reflection plane: (111)
compound lattice constant : 5.43070 Å
d-spacing value: 3.13542 Å
$\chi_0 = -0.001393990 - i \cdot 0.000299275$
$\chi_1 = -0.000733302 - i \cdot 0.000209153$
$\chi_2 = -0.000733302 - i \cdot 0.000209153$
Debye-Waller factor: 0.988344

D.1 b-value

The b-value in the above parameter file corresponds for the monochromator crystal and for the sample crystal to

$$b = \frac{\vec{n} \cdot \vec{s}_0}{\vec{n} \cdot \vec{s}}.$$

The vector $\vec{n}$ is the unit vector of the surface normal of the diffracted crystal, and $\vec{s}_0$ and $\vec{s}$ are the unit vectors in the incident and diffracted beam directions. For the symmetric Bragg reflection $b = -1$. The Darwin-Prins curve (reflectivity) $R(b)$ is a function of b.

In order to include the mosaicity of the sample, instead of broadening the reflectivity curve with a convolution of a Gaussian function, the b value of the monochromator was changed from the value for the Bragg reflection ($b = -1$). In doing so, the width of the reflectivity curve could be varied as well as its height.

For a series of NIXSW experiments it was tested, which b-value of the monochromator yield the best fitting result on the reflectivity data. This value was fixed for the evaluation of all data of that series.

Appendix E

Background influence

In all PE-spectra of the standing wave experiment, a background had to be subtracted in order to obtain the NIXSW profiles. This had to be done very carefully, because an incorrect subtracted background can influence the result. Therefore, a model has to be developed in order to subtract the unwanted background contributions.

With such a model, it occurs that also a contribution of the peak under investigation is subtracted, too. That does not matter, because the shape (and hence the result) of a NIXSW profile does not change, if a contribution which follows the same intensity profile as the rest of the spectrum is missing. On the other hand side, an incorrect subtracted background can change the result, when the PE spectrum consists of different contributions with distinct NIXSW profiles.

Furthermore, if the background originating from the substrate is not correctly subtracted, a contribution of the substrate will remain in the data. That means that the structural information of the substrate mixes up with information of the peaks under investigation. Hence, in the results can be changed slightly due to the background contribution.

E.1 Background types

Two different background were used in order to subtract the substrate contributions, a linear background and a Shirley background type. The latter is exemplarily shown in figure E.1.

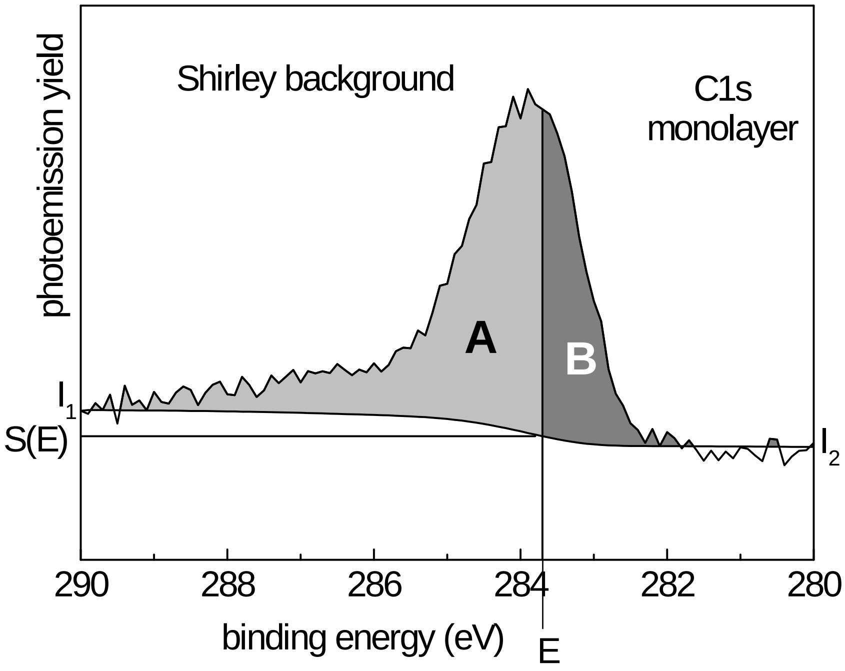

Figure E.1: *C1s spectrum of the monolayer. A Shirley type background was subtracted.*

Almost any fitting program provides a Shirley type background in the fitting routine, which is iteratively computed. In a first step an approximation of the Shirley background $S(E)$ is assumed which, in a second step, is iteratively refined. The formula used is the following:

$$S(E) = I_2 + (I_1 - I_2)\frac{B(E)}{(A(E) + B(E))}.$$

I_1 and I_2 correspond to the intensities of the PE spectrum at the two sides of the investigated spectrum. The integrated areas $A(E)$ and $B(E)$ (shown in figure E.1) are calculated in the first step with an approximation for the Shirley background.

E.2 Statistical background contributions

The photoemission signal consists of the substrate count rate N_{Ag} and the adsorbate count rate N_0. In the fit of the NIXSW profile the term

$$\left(N_0 \pm \sqrt{N_{Ag}} \pm \sqrt{N_0} - N_{fit}\right)^2$$

has to be minimized. However, $\sqrt{N_0} \ll N_0$ and can be neglected due to its small size. Therefore $\left(N_0 \pm \sqrt{N_{Ag}} - N_{fit}\right)^2$ has to be minimized. With a low count rate, the substrate contribution $\sqrt{N_{Ag}}$ in a standing wave scan can come up in the range of 10% of N_0. However, this is only the case for spectra with very low statistics. In the data of the present work a relation on the statistics and the substrate contribution in the results could not be observed.

Appendix F

Anhydride satellite in the O1s monolayer spectrum

In the present work, a satellite peak of the anhydride oxygen was found in the O1s spectra of the monolayer at a binding energy position of 535.8 eV. The analysis from which it could be concluded that this peak in fact belongs to the anhydride oxygen is presented in the following.

Different fitting models were investigated on the off-Bragg spectra. Those with the smallest values for χ^2 were subsequently tested on the PE spectra of a standing wave experiment. It was found that in the PE spectra of the standing wave, the observed peak clearly has the same variation in the electron yield as the anhydride peak. It was also tried to treat this feature as a shake up of the carboxylic oxygen, but in that case, the residuals became larger. So, after the minimization of the χ^2, it can be excluded, that this peak belongs to the caboxylic oxygen.

This result is in contrast to that of Unwin et al. [Unw 03], who attributes this peak to background scattering. However, Unwin et al. analyzed PTCDA multilayers on InSb(111)A, so that a direct comparison of the spectra is not possible.

In figure F.1 the result of the χ^2 analysis is shown. Using the spectral envelope $\{s_j\}$ and a synthetic model $\{m_j\}$ the χ^2 is defined in the following way

$$\chi^2 = \sum \frac{(s_j - m_j)^2}{|s_j|}.$$

The different fitting models shown in figure F.1 correspond to the best fitting models, found by the minimization of χ^2 in the fit of the off-Bragg PE spectra.

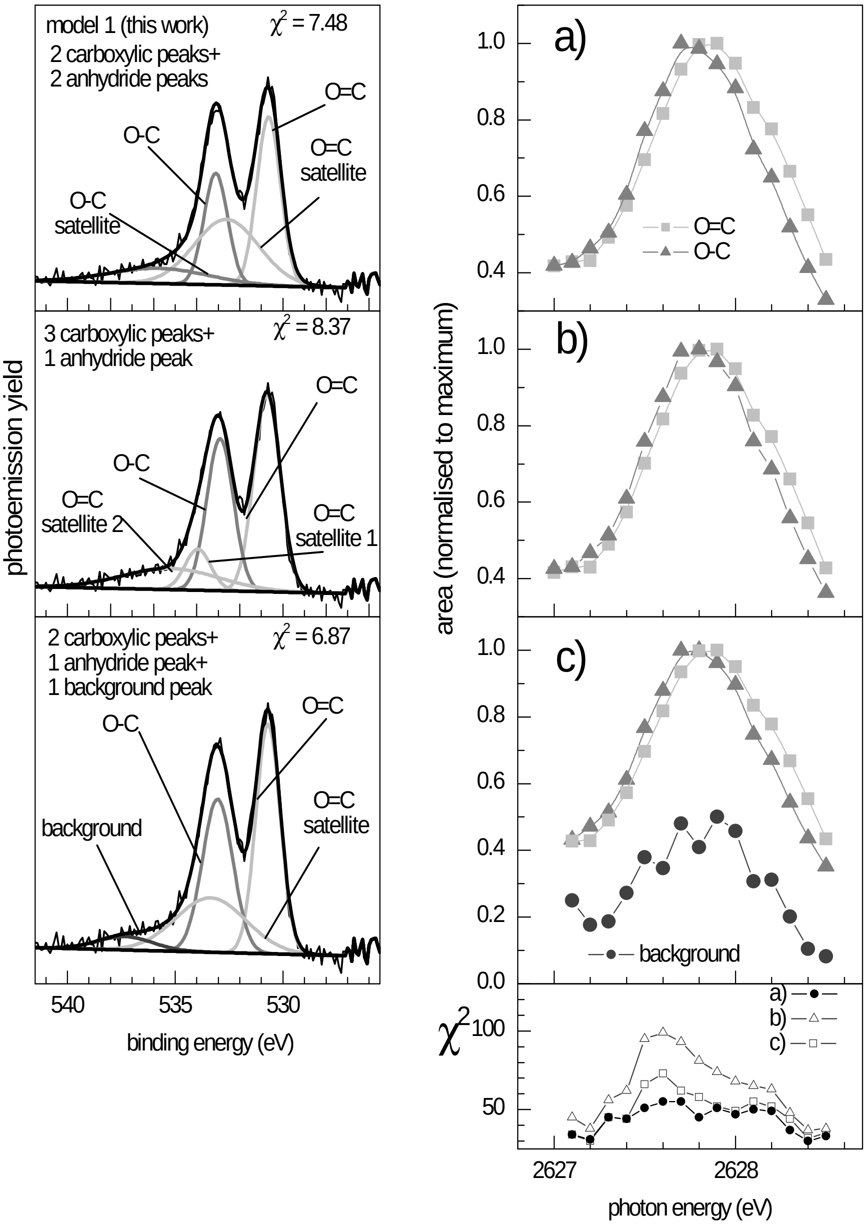

Figure F.1: *Left: Fitting models for the different peak compositions and the corresponding* χ^2 *values of the fit in an off-Bragg spectrum. Right a), b) and c): NIXSW profiles derived from the appropriate fits on the PE spectra, taken with an excitation energy close to the Bragg condition. Bottom on the right:* χ^2 *analysis for the fits on the PE spectra used for the NIXSW profiles. Each point corresponds to the* χ^2 *of the appropriate fit. It can be seen that the model used in this work leads to the lowest* χ^2 *values.*

Appendix G

Principal-Component Analysis

The shape of a photoemission (PE) spectrum is the result of its composition from different peaks with distinct origins convoluted with the instrumental function, e. g., the O1s spectrum of the PTCDA on silver is a composition of many peaks. Two contributions come from the two chemically different type of oxygen atoms of the PTCDA molecule with slightly shifted binding energies. In addition to this, there exist numerous shake up features from these two O1s components. Due to the distinct vertical positions of the two type of oxygen atoms the shape in PE spectra changes within photon energy in a standing wave experiment. This is due to the fact that each component undergoes its own intensity curve which results from the specific vertical position and distribution. This gives rise to the question, whether it is possible to extract the exact peak features of the distinct peaks from a set of XSW spectra. A method for this would be the principal component analysis (PCA). In the computer program *CasaXPS* [Fai 01] the PCA function for XPS spectra is included. For the decision of the applicability of this method a closer look onto the PCA method and onto the composition of standing wave spectra is useful.

G.1 PCA introduction

The data matrix in XPS is composed of spectra where each acquisition channel is viewed as a coordinate in an r-dimensional space: r is equal to the number of acquisition channels per spectrum. The problem addressed by PCA is that of determining the number of distinct spectroscopic features present in a particular set of c spectra. [Fai 01].

With the Principal Component Analysis (or Eigenanalysis) the spectra of a set can be described with a linear combination of a number of principal components (artificial spectra). If there exists a linear dependency, the principal components (Eigenvectors) span the subspace, which has a lower dimensionality than the number of the spectra of the set. Whereas the original data are interrelated, the resulting principal components are uncorrelated.

PCA provides a method for identifying the underlying spectra that form the building blocks for the entire set of spectra. The data matrix is transformed into a new set of r-dimensional vectors. These new vectors span the same subspace as the original columns of the data matrix, however they are now characterized by a set of eigenvalues and eigenvectors. The eigenvalues provide a measure for the significance of the principal components with respect to the original data.

G.2 XSW spectra composition

How do the components of the PE spectra change in a standing wave experiment? Do they follow mathematical functions, which can be separated by PCA? For clarification, a closer look at the PE yield in a standing wave experiment helps. The photoelectron intensity profile from an atom within the interference field (characterized by $\vec{h}$) is described by [Zeg 93]

$$I \propto 1 + R\left(\nu\right) + 2\sqrt{R\left(\nu\right)}(\cos(\nu - 2\pi\vec{h}\cdot\vec{r}). \tag{G.1}$$

Herein $R(\nu)$ is the reflectivity, $\vec{r}$ the vector of the atom-position and ν the phase,which changes from 0 to π in a standing wave experiment.

For a number N of atoms of a particular element the yield is the sum of the scattered yields from the individual atoms at position $\vec{r_i}$.

$$I \propto 1 + R(\nu) + \frac{2}{N}\sqrt{R(\nu)}\sum_{i=1}^{N}\cos(\nu - 2\pi\vec{h}\cdot\vec{r_i}) \tag{G.2}$$

Herein, the scalar product $\vec{h}\cdot\vec{r_i}$ is equal to the coherent position C_P (for more details see chapter 3.1).

As an example, an adsorbate will be considered with two different vertical adsorption sites on the surface. The binding energies of the two types is assumed to be chemically different. This yields two peak components in the PE spectrum, which follow both the intensity curve of equation G.2. However their phases of the cosines are different , depending on their particular vertical position. Therefore, the PE yield follows

$$I_{1,\,2} = 1 + R(\nu) + 2\sqrt{R(\nu)}\cos(\nu - 2\pi C_{P\,1,\,2}). \tag{G.3}$$

Thus, for two adsorption sites, two principal components are necessary for the description of the spectra. However, the two components, obtained by PCA, are NOT equivalent to the two components of equation G.3. They correspond to the mathematical necessary components for a linear combination to describe the change in the set of PE spectra. These components also may become negative.

In this work artificial spectra were tested with PCA. Spectra with one, two, three and more components on different binding energy positions were tested. Each spectrum changed in intensity with a cosine. All cosines had distinct phases.

The testing revealed that maximal three principal components are necessary for the description of the spectra[1]. That means, measuring the intensity yield of the substrate leads to only one component (of course). Two distinct adsorbate positions yield two principal components and three and more positions always yield three principal components. However, in this discussion contributions with a phase shift of π to the observed coherent position was not

---

[1] Within this work, it could not be clarified why only three components and not more are necessary for the description of the NIXSW data.

considered. Such a component will not be identified as a new component with PCA.

Also, when the energy position is identical for two distinct contributions, it is often not possible to observe this additional component with PCA.

If the analysis yields more than three principal components, there is a systematic error in the experimental system, e.g. irregular steps of the monochromator or desorption of the adsorbate during the experiment.

G.3 PCA on XSW Photoemission spectra and TFA

PCA is a nice tool for kicking out the noise of the spectra. After applying a PCA, the determined principal components can be used for the so-called target factor analysis (TFA). This is the fit of the principal components to the real spectra. If there are spikes they can be identified and omitted in the analysis. The structure of the PE spectra becomes visible and the spectra are much smoother.

If there is photon stimulated desorption or if the monochromator works irregular, this can be seen, by comparing the analysis of a set of XSW experiments on the same system. In short, PCA makes the changing peak features visible for the eye. The target tested spectra yield to a fitting model, which can be used on the measured spectra.

It was tested in this work that applying the fitting model to the target tested spectra and to the purely measured spectra give the same results.

Bibliography

[AloGar 04] M. I. Alonso and M. Garriga, Thin Solid Films **455-456** (2004) 124.

[AshMer 76] N. W. Ashcroft and N. D. Mermin, *solid state physics*, Harcourt Brace College Publishers (1976).

[Bar 00] J. V. Barth, Surface Science Reports **40** (2000) 75.

[BarRav 03] S. M. Barlow and R. Raval, Surface Science Reports **50** (2003) 201.

[BatCol 64] B. W. Batterman and H. Cole, Reviews of Modern Physics **36** (1964) 681.

[Bau 07] O. Bauer, *private communication* (2007).

[BecPra 89] A. Bechler and R. Pratt, Physical Review A **39** (1989) 1774.

[Bul 96] V. Bulović, P. E. Burrows, S. R. Forrest, J. A. Cronin, and M. E. Thompson, Chemical Physics **210** (1996) 1.

[Car 90] A. F. Carley, P. R. Davies, M. W. Roberts, and K. K. Thomas, Surface Science Letters **238** (1990) L467.

[Chi 77] C. K. Chiang, C. R. Fincher, Jr, Y. W. Park, A. J. Heeger, H. Shirakawa, E. J. Louis, S. C. Gau, and A. G. MacDiarmid, Physical Review Letters **39** (1977) 1098.

[Coo 93] J. W. Cooper, Physical Review A **47** (1993) 1841.

[EckKan 71] P. Eckerlin and H. Kandler, *Landolt-Börnstein*, vol. 6, Springer-Verlag Berlin, Numerical Data and Functional Relationships in Science and Technology ed. (1971).

[EhrHud 66] G. Ehrlich and F. G. Hudda, Journal of Chemical Physics **44** (1966) 1039.

[Ere 03] M. Eremtchenko, J. A. Schaefer, and F. S. Tautz, Nature **425** (2003) 602.

[Ere 04] M. Eremtchenko, D. Bauer, J. A. Schaefer, and F. S. Tautz, New Journal of Physics **6** (2004) 4.

[Fai 01] N. Fairley, *CasaXPS User's Manual*, 2.0 ed. (2001).

[Fis 98] C. J. Fisher, R. Ithin, R. G. Jones, G. J. Jackson, D. P. Woodruff, and B. C. C. Cowie, Journal of Physics: Condensed Matter **10** (1998) L623.

[For 84] S. R. Forrest, M. L. Kaplan, and P. H. Schmidt, Journal of Applied Physics **55** (1984) 1492.

[For 97] S. R. Forrest, Chemical Reviews **97** (1997) 1793.

[FreBig 87] H.-J. Freund and R. W. Bigelow, Physica Scripta **T 17** (1987) 50.

[Ger 05] A. Gerlach, F. Schreiber, S. Sellner, H. Dosch, I. A. Vartanyants, B. C. C. Cowie, T.-L. Lee, and J. Zegenhagen, Physical Review B **71** (2005) 205425.

[Ger 07] A. Gerlach, S. Sellner, F. Schreiber, N. Koch, and J. Zegenhagen, Physical Review B **75** (2007) 045401.

[Glö 98] K. Glöckler, C. Seidel, A. Soukopp, M. Sokolowski, E. Umbach, M. Böhringer, R. Berndt, and W.-D. Schneider, Surface Science **405** (1998) 1.

[Gre 98] W. Greulich, ed., *Lexikon der Physik*, Spektum, Akad. Verl. Heidelberg (1998).

[Grö 94] O. Gröbner, A. G. Mathewson, and P. C. Marin, Journal of Vacuum Science and Technology A **12** (1994) 846.

[Han 91] W. Hansen, M. Bertolo, and K. Jacobi, Surface Science **253** (1991) 1.

[Hau 05a] A. Hauschild, K. Karki, B. C. C. Cowie, M. Rohlfing, F. S. Tautz, and M. Sokolowski, Physical Review Letters. **94** (2005) 036106.

[Hau 05b] ——, Physical Review Letters. **95** (2005) 209602.

[Hen 07] S. K. M. Henze, O. Bauer, T.-L. Lee, M. Sokolowski, and F. S. Tautz, Surface Science **601** (2007) 1566.

[HenGöp 94] M. Henzler and W. Göpel, *Oberflächenphysik des Festkörpers*, Teubner Verlag (1994).

[Hos 94] A. Hoshino, S. Isoda, H. Kurata, and T. Kobayashi, Journal of Applied Physics **76** (1994) 4113.

[Hsi 01] G. H. Hsiung, K. Y. Young, Y. J. Hsu, and J. R. Chen, Journal of Vacuum Science and Technology A **19** (2001) 1657.

[Jab 03] A. Jablonski, F. Salvat, and C. J. Powell, *NIST Electron Elastic-Scattering Cross-Section Database, Version 3.0*, National Institute of Standards and Technology (2003).

[Jac 00] G. J. Jackson, B. C. C. Cowie, D. P. Woodruff, R. G. Jones, M. S. Kariapper, C. Fisher, A. S. Y. Chan, and M. Butterfield, Physical Review Letters **84** (2000) 2346.

[Jun 93] M. Jung, U. Baston, G. Schnitzler, M. Kaiser, J. Papst, T. Porwol, H. J. Freund, and E. Umbach, Journal of Molecular Structure **293** (1993) 239.

[Kil 02a] L. Kilian, PhD thesis, Universität Würzburg (2002).

[Kil 02b] L. Kilian, W. Weigand, E. Umbach, A. Langner, M. Sokolowski, H. L. Meyerheim, H. Maltor, B. C. C. Cowie, T. Lee, and P. Bäuerle, Physical Review B **66** (2002) 0754121.

[Kil 04] L. Kilian, E. Umbach, and M. Sokolowski, Surface Science **573** (2004) 359.

[Kil 07] L. Kilian, A. Hauschild, R. Temirov, A. Schöll, A. Bendounan, F. Reinert, T.-L. Lee, F. S. Tautz, M. Sokolowski, and E. Umbach, *submitted to Physical Review Letters* (2007).

[Kla 06] H. Klauk, ed., *Organic Electronics*, Wiley-VCH (2006).

[Kra 06] A. Kraft, R. Temirov, S. K. M. Henze, S. Soubatch, M. Rohlfing, and F. S. Tautz, Physical Review B **74** (2006) 0414021(R).

[Lee 01] J. J. Lee, C. J. Fisher, D. P. Woodruff, M. G. Roper, R. G. Jones, and B. C. C. Cowie, Surface Science **494** (2001) 166.

[Lov 84] A. J. Lovinger, S. R. Forrest, M. L. Kaplan, P. H. Schmidt, and T. Venkatesan, Journal of Applied Physics **55** (1984) 476.

[Lud 94] C. Ludwig, B. Gompf, J. Petersen, R. Strohmaier, and W. Eisenmenger, Zeitschrift für Physik B **93** (1994) 365.

[Mar 94] P. C. Marin, Nuclear Instruments and Methods in Physics Research B **89** (1994) 69.

[Mar 06] H. Marchetto, U. Groh, T. Schmidt, R. Fink, H.-J. Freund, and E. Umbach, Chemical Physics **325** (2006) 178.

[MoeKar 92] M. Moebus and N. Karl, Journal of Crystal Growth **116** (1992) 495.

[Nel 02] E. J. Nelson, J. C. Woicik, P. Pianetta, I. A. Vartanyants, and J. W. Cooper, Physical Review B **65** (2002) 165219.

[Roh 05] M. Rohlfing, *private communication* (2005).

[Roh 07] M. Rohlfing, R. Temirov, and F. S. Tautz, *unpublished* (2007).

[Rur 05] R. Rurali, N. Lorente, and P. Ordejòn, Physical Review Letters **95** (2005) 2096011.

[Sch 01] F. Schreiber, K. A. Ritley, I. A. Vartanyants, H. Dosch, J. Zegenhagen, and B. C. C. Cowie, Surface Science **486** (2001) L519.

[Sch 03] A. Schöll, PhD thesis, Universität Würzburg (2003).

[Sch 04] A. Schöll, Y. Zou, M. Jung, T. Schmidt, R. Fink, and E. Umbach, Journal of Chemical Physics **121** (2004) 10260.

[Sch 05a] A. Schöll, *private communication* (2005).

[Sch 05b] K. Schulte, R. A. J. Wooley, L. Wang, P. J. Moriarty, P. R. Birkett, H. W. Kroto, and B. C. C. Cowie, Nuclear Instruments and Methods in Physics Research A **547** (2005) 208.

[Sch 06] S. Schmitt, PhD thesis, Universität Würzburg (2006).

[SchShi 66] R. Schwoebel and E. Shipsey, Journal of Applied Physics **37** (1966) 3682.

[Sei 93] C. Seidel, PhD thesis, Physikalisches Institut der Universität Stuttgart (1993).

[SH 97] T. Schmitz-Hübsch, T. Fritz, F. Sellam, R. Staub, and K. Leo, Physical Review B **55** (1997) 7972.

[SH 99] T. Schmitz-Hübsch, T. Fritz, R. Staub, A. Back, N. R. Armstrong, and K. Leo, Surface Science **437** (1999) 163.

[ShaCow 98] A. G. Shard and B. C. C. Cowie, Journal of Physics: Condensed Matter **10** (1998) L69.

[Shi 00] H. Shirakawa, R. MacDiarmid, and A. Heeger, *nobelprice in chemistry* (2000).

[Shk 00] V. Shklover, F. S. Tautz, R. Scholz, S. Sloboshanin, M. Sokolowski, J. A. Schaefer, and E. Umbach, Surface Science **454-456** (2000) 60.

[Soa 99] E. A. Soares, V. B. Nascimento, V. E. de Carvalho, C. M. C. de Castilho, A. V. de Carvalho, R. Toomes, and D. P. Woodruff, Surface Science **419** (1999) 89.

[Sta 04] J. Stanzel, W. Weigand, L. Kilian, H. L. Meyerheim, C. Kumpf, and E. Umbach, Surface Science **571** (2004) L311.

[Sta 06] C. Stadler, S. Hansen, F. Pollinger, C. Kumpf, E. Umbach, T.-L. Lee, and J. Zegenhagen, Physical Review B **74** (2006) 035404.

[Sta 07] C. Stadler, S. Hansen, A. Schöll, T.-L. Lee, J. Zegenhagen, C. Kumpf, and E. Umbach, New Journal of Physics **9** (2007) 50.

[Tab 95] J. Taborski, P. Väterlein, H. Dietz, U. Zimmermann, and E. Umbach, Journal of Electron Spectroscopy and Related Phenomena **75** (1995) 129.

[Tau 02a] F. S. Tautz, M. Eremtchenko, J. A. Schaefer, M. Sokolowski, V. Shklover, and E. Umbach, Physical Review B **65** (2002) 125405.

[Tau 02b] F. S. Tautz, M. Eremtchenko, J. A. Schäfer, M. Sokolowski, V. Shklover, K. Glöckler, and E. Umbach, Surface Science **502-503** (2002) 176.

[Tem 06a] R. Temirov, *private communication* (2006).

[Tem 06b] R. Temirov, S. Soubatch, A. Lucian, and F. S. Tautz, Nature **444** (2006) 350.

[Trz 01] M. B. Trzhaskovskaya, V. I. Nefedov, and V. G. Yarzhemsky, Atomic Data and Nuclear Data Tables **77** (2001) 97.

[Trz 06] M. B. Trzhaskovskaya, V. K. Nikulin, V. I. Nefedov, and V. G. Yarzhemsky, Atomic Data and Nuclear Data Tables **92** (2006) 245.

[Umb 96] E. Umbach, M. Sokolowski, and R. Fink, Applied Physics A **63** (1996) 565.

[Umb 98] E. Umbach, K. Glöckler, and M. Sokolowski, Surface Science **402-404** (1998) 20.

[Unw 03] P. J. Unwin, D. Onoufriou, and T. S. Jones, Surface Science **547** (2003) 45.

[Var 05] I. Vartanyants, T.-L. Lee, S. Thiess, and J. Zegenhagen, Nuclear Instruments and Methods in Physics Research A **547** (2005) 196.

[VarZeg 97] I. A. Vartanyants and J. Zegenhagen, Nuovo Cimento **19** (1997) 617.

[VarZeg 00] ——, Solid State Communications **113** (2000) 299.

[Wag 07] T. Wagner, A. Bannani, C. Bobisch, and H. K. R. Möller, Journal of Physics: Condensed Matter **19** (2007) 056009.

[WitWöl 04] G. Witte and C. Wöll, Journal of Materials Research **19** (2004) 1889.

[Woo 98] D. P. Woodruff, Progress in Surface Science **57** (1998) 1.

[Woo 05] ——, Nuclear Instruments and Methods in Physics Research A **547** (2005) 187.

[WooDel 94] D. P. Woodruff and T. A. Delchar, *Modern Techniques of Surface Science*, Cambridge Solid State Science Series, 2nd ed. (1994).

[Zeg 93] J. Zegenhagen, Surface Science Reports **18** (1993) 199.

[Zeg 02] ——, *DARE* (2002).

[Zou 06] Y. Zou, L. Kilian, A. Schöll, T. Schmidt, R. Fink, and E. Umbach, Surface Science **600** (2006) 1240.

Erklärung

An Eides statt versichere ich, dass ich diese Dissertation „*The Adsorption Geometry of PTCDA on Ag(111) – an NIXSW Study*“ selbst und ohne jede unerlaubte Hilfe angefertigt habe, dass diese oder eine ähnliche Arbeit noch keiner anderen Stelle als Dissertation eingereicht worden ist und dass sie an den nachstehenden Stellen auszugsweise veröffentlicht worden ist.

- Hauschild, A., Karki, K., Cowie, B. C. C., Rohlfing, M., Tautz, F. S. und Sokolowski, M.: „*Molecular distortions and chemical bonding of a large π-conjugated molecule on a metal surface*“, Physical Review Letters, **94**, 0361061 (2005).

- Hauschild, A., Karki, K., Cowie, B. C. C., Rohlfing, M., Tautz, F. S. und Sokolowski, M.: „*Reply: Molecular distortions and chemical bonding of a large π-conjugated molecule on a metal surface*“, Physical Review Letters, **95**, 2096021 (2005).

- Kilian, L., Hauschild, A. , Temirov, R., Schöll, A., Tautz, F. S., Sokolowski, M., Reinert, F., Lee, T.-L., Umbach, E.: „*A structural and electronic phase transition at a metal-organic interface: The role of intermolecular interactions*“
  Eingereicht

Bonn, 31. August 2007

Annegret Hauschild

Liste eigener Publikationen

- Hauschild, A., Karki K., Temirov, R., Schöll A., Lee, T.-L., Cowie, B. C. C., Tautz, F. S. und Sokolowski, M.: „*Normal incidence x-ray standing wave determination of the adsorption geometry of PTCDA on Ag(111): comparison of the ordered and disordered phase*“

  In Vorbereitung

- Kilian, L., Hauschild , A., Schöll, A., Tautz, F. S., Sokolowski, M., Reinert, F., Umbach, E.: „*A structural and electronic phase transition at a metal-organic interface: The role of intermolecular interactions*“

  Eingereicht

- Hauschild, A., Karki, K., Cowie, B. C. C., Rohlfing, M., Tautz, F. S. und Sokolowski, M.: „*Molecular distortions and chemical bonding of a large π-conjugated molecule on a metal surface*“, Physical Review Letters, **94**, 0361061 (2005).

- Hauschild, A., Karki, K., Cowie, B. C. C., Rohlfing, M., Tautz, F. S. und Sokolowski, M.: „*Reply: Molecular distortions and chemical bonding of a large π-conjugated molecule on a metal surface*“, Physical Review Letters, **95**, 2096021 (2005).

- Langner, A., Hauschild, A., Fahrenholz, S. und Sokolowski,M.: „*Structural properties of tetracene films on Ag(111) investigated by SPA-LEED and TPD*“, Surface Science, **574,** 153 (2005).